Université de Lille

Unité Mécanique Lille UML J. Boussinesq

Numerical Simulation of the Mechanical Behavior of a New Composite Material in the Marine Environment

Simulation numérique du comportement mécanique d'un nouveau matériau composite en milieu marin

Thèse de doctorat de l'Université de Lille
préparée à Unité de Mécanique de Lille - Joseph Boussinesq (UML)

École Graduée N°632 Sciences de l'Ingénierie et des Systèmes (ENGSYS)
Spécialité: Mécanique des solides, des matériaux, des structures et des surfaces (MSMSS)

Sous la direction de :
Prof. Jean-Marie Nianga et Prof. Toufik Kanit

Co-encadrant :
Prof. Zefeng Wang et Prof. Yunliang Jiang (Huzhou University)

Thèse présentée et soutenue à Villeneuve d'Ascq, le 5 février 2026, par

YIFEI PENG

Composition du Jury :

Abdelwaheb Amrouche Professeur, Université d'Artois	Président (Examinateur)
Fouad Erchiqui Professeur, Université du Québec en Abitibi-Témiscamingue	Rapporteur
Sheng Wu Professeur, Harbin Engineering University	Rapporteur
Raquel-Jahara Lobosco Professeure, Université fédérale de Rio de Janeiro	Examinatrice
Toufik Kanit Professeur, Université de Lille	Co-directeur de thèse
Jean-Marie Nianga Professeur, JUNIA	Directeur de thèse

Thèse de doctorat

Remerciements

“礼有三本: 天地者, 生之本也; 先祖者, 类之本也; 君师者, 治之本也.” - 荀子, ≪ 礼论 ≫

Le respect envers les enseignant(e)s et les professeurs est une valeur culturelle traditionnelle que les Chinois défendent depuis l'Antiquité. Et dans la société d'aujourd'hui, les enseignant(e)s et les professeurs représentent les connaissances et les opportunités.

En conséquence, je voudrais tenir à exprimer ma gratitude envers tous les professeurs qui m'ont aidé tout au long de mes études doctorales. Je remercie des professeurs qui ont pris la direction de ma thèse, M. Jean-Marie NIANGA, M. Toufik KANIT et M. Zefeng WANG. Je remercie les professeur(e)s en tant que membres du jury de la thèse, M. Fouad ERCHIQUI, M. Sheng WU, M. Abdelwaheb AMROUCHE et Mme Raquel-Jahara LOBOSCO. Je remercie les professeurs qui ont beaucoup aidé pendant mes études, M. M'hamed SOULI, M. Fahmi ZAIRI, M. Abdellatif IMAD, M. Enrico CALZAVARINI, Mme Silvia DA COSTA HIRATA, M. Laurent PEYRODIE, M. Yunliang JIANG. Je voudrais remercier spécialement le directeur de l'ED ENGSYS, M. Henri HAPPY.

Je remercie également mes collègues qui sont très gentils. Lionel, Silvia, Hamdi, Anissa, Ahmed, Saad, je suis heureux de travailler avec vous. Je remercie Mathieu qui m'a aidé à débloquer dans la recherche. Je remercie également Lionel.

Je voudrais vivement exprimer ma sincère gratitude et mon amour à mes parents. J'ai appris de mes parents la persévérance et le sens de travailler avec

diligence et pragmatisme. C'est vous qui m'avez toujours soutenu, me permettant d'accomplir ce que d'autres n'auraient pas pu atteindre. Il est impossible d'exprimer mes remerciements infinis à vous par des mots. MERCI et JE VOUS AIME.

Je remercie aussi ma sœur, tu soutiens notre famille et prends bien soin de nos parents.

Je remercie Xin, un facteur dans mon destin, une cause qui m'a amené sur ce chemin. Que les étoiles guident notre chemin, une piste de l'harmonie et du bonheur.

Enfin, ces dernières années passées à l'UML ont été vraiment inoubliables. Ce fut une expérience riche d'exploration, de communication, de recherche, de collaboration et de croissance. C'est un terminus et un autre point de départ.

Abstract

With the development of intelligent equipment, unmanned surface vehicles nowadays are widely used in the fields of defense, environmental surveillance and offshore energy, and possess promising application prospects. Benefiting from the ability to make use of renewable energy at sea, surface vehicles such as the Wave glider and AutoNaut are capable of performing long-duration missions in marine environments. The hull structure of a small to medium-sized surface vessel is generally made of sandwich-structured composite materials with the skin generally being the glass fiber or carbon fiber-reinforced polymers. Investigating the interaction between the hull structure of a surface vehicle and water waves, as well as evaluating the level of wave impact loads under its operating sea state conditions, are the major focus of this study. This can support research on the mechanical response and fatigue behavior of composite structures under dynamic loading induced by water waves. The wave-structure interaction problem is carried out through numerical experiments in this study. Numerical simulations are performed using the Arbitrary Lagrangian Eulerian method. This approach combines the advantages of the Lagrangian and Eulerian formulations, allowing for multi-material computation and the presence of large material deformations in the simulation. Based on this approach, a numerical wave flume model with damping zones for water wave absorption is constructed, which is first applied to simulate the water waves corresponding to the working sea conditions of the wave glider, and then, the wave impact scenarios are carried out with a structure simulating the wave glider's float cou-

pled into the numerical wave flume. The numerical generation of water waves is on the basis of linear wave theory and piston-type wavemaker theory. Four sets of target waves have been set up based on the dimension parameters of the numerical wave flume and the wave glider's general operating sea states. Profiles of generated water waves are measured and compared to the analytical solution of target waves derived from the linear wave theory. Error rates of simulated water waves are calculated in order to verify the effectiveness of the numerical wave flume and the accuracy of the wave generation. Then, the wave-structure interaction simulations use the same four sets of target waves. A coupling algorithm based on the penalty method is used to model the contact between fluids and the structure, also to predict the wave loads at the wave-structure interface. Wave load data is collected and analyzed. The posture changes of the structure under influence of wave impacts are also investigated. Computational resources devoted to water wave generation and wave-structure interaction simulations are studied to verify different weightings of Arbitrary Lagrangian Eulerian calculation in their computations. As a result, this study has investigated the water wave generation and wave-structure interaction problems through numerical simulations. The numerical wave flume model constructed in this study is valid and has the potential to be extended for more complex application scenarios.

Contents

Remerciements i

Abstract iii

List of Figures x

List of Tables xi

Acronyms xii

Symbols xiv

Introduction 1

1 Research Context 5

1.1 Wave Glider 5

1.1.1 Structure 6

1.1.2 Applications for Ocean Observation 10

1.1.3 Load Analysis 11

1.2 Marine Composites 18

1.2.1 Application of Marine Composites as Structural Materials 20

1.2.2 Reinforcement Fibers 23

1.2.3 Structure and Matrix 30

1.3 Wave Load Calculation Method 33

1.3.1 Numerical Wave Flume 34
1.3.2 Fluid-Structure Interaction Simulation 36
1.4 Conclusion 38

2 Wave Theories and Wave Generation 41
2.1 Linear Wave Theory 41
2.2 Wave Generation 51
2.2.1 Piston-Type Wavemaker Theory 55
2.2.2 Wave Flume and Wave Characteristics 61
2.3 Wave Absorption and Non-reflective Boundary 63
2.4 Conclusion 69

3 Numerical Method for Fluid-Structure Interaction Simulation 71
3.1 Arbitrary Lagrangian Eulerian Method 71
3.1.1 ALE Description and Referential Domain 72
3.1.2 ALE Navier–Stokes Governing Equations 78
3.1.3 Weak Formulation 81
3.1.4 Split Method 83
3.1.5 Lagrangian Phase Computation 87
3.1.6 Advection algorithm 91
3.2 Interface Tracking Method 97
3.2.1 Multi-material formulation 97
3.2.2 Interface Tracing and Reconstruction 99
3.3 Coupling Algorithm Based on Penalty Method 100
3.3.1 Contact Conditions 102
3.3.2 Coupling Forces Based on the Penalty Method 103
3.4 Conclusion 106

4 Numerical Experiments of Water Waves and Wave–Structure Interaction 108
4.1 Wave Generation in a Numerical Wave Flume 108

4.1.1 Wave Flume Configuration 109
4.1.2 Material Models 110
4.1.3 Analytical Target Waves 112
4.1.4 Simulation Results 114
4.1.5 Results Analysis 117
4.2 Simulation of Wave–Structure Interaction 120
4.2.1 Coupling Structure in the Wave Flume 120
4.2.2 Simulation Results 121
4.2.3 Water Wave Impact Loads 123
4.2.4 Structure Posture Analysis 129
4.3 Conclusion 131

A Analytical Wave Profiles of Target waves **134**

B Simulated Target Waves **137**

C Simulated Wave-Structure Interaction **140**

D Impact Pressure Data **143**

List of Figures

1.1 Wave Glider (a) and AutoNaut (b) 6
1.2 Model of a 3-Meter Scale Wave Glider 7
1.3 Simplified Water Particle Trajectories 8
1.4 Schema of Propulsion through Wave Motion 9
1.5 Marine Environmental Loads 15
1.6 Structure of Laminate Composite (a) and Sandwich Composite (b) 31

2.1 Linear Wave Schema 43
2.2 Governing Equation and Boundary Conditions of Linear Wave . . 50
2.3 Piston-Type Wavemaker 52
2.4 Flap-Type Wavemaker 53
2.5 Governing Equation and Boundary Conditions of Piston-Type Wave Generation 58
2.6 Schema of Standing Wave Phenomena 63
2.7 Diagram of the Rayleigh Mass and Stiffness Damping 69

3.1 Material Domain, Spatial Domain, Referential Domain and the Transformation of Coordinates 74
3.2 8-Node Solid Element 87
3.3 Interface Reconstruction 101
3.4 Penalty Coupling Schema 104

4.1 Wave flume with damping zones 110

4.2 Analytical Wave Profiles of Target Waves E1, E2 113
4.3 Computation Hardware Description 114
4.4 Wave Generation Without Damping Zone 115
4.5 Simulated Target Wave E1 With Damping Zones 116
4.6 Comparison of Normal and Damping Nodal Velocities 116
4.7 Simulated Target Waves E1, E2 118
4.8 Wave Flume Coupled With Structure 121
4.9 Wave Impacts From Target waves E1, E2 122
4.10 Nodes on the Fluid-Structure Interface 124
4.11 X-Direction Pressure Data From Impact E1 125
4.12 Y-Direction Pressure Data From Impact E1 125
4.13 Impact Phase Analysis of Node-31347 126
4.14 Impact Phase Analysis of Node-31452 127
4.15 X-Direction Pressure Data From Impact E2 128
4.16 Y-Direction Pressure Data From Impact E2 128
4.17 Structure Motion Subjected to Impact E2 130

A.1 Analytical Wave Profiles of Target Waves E1, E2 134
A.2 Analytical Wave Profiles of Target Waves E3, E4 135
A.3 Analytical Wave Profiles of Target Waves E5, E6 135
A.4 Analytical Wave Profiles of Target Waves E7, E8 136

B.1 Simulated Target Waves E1, E2 137
B.2 Simulated Target Waves E3, E4 138
B.3 Simulated Target Waves E5, E6 139
B.4 Simulated Target Waves E7, E8 139

C.1 Wave Impacts From Target waves E1, E2 140
C.2 Wave Impacts From Target waves E3, E4 141
C.3 Wave Impacts From Target waves E5, E6 142
C.4 Wave Impacts From Target waves E7, E8 142

D.1 X-Direction Pressure Data From Impact E1 143
D.2 Y-Direction Pressure Data From Impact E1 144
D.3 X-Direction Pressure Data From Impact E2 144
D.4 Y-Direction Pressure Data From Impact E2 145
D.5 X-Direction Pressure Data From Impact E3 145
D.6 Y-Direction Pressure Data From Impact E3 146
D.7 X-Direction Pressure Data From Impact E4 146
D.8 Y-Direction Pressure Data From Impact E4 147
D.9 X-Direction Pressure Data From Impact E5 147
D.10 Y-Direction Pressure Data From Impact E5 148
D.11 X-Direction Pressure Data From Impact E6 148
D.12 Y-Direction Pressure Data From Impact E6 149
D.13 X-Direction Pressure Data From Impact E7 149
D.14 Y-Direction Pressure Data From Impact E7 150
D.15 X-Direction Pressure Data From Impact E8 150
D.16 Y-Direction Pressure Data From Impact E8 151

List of Tables

1.1 Beaufort Wind Scale 12
1.2 Sea State 14
1.3 Mechanical Properties of Glass Fibers 25
1.4 Mechanical Properties of Aramid Fibers 27
1.5 Mechanical Properties of PAN-based Carbon Fibers 30
1.6 Mechanical Properties of Pitch-based Carbon Fibers 30

2.1 Classification of Water Waves by Relative Water Depth 62

4.1 Target Wave Parameters and Analytical Solutions 112
4.2 Relative Depth, Wave Steepness and Relative Wave Height of Target Waves 113
4.3 Simulated Wave Parameters and Errors 118
4.4 Statistics on Computation Resources (Wave Generation) 119
4.5 Statistics on Computation Resources (FSI) 123
4.6 Max Normal Pressure Data on Fluid-Structure Interface 129

Acronyms

$AFRP$ Aramid Fiber-Reinforced Polymer
ALE Arbitrary Lagrangian Eulerian
CEL Coupled Euler-Lagrange
CFD Computational Fluid Dynamics
CFL Courant-Friedrichs-Lewy
$CFRP$ Carbon Fiber-Reinforced Polymer
EOS Equation of State
$Eq.$ Equation
FEM Finite Element Method
FRP Fiber-Reinforced Polymer / Fiber-Reinforced Plastic
FSI Fluid-Structure Interaction
FVM Finite Volume Method
$GFRP$ Glass Fiber-Reinforced Polymer / Glass Fiber-Reinforced Plastic
GRP Glass-Reinforced Plastic
$MUSCL$ Monotone Upwind Schemes for Conservation Laws
NS Navier-Stokes
PAN Polyacrylonitrile
PG Petrov-Galerkin
$PLIC$ Piecewise Linear Interface Construction
$SALE$ Structured Arbitrary Lagrangian Eulerian
$SLIC$ Simple Line Interface Calculation
$SSHWS$ Saffir-Simpson Hurricane Wind Scale

$SUPG$ Streamline Upwind Petrov-Galerkin

TC Tropical Cyclone

USV Unmanned Surface Vehicle / Uncrewed Surface Vessel

VOF Volume of Fluid

Symbols

In Chapter 2

d water depth

H wave height

a wave amplitude

L wavelength

T wave period

f wave frequency

c phase velocity of wave

k wave number

H/L wave steepness

d/L relative water depth

ρ density of the fluid

$\boldsymbol{u}(u, w)$ fluid velocity

∇ Nabla operator

$\boldsymbol{\omega}$ vorticity field

$\boldsymbol{\phi}(x, z, t)$ velocity potential

$\boldsymbol{\Gamma}$ object

$\Gamma(x, y, z, t)$ surface expression of the object

$B(x, z, t)$ surface expression of the bottom

η free surface

$F(x, z, t)$ surface expression of the free surface

p pressure

$\boldsymbol{f}$ body force

$\boldsymbol{\Omega}$ potential function of the body force

p_a atmospheric pressure

g gravitational acceleration

e mathematical constant of exponential function

$S(z)$ / S / S_0 stroke of the paddle

θ frequency of paddle's motion

$P(x, z, t)$ surface expression of the paddle

$e(z)$ general expression of the wavemaker's displacement

ϕ_H homogeneous solution of velocity potential

ϕ_P particular solution of velocity potential

$[C]$ damping matrix

$[M]$ mass matrix

$[K]$ stiffness matrix

α mass weighted damping coefficient

β stiffness weighted damping coefficient

$\{X\}$ matrices of displacement or deformation

$\{F_T\}$ matrix of total force

$[\boldsymbol{I}]$ identity matrix

In Chapter 3

Ω_0 material domain

Ω_t spatial domain

$\hat{\Omega}$ referential domain

Γ_0 material domain boundary

Γ_t spatial domain boundary

$\hat{\Gamma}$ referential domain boundary

$\vec{X}$ coordinates of the material domain

$\vec{x}$ coordinates of the spatial domain

$\vec{\xi}$ coordinates of the referential domain

$\vec{\Phi}$ injective function relating coordinates of the spatial domain to coordinates of the material domain

$\hat{\vec{\Phi}}$ injective function relating coordinates of the referential domain to coordinates of the spatial domain

$\vec{t_0}$ / $\vec{t}$ / $\hat{\vec{t}}$ traction set at the boundaries $\Gamma_0^{\vec{t}}$ $\Gamma_t^{\vec{t}}$ / $\hat{\Gamma}^{\vec{t}}$

$\vec{v_0}$ / $\vec{v}$ / $\hat{\vec{v}}$ velocity set at the boundaries $\Gamma_0^{\vec{v}}$ / $\Gamma_t^{\vec{v}}$ / $\hat{\Gamma}^{\vec{v}}$

$\vec{u}$ displacement vector of a material mass

$\dot{\vec{u}}$ velocity vector of a material point

$\dot{\vec{v}}$ acceleration vector

$\hat{\vec{u}}$ grid displacement

$\hat{\vec{v}}$ grid velocity vector

$\vec{w}$ convective velocity

ρ density of the fluid

$\vec{v}$ velocity of a fluid particle

p pressure

$\boldsymbol{\Omega}$ viscous stress tensor

$\vec{g}$ gravity

E total energy per unit mass

$\boldsymbol{\Sigma}$ stress tensor

$\boldsymbol{I}$ identity matrix

$\vec{b}$ force per unit mass from the body force

e internal energy

$\boldsymbol{D}$ strain rate tensor

λ / μ Lamé coefficients

ν kinematic viscosity coefficient

η bulk viscosity coefficient

$\delta\rho$ / δv_i / δe test functions

L characteristic parameter of the length of the elements

$\mathcal{P}_e$ Péclet number

$S(\vec{x}, t)$ source term

$J_{\hat{\Phi}}$ Jacobian of the injective function

Ω_t^e 8-node solid element

N_I shape function

$Vol(\Omega_t^e)$ volume of an element

E_e total internal energy of the element

ρ_{ref} reference density

C Courant number

V_f^k volume fraction of a material in an element

$\dot{\bar{\varepsilon}}$ average strain rate of an element

$\dot{\varepsilon}^k$ strain rate of the material k

p^{eq} equilibrium pressure

ΔV_f^k variation of volume fraction

$\vec{n}$ normal of the interface segments

Ω^F fluid domain

Γ^F boundary of the fluid domain

$\vec{n}^F$ normal of the fluid domain

Ω^S structure domain

Γ^S boundary of the structure domain

$\vec{n}^S$ normal of the structure domain

Γ^C interface between structure domain and structure domain

d_n distance of penetration between fluid and structure

$\dot{d}_n$ penetration rate

$\vec{t}^{\,F}$ traction vector of the Cauchy stress of the fluid

$\vec{t}^{\,S}$ traction vector of the Cauchy stress of the structure

k spring stiffness

F_f force imposed on the master node

F_s force imposed on the slave node

M_S mass of the structure node (slave)

M_F mass of the fluid node (master)

Introduction

Wave load is an important factor affecting the safety of marine structures. The aim of this study is to investigate the water wave generation and wave-structure interaction problems, where the prediction of wave loads caused by wave impacts is one of the major focuses. The object to be investigated is a small-sized floating structure on the sea surface, the hull structure of a wave glider's float. This type of hull structure is generally made of sandwich-structured composite materials. Compared to typical metal materials, composite hull can provide better specific strength and excellent aging resistance in seawater. With wave loading data obtained under general working sea states of the wave glider, the mechanical response and fatigue behavior of the composite hull can be further investigated. This may help to improve the reliability and durability of the composite hull structure in marine environments and enhance the life cycle of the wave glider. In this study, generation of water waves as well as wave impacts are carried out through numerical simulations. The entire study consists of three parts, including research background investigation, theoretical studies, and numerical experiments. The studied subjects (wave glider, composite material), considered problems (water wave impact, marine environment), related theories (water wave theory, wavemaker theory, wave absorption method, numerical methods for the wave-structure interaction simulation), and the research results (numerical simulation results, analysis) are demonstrated in detail.

Chapter 1 concerns a survey of the research context. The targeted research object is the wave glider. As an unmanned and hybrid surface vehicle,

the structure, dimensional parameters, and general operating sea state conditions of the wave glider are presented. Application of the wave glider for tropical cyclone observation in extreme sea states is investigated. Then, environmental loading factors that the wave glider is subjected to in marine environments are analyzed. This brings forth the research subject, which is the investigation of water wave impacts on a surface vehicle. Following this point, an introduction to marine composites is presented, including the use of composites as structural materials in shipbuilding, the main reinforcement fibers, matrix materials as well as the structure of composites applied in marine environments. Then, a preliminary investigation of methods for performing wave load calculations is carried out. Based on the existing studies in literature, a commonly used and effective approach, the numerical wave flume, is proposed to carry out the simulation of water wave generation as well as wave-structure interaction. And the theoretical basis relating to the numerical methods is briefly described.

Chapter 2 describes the theoretical foundations used for water wave generation. Since the primary consideration of wave conditions are the general working sea states of the wave glider, linear wave theory is selected as the basis of water wave generation problem in this study. Firstly, the mathematical description of the water wave problem is established, which mainly includes the governing equation and the boundary conditions. Then, the simplified mathematical description is derived by introducing the assumption of the linear wave theory. Next, the piston-type wavemaker theory is presented. Associated boundary conditions are established assuming that water waves are generated due to the disturbances created by a paddle executing linear reciprocating movement. And the transfer function describing the relationship between wavemaker's movement and wave height is derived from the mathematical description of piston-type wavemaker theory for linear water wave generation. Some key parameters used to characterize water waves are also presented. In addition, wave reflections in the wave generation problem can badly affect the wave profile of the simulated target waves. Both passive and active water wave absorption meth-

ods are presented. And the use of artificial Rayleigh damping is proposed to suppress the effects of reflected waves in simulations.

Chapter 3 describes the numerical methods used in order to perform the wave-structure interaction simulations. Arbitrary Lagrangian Eulerian formulation is a commonly used approach to solve fluid-structure interaction problems. In addition to the material domain (Lagrangian formulation) and the spatial domain (Eulerian formulation), an arbitrary referential domain is introduced. The transition of material coordinates between three domains can be done through the injective functions. Then, internal nodes of the grid are allowed to move based on the convective velocity, thus enabling the ability to correct mesh distortions. The governing equations used to describe the fluid are Navier-Stokes equations, and their expressions under the Arbitrary Lagrangian Eulerian description are given. To simplify the resolution of Navier-Stokes equations, split method is introduced. This method divides the computation into a Lagrangian phase and an Eulerian phase. Then, the final computational outputs need to be projected onto a new grid through an advection algorithm. This grid is determined by the convective velocity, and in the presence of large deformations, the new grid is generated to eliminate mesh distortions. An advection algorithm with second-order accuracy is presented. Next, the Young's method for the realization of interface tracking and reconstruction is described. The existence of interface between materials can be determined based on the material volume fraction information within each element. And the reconstruction of interface is performed using the piecewise linear interface calculation method. Finally, the Euler–Lagrange penalty coupling approach used to model the contact between fluids and the structure is briefly described. The coupling forces at the fluid-structure interface are predicted by a spring-like system where the important parameter (stiffness coefficient) that affects the prediction accuracy is discussed.

Chapter 4 presents and analyzes the simulation results. Numerical experiments are divided into two parts, water wave generation and wave-structure

interaction. The construction of a numerical wave flume is first described. The adopted material models are presented. Four sets of target water waves corresponding to the general operating sea states of the wave glider are simulated. The analytical solutions of target waves derived from linear wave theory are also presented. Then, the simulation scenes of water wave generation are shown. The necessity of wave absorption is illustrated, and the effect of used Rayleigh damping method is verified by comparing water particle velocities in different areas of the wave flume. Next, measured parameters of the simulated water waves are listed, as well as the error rates comparing their analytical solutions. The computational resources utilized for the water wave generation simulation are also presented. Similarly, for wave impact simulations, the numerical wave flume model with coupled structure is first presented. The impact simulation uses the same four sets of target waves. The type and setup of the fluid-structure contact are discussed. Then, the simulation scenes of water waves impacting the structure are shown. The computational resource usage between wave generation and wave impact is also compared. Wave loads at the wave-structure interface caused by impacts of target waves are collected and demonstrated. And the impact process is analyzed. At last, the dynamic motion of the structure under influence of wave impacts is illustrated.

Chapter 1

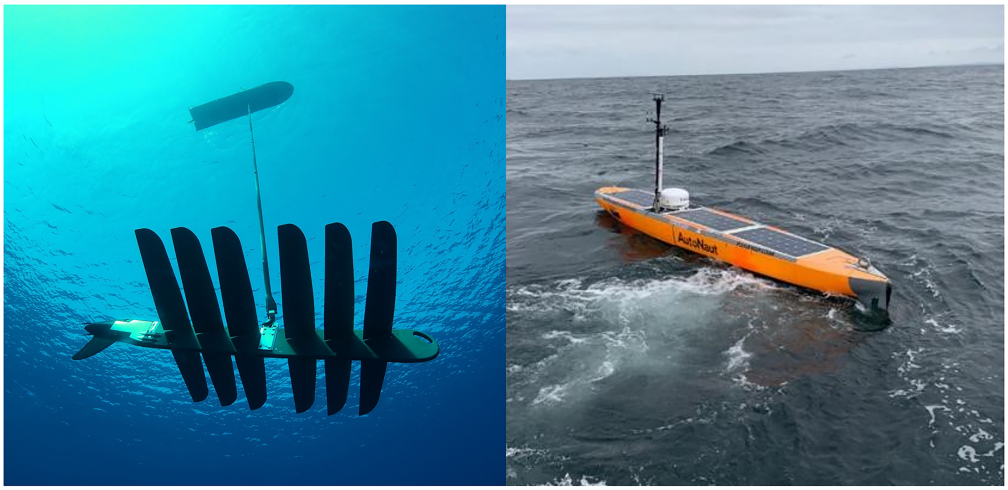
Research Context

1.1 Wave Glider

Wave glider is an unmanned surface vehicle (USV), a cost-effective autonomous ocean platform capable of carrying out long-duration missions. To fulfill this goal, it is designed to be able to make use of both solar and wave motion energy as a source of power for its electronic and propulsion systems. One advantage of this hybrid platform is that it allows the flexibility to configure different payload equipment so as to meet the requirements of different mission objectives. Wave glider is considered to have a wide range of applications in defense, environmental surveillance and offshore energy, making it a key research project in various countries and regions. The classic wave glider product is made by the American manufacturer Liquid Robotics [1]. China is also emphasizing the use of such technology, there are already mature products of wave gliders, including the “Black Pearl” produced by Tsingtao Hydrotech [2], the “Sea Sentinel” developed by Sun’s team [3] at Ocean University of China, and others. Another similar product that utilizes wave motion energy is the “AutoNaut” [4] un-

[1] www.liquid-robotics.com
[2] www.tsingtaohydrotech.com
[3] Xiujun SUN, Key Laboratory of Physical Oceanography, Ocean University of China
[4] www.autonautusv.com

crewed surface vessel (USV) made by a manufacturer in the United Kingdom. The Figure 1.1 shows the Wave Glider and AutoNaut.



(a) (b)

Figure 1.1: Wave Glider (a) and AutoNaut (b) [a]

a. Image source: www.liquid-robotics.com, www.autonautusv.com

1.1.1 Structure

The overall structure of a wave glider consists of three main parts, the float, the umbilical and the sub. It is a small-sized platform, and the length of the float ranges from 1.5 m (meter) to 3.5 m among different types of wave gliders. Due to the peculiarity of this surface-submerged hybrid structure, the normal operation of the wave glider requires a minimum working water depth. This characteristic also determines that its working range includes the water surface and shallow waters extending to about 30 m below the water surface (without taking into account its towing capacity for deep-water equipment).

In order to demonstrate the structure of the wave glider, a 3-meter scale 3D model is roughly modeled, as shown in Figure 1.2. The modeled wave glider has a float of 3 m in length and a sub of 2.2 m in length, which are connected by an umbilical with a length of 8 m.

Float of the wave glider is an unpowered, passive part. Its functions include: 1. providing buoyancy for the overall structure and installed payload instruments; 2. providing electrical power to the electronic system and the thruster installed at tail of the sub through solar panels on the float's top surface ; 3. providing cabin space for the installation of electronic payloads.

Sub is the propulsion part of the wave glider. It is fitted with a hydrofoil system capable of converting wave motion into forward thrust. The model in Figure 1.2 has 6 pairs of hydrofoils. Meanwhile, when the wave undulations are small, wave motion energy is not enough to support its movement, or when a higher cruising speed is needed, the thruster at tail of the sub can be activated. The tail fin mounted on the sub is also an important part for controlling wave glider's movement. It can be deflected through servo control in order to control the wave glider's overall direction.

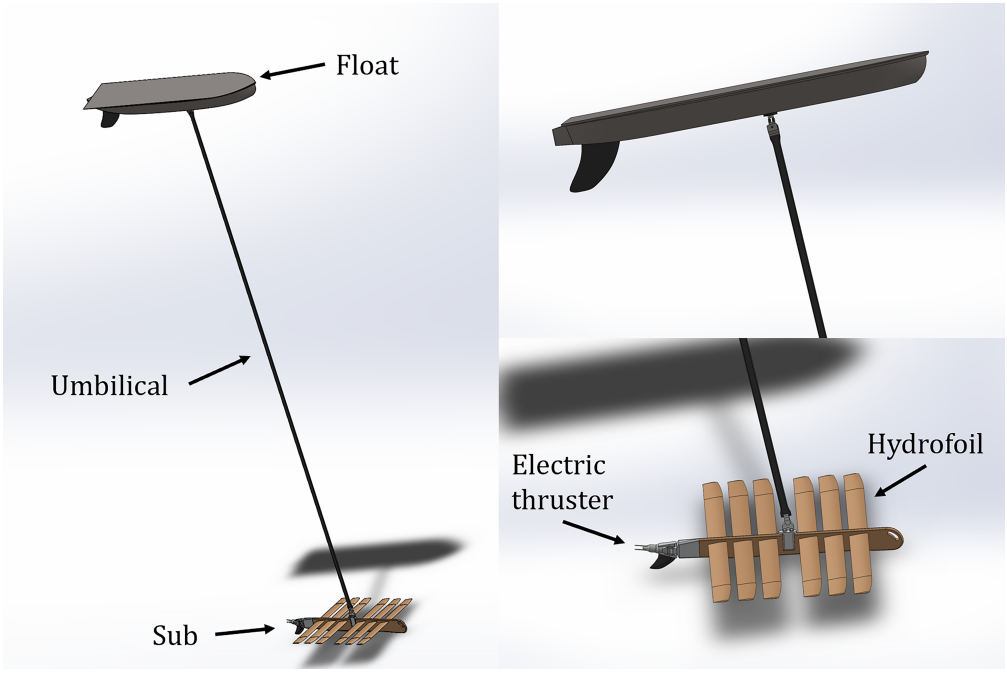


Figure 1.2: Model of a 3-Meter Scale Wave Glider

When it comes to utilization of wave motion by the wave glider, the outcome is that hydrofoils of the sub generate periodic mechanical propulsion force due

to the changes in kinetic energy of moving water particles. To understand this, let's first observe the water particles' motion of a linear water wave in deep-water condition, as shown in Figure 1.3. First, under ideal conditions, the trajectories of water particles can be regarded as closed circular orbits. Then, vertically downward from the free surface, the circumference of the water particles' trajectory becomes progressively shorter. However, since water particles at the same vertical position take the same amount of time to complete one circular trajectory, this will result in a reduction in the tangential speed of water particles at a deeper depth, that is, reduced wave motion.

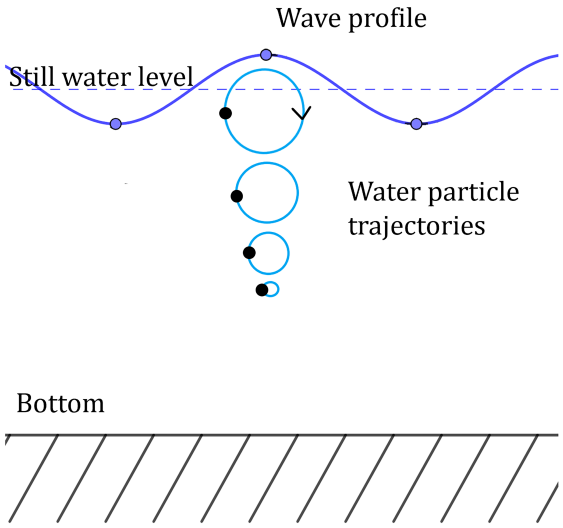


Figure 1.3: Simplified Water Particle Trajectories

As for the wave glider, its macroscopic motion is the rise and fall movements of the float carrying the sub along with wave crests and troughs through the attached umbilical. During this process, changes in vertical position of the sub causes the hydrofoils to be in a continuous and periodical changing wave motion field. And it is the difference of water particle motions that results in deflections of the hydrofoils, producing forward mechanical forces. The propulsive force of which acts on the sub and pulls the entire wave glider forward. It can be considered that hydrofoils are in a balanced posture in calm water. When waves lift the float, the sub moves upward in the vertical direction under the connection

of the umbilical to a position where the wave motion is greater, then the hydrofoils are deflected counterclockwise from the balanced position; when the float descends with wave troughs, the hydrofoils become deflected clockwise based on the same principle, as shown in Figure 1.4. And whether in an upward or downward posture, forces produced by deflections of the hydrofoils can divide a forward thrust for the wave glider.

Umbilical serves as connection between the float and the sub. It is made of a tether material with stiffness, as the medium for transmitting buoyancy and thrust between the float and the sub. At the same time, the electrical energy collected by solar panels can also be transmitted to the electric thruster and payloads mounted on the sub through a circuit passing the umbilical.

The structure of the wave glider determines its characteristics, long duration, low speed and diverse payload carrying capacity. Taking a 3-meter scale wave glider from Liquid Robotics as an example, its mission duration can be up to 12 months, its speed can reach 0.8 kn in sea state 2 and up to 2 kn (knot) in sea state 4 or higher sea conditions, it can carry a payload of up to 70 kg (kilogram) and has a towing capacity of up to 500 kg, finally, when equipped with an umbilical of 8 m, its minimum working water depth is 15 m [1].

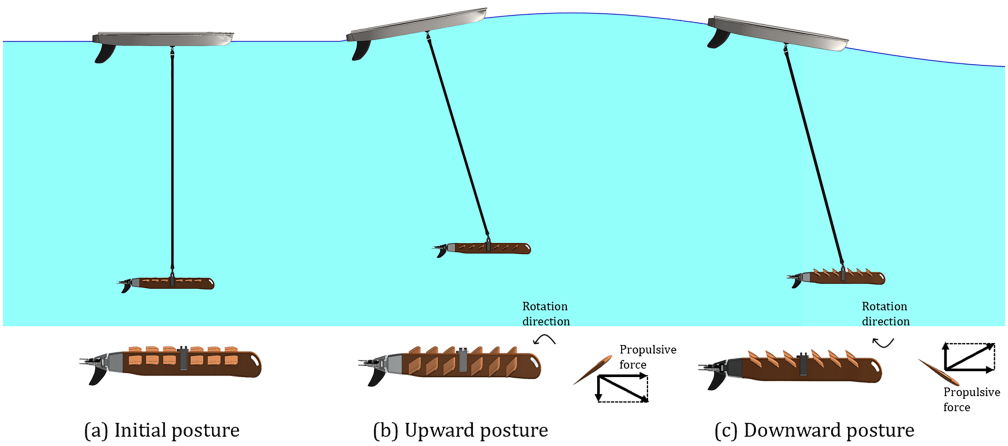


Figure 1.4: Schema of Propulsion through Wave Motion

For the float, which is always on the ocean surface, its dimensions, geometry, material and structure largely determine the payload-carrying capacity of the wave glider, its seakeeping ability in different sea conditions, and its survival ability in rough sea states. Therefore, the float is more of interest for this research.

1.1.2 Applications for Ocean Observation

In the field of ocean observation, the wave glider can undertake missions like hydrographic measurements on the sea surface, at the air-sea interface, and in shallow water layers, at the same time, it also has the capability of tracking and observing marine organisms as well as marine meteorology. In recent studies, the use of the wave glider to observe extreme ocean climate and related phenomena, such as the tropical cyclone (TC, also called typhoon or hurricane in specific regions), undersea earthquake and tsunami, has become a hot topic.

In 2012, the team of Lenain and Melville used a wave glider to observe and record data on a category [5] 3 TC “Freda” [2]. The wave glider approached the center of the TC about 46 km away and experienced rough sea conditions with winds of up to 37 m/s and significant wave heights of up to 10 m.

In 2016, Mitarai and McWilliams conducted observations of a category 4 TC “Danas” using a wave glider to study TC-induced air-sea processes [3]. The wave glider approached 15 km (kilometer) east of the typhoon eye area and collected atmospheric and oceanic data under extremely dangerous sea conditions.

In 2017, Tian *et al.* used the “Black Pearl” wave glider to observe three TCs “Hato”, “Pakhar”, and “Mawar” passing through the northern area of the South China Sea and recorded TC-induced surface wave data [4]. The collected data recorded intense changes of the surface wave, with the wave period increased from $4-6$ s to about $8-10$ s and the wave height increased from $0-1$ m to $3-8$

[5] The category of a tropical cyclone is usually based on the Saffir-Simpson Hurricane Wind Scale (SSHWS).

m.

Also in 2017, Son *et al.* used a wave glider to observe the impact of the TC “Talim” on the marine environment [5]. The wave glider approached the TC where the wind speed reached 25 m/s and the significant wave height reached 9.1 m, and measured the relevant oceanic data.

In other studies about the genesis of TCs, its numerical modeling, track and intensity prediction, Fitzpatrick *et al.* conducted observations of the oceanographic and atmospheric boundary layer conditions during the passage of TC “Hanna” using the wave glider [6]. Tian *et al.* deployed three wave gliders in the South China Sea and the adjacent Western Pacific region to observe TCs passing through, the sea surface wind structure of 8 TCs was recorded [7]. In order to improve the accuracy of their prediction model on TCs, Kosaka *et al.* used the wave glider to observe environmental changes induced by the category 5 TC “Hinnamnor” [8]. Thomas and Tarapore presented a method using a swarm of wave gliders to improve the accuracy and validity of TC observations [9].

In these observations focused on the TC, the wave glider needs to be as close as possible to the center of the TC and experiences rough ocean conditions, which challenges its survival ability in the face of high sea states.

1.1.3 Load Analysis

Marine structures are inevitably exposed to complex environmental loads, which could lead to material fatigue as well as structural failure. These loading factors are multifaceted and combined, such as the common loads caused by wind, waves and ocean currents. A simple load analysis of the wave glider is needed to identify the main factors affecting its structural safety. Therefore, it is first necessary to understand the main loading factors in the marine environment.

The impact of wind loads on marine structures is mainly related to the stability and overturning problems, specifically, the effects of wind-induced drag and

lift, which generates overturning moments and affects the stability of both floating and fixed structures [10]. However, the wind loads are usually considered as a secondary factor when carrying out load calculations, since the average static forces and moments induced by wind on marine structures represent only a small fraction of the total loads [11]. For structural analysis of ships, wind loads must be taken into account when the superstructure or its component can be significantly affected by wind forces. Wind loads need to be determined based on observed data for the sea area where the structure is located, and wind data typically include information on the frequency of occurrence, duration, and direction of wind velocity. Although *in situ* measurements are more efficient with appropriate instruments such as wave buoys and anemometers, traditionally, the wind velocity specified by the Beaufort Scale remains a rough reference. Table 1.1 shows the wind velocity and descriptive term corresponding to the 13 Beaufort Scale levels. By measuring wind data, the wind profile (variation of the mean wind velocity with a height above the still-water level) can be obtained. Combined with the geometric coefficient of the loaded structure, wind pressure, and wind forces can be calculated [11]. In more complex analyses, wind tunnel tests and computational fluid dynamics (CFD) methods can be employed.

Beaufort number	Descriptive term	Mean velocity [1](m/s)	Possible wave height (m)
0	Calm	$0-0.2$	$-$
1	Light air	$0.3-1.5$	0.1 (0.1)
2	Light breeze	$1.6-3.3$	0.2 (0.3)
3	Gentle breeze	$3.4-5.4$	0.6 (1)
4	Moderate breeze	$5.5-7.9$	1 (1.5)
5	Fresh breeze	$8.0-10.7$	2 (2.5)
6	Strong breeze	$10.8-13.8$	3 (4)
7	Near gale	$13.9-17.1$	4 (5.5)
8	Gale	$17.2-20.7$	5.5 (7.5)
9	Strong gale	$20.8-24.4$	7 (10)
10	Storm	$24.5-28.4$	9 (12.5)
11	Violent storm	$28.5-32.6$	11.5 (16)
12	Hurricane	32.6 and over	14 $(-)$

[1] Velocity equivalent at a standard height of 10m above open flat ground.

Table 1.1: Beaufort Wind Scale [a]

a. Data source: World Meteorological Organization. Manual on Codes, Volume I.1 – International Codes, Part A – Alphanumeric Codes, **2019**.

Wave is one of the most significant and dangerous environmental loads to marine structures. Intense waves can generate high loads on marine structures, and could result in significant displacements and deformation. Wave brings continuous dynamic loads that accelerates material fatigue. When analyzing the wave loads, not only wave impacts are necessary, other effects like green-water loading are also important to consider. The intensity of waves depends on different factors, such as wind velocity, the duration of which wind blow in the same direction, the fetch (extent of the surface over which the wind is blowing), and the water depth [12]. Waves take form by the interaction of wind with the free water surface, generated when the wind creates ripples on the water surface. As the wind continues, these ripples grow into waves, and gradually increase until the wave slope in deep water exceeds 1:7, finally resulting in the break of waves and preventing further energy absorption [12]. In some situations, waves can be fully developed, surpass the wind speed and propagate over long distances without energy loss. In fact, the continuous generation of waves, the wind loads which impose on waves during propagation, and their arrival in a new water area, all those make wave conditions a highly irregular factor. Thus, for a marine structure, the waves that it experiences can be completely random. However, according to the principle of superposition, an irregular wave system can be accurately described by a linear superposition of many regular wave components with different lengths, amplitudes, propagating directions, and phase angles [12, 13]. With wave conditions defined by mathematical form, the calculation of wave loads acting on structures and analysis of the structure's response can be done. Typically, structural analysis can utilize formulas provided by ship classification society, and wave data can be referenced from multiple marine meteorological and oceanographic database. For a rough understanding, Table 1.2 shows 10 sea state codes and the corresponding significant wave heights, and the data refers to well-developed wind waves in the open sea.

Ocean currents can be described as continuous, horizontal, and routed

Sea state code	Descriptive term	Significant wave height (m)
0	Calm (glassy)	0
1	Calm (rippled)	$0-0.1$
2	Smooth (wavelets)	$0.1-0.5$
3	Slight	$0.5-1.25$
4	Moderate	$1.25-2.5$
5	Rough	$2.5-4$
6	Very rough	$4-6$
7	High	$6-9$
8	Very high	$9-14$
9	Phenomenal	Over 14

Table 1.2: Sea State [a]

a. Data source: World Meteorological Organization. Manual on Codes, Volume I.1 – International Codes, Part A – Alphanumeric Codes, **2019**.

movements of seawater. Ocean currents impose static loads on marine structures, mainly including hydrodynamic drag, and frictional drag is a necessary factor to consider for large marine structures [13]. On the other hand, although not as dangerous as wave impacts, dynamic loads imposed by ocean currents could also cause material fatigue and damage structural safety [14]. While the impact of current loads on marine structures is more important than wind loads, there are fewer independent analyses of ocean currents loading cases in the literature. Perhaps that is because ocean currents are to some extent in fixed courses and avoidable.

Another type of environmental load comes from marine organisms. Marine organisms will gather on the immersed and unprotected surface of the structure, and form a biofilm in a short time. Initially, a thin film of organic matter will form on the surface within a few hours. This provides a habitat for marine microorganisms such as bacteria, fungi, or microalgae. And gradually, a microbial biofilm is formed. Subsequently, larger marine organisms, which mainly include barnacles and other invertebrates that can attach to a hard surface, will cover the surface. Those marine organisms cause load on the structure, change its stress conditions, increase resistance to heat exchange, and affect the hydrodynamic performance.

Finally, a factor that should not be forgotten is the pressure from the sea-

water. In general, using the atmospheric pressure at sea level (1 atm = 101325 Pa) as a reference, it is commonly considered that the pressure increases by 1 bar (1 bar = 100000 Pa) for every 10 m increase in depth. So, it is an increase of 1 decibar per meter of depth. Pressure has a significant effect on underwater structures, and the material strength of an underwater vehicle generally determines its ability to dive in depth.

Figure 1.5 below illustrates the main loading factors to which the wave glider is subjected in the marine environment.

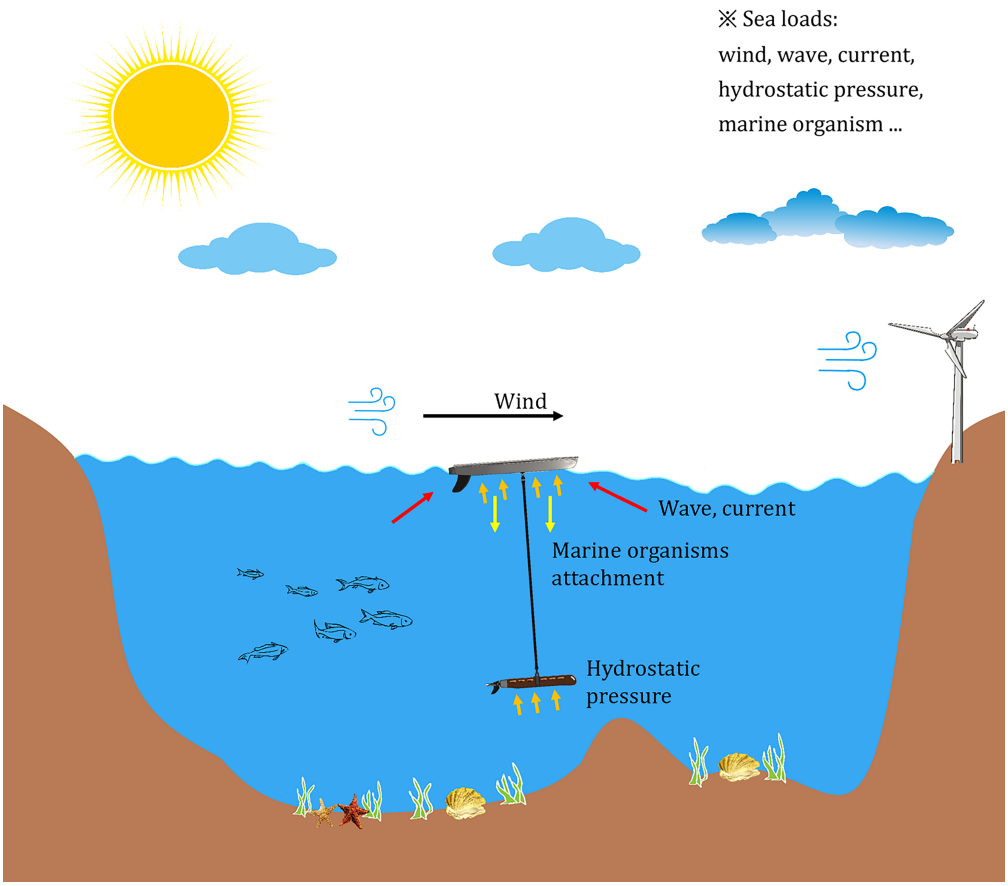


Figure 1.5: Marine Environmental Loads [a]

a. Image modified from "Marine environment", source: Peng, Y.; Ninaga, J.M.; Wang Z. Characterization of Marine Composites: A Comprehensive Review of Marine Materials in Shipbuilding, Their Mechanical Behaviors and Degradation Mechanisms. *Global Journal of Engineering Sciences* **2025**, *12(1)*.

For all environmental loads, it is necessary to distinguish which are the major factors affecting the structural safety of the wave glider. And in summary, this

study identifies that the wave loads (wave impacts) are the major factor affecting the material health of the wave glider's float structure. The other factors such as wind loads, ocean currents, attachment of marine organisms and hydrostatic pressure are considered as of minor importance.

First, wind loads can be an important factor when considering large marine structures, as their structures above the water surface generally have load-bearing surfaces in different directions. For example, the superstructure of a large vessel may be subjected to a large overturning moment in the face of side winds, while head winds usually bring resistance to sailing. The wave glider is small in dimensions and there are only a few mounted sensors on the upper surface of the float, so wind loads have little effect on it.

Then, the effect of ocean currents on a vessel structure remains mainly the impact on its navigation caused by seawater movement. And ocean currents move along fixed routes. Therefore, not only ocean currents have little influence on the wave glider, but take advantage of the currents' path as a way to increase sailing speed can also be considered.

In the meantime, since wave glider is still a surface vehicle, only the sub is working underwater and its depth will not exceed 15 m, the influence of hydrostatic pressure is negligible.

Next, the influence of marine organisms' attachment on the wave glider is mainly an increase in mass and it may act as an obstacle to navigational performance. When the main focus is on mechanical material fatigue and the effects of marine organisms in aging process of the material are not taken into account, the effect of marine organisms is a minor factor.

Finally, for wave loads, it is the major factor that needs to be considered. Marine structures are subjected to continuous cyclic loading during their working life, and these loads can harm the health of the material, leading to the propagation of cracks that exist in the material and causing fatigue damage. Yet, the fatigue damage is exactly one of the key failure modes of marine structures [15, 16].

Due to the irregularity of waves, the loads that waves exert on marine structures are very complex. For example, wave loads could occur anywhere along and across the hull of a ship. Nevertheless, there are some major wave load phenomena that threaten the safety of marine structures. In the work of illustrating the development of the prediction of wave-induced loads, Temarel *et al.* describe four major wave-loading phenomena, which are slamming, green water, sloshing and loads from abnormal waves [17].

Wave slamming occurs when a marine structure crosses the wave crests. This type of wave loading can be characterized as a short-period force or a rapid pressure pulse acting on the surface of a structure [18, 19]. A typical example is that when a high-speed vessel crosses the wave crests, its bow and stern sections are successively lifted out of the water by its speed or the large waves, and then slammed by the wave crest, or struck against the water surface, forming strong periodic impacts. Intense slamming impacts can significantly affect the behavior of a ship's hull structure. High-frequency slamming may lead to accelerated fatigue behavior of the hull material, accumulating fatigue damages and allowing the growth of cracks.

Green water is a wave loading phenomenon, where waves come into contact with marine structures and surge onto the structure, causing waves to break. And then, depending on geometry of the structure, running water of broken waves either flow on the deck or rush up to the superstructure. Impact of this portion of water may result in damage to deck materials or facilities installed on the deck.

Sloshing refers to the change in free surface of the liquid inside a container during unsteady movement, or upon impact. When the free surface changes drastically, it may endanger the structural safety of the container. At sea, it is generally associated with ships transporting oil or liquefied natural gas.

And for loads from abnormal waves, it usually involves focused waves or solitary waves, that is, the interaction of the structure with waves with extremely great wave heights. Such a strong impact may exceed the yield strength of the

material and cause failure of the structure.

Summarizing above analysis, on the one hand, wave loads that pose the greatest threat to the hull structure of the wave glider's float are slamming impacts as well as abnormal wave loads. Slamming loads occur when waves are relatively large, causing a part of the wave glider's float to be lifted out of the water and then strike the water surface or wave crest, potentially damaging the bow, stern, or side sections of the float. And when abnormal wave impact occurs, the float structure may suffer damage due to sudden and intense dynamic pressure loading. These wave loads are most likely to cause local damage to the hull structure. On the other hand, green water loads pose a risk of potential damage to solar panels and electronic equipment installed on the float. In the context of application scenarios, the wave glider is usually deployed for a long duration at sea (general operating conditions being sea states $2-4$), and the wave glider may experience extremely rough sea conditions (sea states $7-8$ depends on the intensity of the TC) when applied to the observation of TCs. Although the wave glider is a small-sized, low-speed surface platform, slamming, green water and abnormal wave loading are the possible wave impact scenarios. Therefore, local damage may initially develop on the hull structure of the float under high-energy wave impacts, followed by material fatigue under prolonged exposure to low-energy general wave impacts, ultimately leading to structural failure.

1.2 Marine Composites

Human's exploration and utilization of the ocean have witnessed the development of shipbuilding materials. Timber served as the main structural material for ships until the 19th century due to its accessibility, also buoyancy and strength that it provides. Then, the launch of the first iron-hulled warship "HMS Warrior" in 1860 marked the beginning of the transition from timber to metal,

which has gradually become the main structural material in modern shipbuilding [20]. The main advantage of metallic materials is their high strength, high stiffness and good toughness. The development of industrial metallurgy has promoted the mass production of metallic materials and their extensive use in shipbuilding. In the shipbuilding industry, steels and aluminum alloys are the most widely used structural materials, and other common materials include titanium and its alloys, copper alloys, cast iron, and so on [21].

However, the development of composite materials has made it an option to replace metals as the structural material, and the application of composite materials in the field of shipbuilding and offshore construction is showing an upward trend. The use of composite materials in shipbuilding can be dated back to around 1950, when glass fiber-reinforced polymer (GFRP, also called Glass Fiber-Reinforced Plastic) was first used in the construction of small vessels [22–25]. Composite materials combine the advantages of high mechanical performance and light weight. Also, in applications in the marine environment, composite materials provide good aging resistance, longer service life and lower maintenance costs. Beyond that, composite materials can meet requirements for specific applications, such as electrical insulation, non-magnetism, and electromagnetic wave transparency. As a structural material, GFRP has already occupied more than 90 $\%$ of the production market share for small vessels. And composite materials are increasingly being used in the construction of fishing boats, pleasure and sporting boats, commercial vessels, naval ships, submersibles, and offshore platforms [26].

The selection of composite materials is a complex process. In shipbuilding, for example, depending on dimensions of the product, laminated composites may be used for the construction of hulls for smaller vessels, and correspondingly, sandwich-structured composites may serve as a better choice for the construction of larger sized vessels. Reinforcement fibers in the composites are the main components that determine the mechanical performance of a structure. Then the selection of matrix material should be determined by reinforce-

ment fibers as well as marine environmental factors. Based on the consideration of mechanical characteristics, the discussion is focused on reinforcement fibers. GFRPs offer reliable mechanical properties and the advantage of low cost, making it suitable for the construction of small vessels. Aramid fiber reinforced polymers (AFRP) provide high mechanical performance, excellent impact resistance and fire resistance for applications in military-grade vessels and as a fireproofing material. Carbon fiber-reinforced polymers (CFRP) possess excellent mechanical properties and low-density characteristic that enable them to be used in the construction of high-performance vessels. In addition to these three main types of reinforcement fibers, basalt fibers have been widely studied as a potential alternative to glass fibers in the marine applications, and natural fibers have also become a hot research topic as biodegradable and easily recycled materials. Furthermore, hybrid composite materials that use multiple reinforcement fibers are considered for enhancing and optimizing the mechanical performance of structures. However, other types of composite materials, such as metal matrix composites, are not discussed in this study.

1.2.1 Application of Marine Composites as Structural Materials

Composite materials are constantly developing and they have been able to serve as the main structural material used in the construction of small and medium sized vessels, marine robots, superstructures of large vessels, offshore platforms, and so on. At the same time, composite materials are also used in the construction of the internal structure of marine structures and related equipment, replacing metal materials to improve the mechanical properties of marine structures, reduce costs and energy consumption.

Stewart noted in his study that Europe and the United States represent the largest markets for recreational boats, and for the majority of these boats, their hulls, decks and other components are constructed from fiber-reinforced plastics (FRPs) [27]. Neşer's research in 2016 indicated that the share of com-

posite materials used in the ship and boat building industry had reached 6 $\%$, and especially for the construction of small vessels with an overall length up to 50 m, the share of composite materials usage had been as high as 70 $\%$ [28]. As composite vessels gradually move to larger dimensions, a study by Baley *et al.* noted that "Bureau Veritas" has currently introduced rules for certification of composite hulls up to 90 m in length [29]. Furthermore, the study indicates that the length of hulls constructed from composite materials has steadily increased over time, and the composite-built hull for naval vessels have reached $80-90$ m in length, but this trend seems to have stopped after entering the 21st century. This may be due to a number of factors such as composite materials performance, associated shipbuilding processes, and the cost of construction and maintenance over the service life that make large composite vessels less economically attractive than steel vessels.

Applications of composite materials in racing boats can significantly reduce weight and improve the sailing performance. Marsh reported in his research that the French foiling trimaran "Hydroptere" has become the first sailboat to break the speed barrier of 50 kn, and that the incredible sailboat "SailRocket 2" has achieved a world record of 65.45 kn. Without a doubt, those two are both made of carbon fiber-reinforced composite material [30].

In several review studies, applications of composite materials in naval vessels are presented, and some of the famous cases are as follows [31–33].

Due to their electromagnetic wave transparency characteristic, the composite materials are well suitable for the construction of mine countermeasure vessels which are not very large in dimensions. "HMS Wilton (M1116)" was the first minehunter constructed with composite materials, launched in 1972, built of glass-reinforced plastic (GRP), with a length of about 46.6 m, and a displacement of about 450 t (tonne). The "HMAS Rushcutter (M80)" is a minehunter launched in 1986, approximately 31 m long, with an innovative catamaran hull design. The hull is constructed of a sandwich structure composite material, with 8 mm (millimeter) thick GRP as the skin and 60 mm thick high-density Polyvinyl

chloride (PVC) foam as the core material.

Another classic example of the use of composite materials in naval vessels is the “Visby” class corvettes of the Swedish Navy. The “HSwMS Smyge” experimental vessel was first launched in 1991 to test the stealth technology in ships built from composite materials. The experimental vessel is about 30 m long and it is made of a sandwich structure composite material. The skin of this sandwich composite is made of carbon fiber/glass fiber/Kevlar fiber with a vinyl ester matrix, and PVC foam is used as the core material. Later, the “Visby” class corvettes were designed and built on the basis of the “HSwMS Smyge” with a length of more than 70 m, about 72.7 m, a beam of about 10.4 m, and the displacement reached about 640 t. This class of corvettes also uses a sandwich structure composite material for the hull, the skin material is reinforced with a hybrid of carbon and glass fibers, and the core material is a kind of PVC foams.

It has been mentioned in some review research that the length of composite-built vessels in various countries’ naval projects may reach 80$-$90 m or even more than 100 m, but there have been no reports of any such vessels being launched for the time being.

However, composite materials can also be used for the superstructure of large vessels. For example, the French Navy was the first to have a large warship equipped with a composite superstructure. The superstructure of the “La Fayette” class frigates is made of sandwich composite material reinforced by glass fiber, and the funnel is also constructed of composite materials.

With the development of marine unmanned vehicles, the use of composite materials to build the hull of an unmanned surface vehicle has become the preferred option. Asgharian and Azizul presented some typical examples of USVs, such as “AutoNaut” which is made of glass fiber-reinforced composite material and “C-Enduro” which is made of carbon fiber-reinforced composite material [34]. The study pointed out that fiber-reinforced polymers have represented the favorable choice of hull material for USVs. In their review research on USVs, Luo *et al.* noted that the use of composites to build USVs can provide a balance

between performance and cost [35]. In addition, in a study on USVs, Ghazali *et al.* concluded that from the point of view of the hull design, carbon fiber-reinforced composites have been the popular choice for building hull structure of USVs, despite the relatively high cost [36].

For the wave glider, although few studies have detailed the materials that it uses, it can be learned from some information on the web that its float may employ the sandwich-structured composite material as the hull material [6], while the skin is made of glass fiber-reinforced polymer.

1.2.2 Reinforcement Fibers

The major consideration for composite materials used to construct marine structures remains their mechanical properties. For applications of fiber reinforced polymers as structural materials in marine environments, common reinforcement fibers include glass fibers, aramid fibers and carbon fibers. Other reinforcement fibers with development prospects include basalt fibers and natural fibers.

Faced with the marine environment, the glass fiber provides high strength, good humid resistance, good chemical resistance, and cost-effectiveness. The industrial production of glass fibers began in the United States in the 1930s. As a matter of fact, the term “glass” refers to a large family of materials. It can be described as amorphous bodies obtained by supercooling a melting composition, during the process, the viscosity increases gradually until it becomes mechanically solid. Under massive form, glass is characterized by very high fragility and it is easy to crack. Nevertheless, glass can be produced in the form of fibers with small diameters, then these fibers lose the characteristics of fragility and exhibit excellent mechanical properties. In simple terms, the production of glass fiber involves extruding molten glass through a bushing, cooling the filaments with water, applying a chemical size, and then gathered and wound onto a tube that

[6] A photo shows the damaged float of a wave glider, https://www.mbari.org/news/the-challenges-of-sending-equipment-out-to-sea/.

is slid onto the collet. This concerns the melt spinning process, the process produces glass fibers with various diameters, typically ranging from 4 μm (micrometer) to 32 μm. Glass filaments are then coated with a chemical coating or size, the sized filaments are finally collected into bundles, forming a glass strand composed of 51 to 1624 filaments [37, 38]. By applying the chemical size, it is possible to achieve several important functions: establish a certain cohesion between filaments; provide a greater or lesser stiffness to the filaments; protect the filaments against abrasion; prevent the appearance of electrostatic charges; facilitate the impregnation of filaments to the resin matrix; promote the bond between glass fiber and matrix, which is crucial for the mechanical performance of the composite material; influence the behavior of the material with aging, sensitivity to humidity, corrosion, and other factors [38].

The first continuous glass fiber came to industrial production has good electrical insulation properties and is called electrical glass, or more commonly E-glass. Glass fibers vary widely, the letter designations are used to imply their special properties, for example, the “E” in E-glass stands for electrical. Generally speaking, glass fibers are categorized into two major classes: general-purpose glass fibers and special-purpose glass fibers. The former type, mainly the E-glass, occupies over 90 $\%$ of market share of the glass fiber. The latter includes S-glass, D-glass, C-glass, M-glass, A-glass, AR-glass, and others. For example, S-glass is designed for aerospace applications, the letter “S” stands for strength.

E-glass fiber has a low electrical conductivity, it is the most economical and widely used fiber for civil applications, and it is extensively used in working environments that require both strength and high electrical resistivity. Because of environmental regulations in the United States and Europe that forbid the emission of boron into the air, E-glass fibers can be classified as boron-containing glass fiber and boron-free glass fiber, depending on their origin. The mechanical properties of these two types of E-glass fibers are almost the same, the major difference is their acid resistance. The acid resistance of boron-free glass

fiber is more than seven times higher than that of boron-containing glass fiber [39]. In contrast, S-glass and R-glass are high-performance glass fibers that have higher mechanical strength and modulus compared to E-glass. They are typically 10 $\%$ to 15 $\%$ stronger at room temperature and they also provide better fatigue resistance [40]. These high-strength glass fibers are typically used in structural applications and they can be used in high-temperature operating environments. Up to now, E-glass, S-glass and R-glass represent the most suitable glass fibers for structural components in the marine environment. Table 1.3 shows some mechanical properties of E-glass, S-glass and R-glass.

Glass fiber	Density (g/cm^3)	Tensile strength (MPa)	Young's modulus (GPa)	Elongation ($\%$)
Boron-containing E-glass	2.54−2.55	3100−3800	76−78	4.5−4.9
Boron-free E-glass	2.62	3100−3800	80−81	4.6
S-glass	2.48−2.49	4380−4590	88−91	5.4−5.8
R-glass	2.54	4135	85.5	4.8

Table 1.3: Mechanical Properties of Glass Fibers [a]

a. Data source: Peng, Y.; Ninaga, J.M.; Wang Z. Characterization of Marine Composites: A Comprehensive Review of Marine Materials in Shipbuilding, Their Mechanical Behaviors and Degradation Mechanisms. *Global Journal of Engineering Sciences* **2025**, *12(1)*.

Aramid fibers can provide high specific strength (tensile resistance), stiffness, impact resistance, vibration absorption, chemical resistance, and flame resistance for marine applications. Aramid fiber is a type of organic synthetic fiber, the term "aramid" indicates wholly aromatic polyamides. The definition given by the U.S. Federal Trade Commission is more accurate that aramid fibers are manufactured fibers in which the fiber-forming substance is a long-chain synthetic polyamide in which at least 85 $\%$ of the amide linkages (the amide bonds -CO-NH-) are attached directly to two aromatic rings [41]. Commercial products of aramid fiber can be generally categorized into meta-aramid fibers, para-aramid fibers, and aramid copolymer fibers. The term "meta-aramid" stands for polyamide compositions which contain largely meta-oriented phenylene segments. The para-aramid fiber means that it contains a significant proportion of para-oriented cyclic units. Correspondingly, aramid copolymer fibers represent

those containing a combination of para-phenylene units and meta-phenylene units. The famous product “Kevlar” of DuPont Company (DuPont de Nemours, Inc.) is a type of para-aramid fiber. Para-aramid fibers like Kevlar can provide mechanical properties, impact resistance, and cut resistance while maintaining heat and chemical resistance. For example, Kevlar is often used for ballistic protection applications. Other para-aramid fibers include Twaron (Teijin), Taparan (Yantai Tayho). Meta-aramid fibers can provide outstanding heat resistance, flame-retardant property, chemical resistance, electrical insulation capability, as well as good textile property. Commercial products of meta-aramid fibers include Nomex (DuPont), Teijinconex (Teijin), Newstar (Yantai Tayho). Then, Technora (Teijin) is a type of aramid copolymer fiber product, it can provide high strength and high modulus, good heat and chemical resistance, good fatigue resistance, low creep property, and lower moisture regain property.

The production of continuous filament yarn of aramid fiber is achieved through the liquid crystalline spinning process, which involves forming a solution of the soluble liquid crystalline polymer or a melt-processable liquid crystalline polymer and spinning into filaments. Since the base polymer tends to decompose near its melting temperature, melt spinning is not utilized. Instead, the base polymer is dissolved in a solvent to form a liquid crystalline solution, and then filaments are produced through dry spinning, wet spinning, or dry-jet wet spinning processes. Taking the production of Kevlar using the wet spinning process as an example, as the polymer concentration increases, the orientation of the polymer chains changes, eventually forming an ordered and stable state, which greatly enhances the strength. Before the polymer concentration reaches 10 $wt\%$ (mass percentage concentration), the viscosity of the solution linearly increases with the increasing polymer concentration. At this point, the solution is isotropic, and the polymer chains have no preferred orientation, forming with random coil structures. When the polymer concentration reaches between 13 $wt\%$ and 20 $wt\%$, the solution viscosity remains at a lower and relatively constant level. At this stage, the polymer chains mainly consist of rods in liq-

uid crystalline arrays, exhibiting a high axial orientation independent of position, and the solution becomes anisotropic. This is because aromatic fiber molecules have good regularity in their main chains, containing rigid mesogenic units. With increasing concentration, they can align side by side to form a parallel arrangement in the liquid crystal state, leading to a high degree of molecular chains segment order. The polymer solution reaches its maximum solubility and remains stable at a temperature of $80\,^{\circ}\mathrm{C}$. Next, the polymer-containing solution is extruded through a spinneret, forming filaments. The resulting filaments by spinning exhibit a further high level of parallel orientation to the fiber axis, which is the reason why this fiber has high tensile strength [42].

For marine applications, Nomex (meta-aramid fiber) can replace the asbestos which is toxic, reducing weight and increasing strength and stiffness of the structure. Kevlar (para-aramid fiber) have higher strength and stiffness compared to E-glass and it can be considered for the construction of structural components, like ship hull and deck. Kevlar can be used for military vessels of which ballistic protection is required, and it can also be used for racing vessels in order to achieve the absorption of vibrations. However, Kevlar is more expensive and it presents processing challenges as that it is difficult to be cut. Table 1.4 shows the mechanical properties of some aramid fibers.

Aramid fiber	Density (g/cm^3)	Tensile strength (MPa)	Young's modulus (GPa)	Elongation ($\%$)
Teijinconex	1.38	620−690	7.9−9.8	35−45
Kevlar 29	1.44	2900	70	4.0
Kevlar 49	1.45	2900	135	2.8
Kevlar 149	1.47	2300	143	1.5
Technora	1.39	3400	72	4.6

Table 1.4: Mechanical Properties of Aramid Fibers [a]

a. Data source: Peng, Y.; Ninaga, J.M.; Wang Z. Characterization of Marine Composites: A Comprehensive Review of Marine Materials in Shipbuilding, Their Mechanical Behaviors and Degradation Mechanisms. *Global Journal of Engineering Sciences* **2025**, *12(1)*.

Carbon fiber is a type of high-performance fiber. It can provide high strength (tensile and compressive), high stiffness, low density, good humidity resistance,

and excellent chemical resistance for marine structures. Carbon fiber can be characterized as a type of fiber which is primarily composed of carbon atoms with the carbon content greater than 92 $\%$. And when the carbon content reaches 99 $\%$, it can be distinguished as graphite fiber. The definition of graphite fibers is rather vague, and there are some other criteria that can be introduced besides the carbon content, such as the heat treatment temperature greater than $1700\,^{\circ}\mathrm{C}$, the elastic modulus greater than 50 Msi (units of million pounds per square inch, approximately 344.74 GPa), 3D ordering of carbon atoms, and high degrees of preferred orientation [43, 44].

The prospects for the application of carbon fiber were not discovered until 1960 when Roger Bacon first experimentally produced graphite whiskers and demonstrated their excellent mechanical characteristics. The produced graphite whiskers presented an extremely high tensile strength property of about 20 GPa and the modulus property of at least 700 GPa [45]. Carbon fibers have a special characteristic of dynamic performance that carbon fiber products offer a wide range of mechanical properties. This is due to the anisotropy of the graphite crystal's structure which makes up the carbon fiber, this nature prevents the formation of a very high strength and very high modulus at the same time. The crystallographic structure of a perfect single crystal of graphite is composed of many sheetlike layers of carbon atoms which are stacked on top of each other. Thus, in the direction parallel to these planes, the crystal possesses extremely high theoretical tensile modulus of elasticity and ultimate tensile strength, separately on the order of 146 Msi (about 1000 GPa) and 15 Msi (about 100 GPa). Instead, the sheet-like layers of carbon atoms are connected by weaker Van der Waals bonds. So, in the direction perpendicular to the sheet planes, the theoretical tensile modulus of elasticity is only on the order of 5 Msi (about 35 GPa).

Carbon fibers are produced through the thermal conversion (controlled heating, stretching treatments, and pyrolysis) of carbonaceous precursor fibers. In addition to carbon fibers produced based on the three main precursors men-

tioned earlier, there are also vapor-grown carbon fibers. The carbon fiber market is primarily dominated by polyacrylonitrile-based (PAN-based) carbon fibers and pitch-based carbon fibers. PAN-based carbon fibers are the most popular choice in various sectors such as industrial, automotive, marine, construction, aerospace, and sports, making up the majority of the carbon fiber product market. Pitch-based carbon fibers, on the other hand, are known for their exceptional high-temperature resistance and find their main applications in special fields like aerospace and nuclear energy. PAN-based carbon fibers are extensively discussed in many publications, the production process includes the production of precursor fibers, oxidization, carbonization, graphitization, surface and sizing treatment. During the oxidization stage this step, the precursor fiber is converted from a linear polymer structure to a highly condensed, thermally stable ladder polymer structure, helping maintain molecular and fibrillar orientations during subsequent heat treatment. During stabilization, the PAN fiber is also stretched under tension to prevent shrinking and ensure the orientation of molecular chains, thus obtaining high modulus carbon fibers. Carbonization involves the thermal decomposition of stabilized PAN fibers to remove non-carbon elements (nitrogen and hydrogen) and increase carbon content. The graphitization step is used to produce further high modulus fibers and is carried out in an inert atmosphere, typically argon, at temperatures of around $3000\,^{\circ}\mathrm{C}$. During this step, the graphitic structure, crystallite size, and preferred orientation are enhanced. However, high temperatures can introduce flaws that may reduce the fiber's strength. Finally, the surface and sizing treatment is performed to improve the fiber-to-resin interfacial bond strength of carbon fibers [38, 39, 46, 47].

Carbon fiber's high strength and chemical resistance make it an excellent alternative to metal materials for building structural components of larger vessels, such as the hull, superstructure, propeller and other key components. At the same time, carbon fiber's properties of lightweight, high strength, vibration absorption and fatigue resistance make it suitable for use in water racing sports such as the construction of canoes, kayaks, sailboats, powerboats, and high-

performance crafts.

The mechanical properties of carbon fibers depend on the type of precursor and the processing technology. According to the mechanical properties obtained, carbon fibers can be categorized into the following types: Low modulus (refer to the standard modulus in some literature), Intermediate modulus, High modulus, Ultrahigh modulus, and High tenacity (refer to tensile strength). Table 1.5 shows the mechanical properties of PAN-based carbon fibers. And Table 1.6 shows the mechanical properties of pitch-based carbon fibers.

Characteristic	Density (g/cm^3)	Tensile strength (MPa)	Tensile Modulus (GPa) (GPa)	Elongation $(\%)$
Standard modulus	1.8	3340−4820	220−240	1.5−2.2
Intermediate modulus	1.8	4130−6200	275−295	1.3−2.0
High Modulus	1.9	4130−5515	340−440	0.7−1.0

Table 1.5: Mechanical Properties of PAN-based Carbon Fibers [a]

a. Data source: Peng, Y.; Ninaga, J.M.; Wang Z. Characterization of Marine Composites: A Comprehensive Review of Marine Materials in Shipbuilding, Their Mechanical Behaviors and Degradation Mechanisms. *Global Journal of Engineering Sciences* **2025**, *12(1)*.

Characteristic	Density (g/cm^3)	Tensile strength (MPa)	Tensile Modulus (GPa) (GPa)	Elongation $(\%)$
Low modulus	1.9	1300−3100	170−240	0.9
High modulus	2.0	1800−2750	375−620	0.5
Ultrahigh modulus	2.2	2410	685−965	0.3

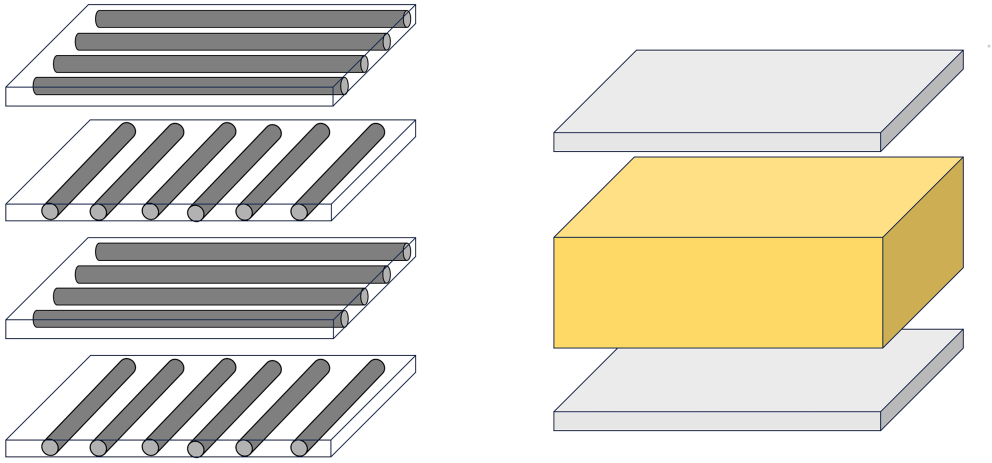
Table 1.6: Mechanical Properties of Pitch-based Carbon Fibers [a]

a. Data source: Peng, Y.; Ninaga, J.M.; Wang Z. Characterization of Marine Composites: A Comprehensive Review of Marine Materials in Shipbuilding, Their Mechanical Behaviors and Degradation Mechanisms. *Global Journal of Engineering Sciences* **2025**, *12(1)*.

1.2.3 Structure and Matrix

In marine applications, non-structural composite materials as well as structural composite materials are both possible to be used. For example, in the construction of small vessel hulls, discontinuous fibers are used to fill in areas where thickness rather than strength is needed, although such fiber forms

of non-structural composite materials are not sufficient to provide strength and stiffness. The continuous, oriented reinforcement fibers are the primary part that provides strength and stiffness. When it comes to the application of building structural components of vessels, the structure of fiber-reinforced composite materials is mainly composed of laminated composites and sandwich-structured composites. Figure 1.6 below shows the composition of a laminate composite and a sandwich composite.



(a) Laminate composite with fiber orientation 0°/90°/0°/90°

(b) Sandwich composite with foam core

Figure 1.6: Structure of Laminate Composite (a) and Sandwich Composite (b)

Laminated composite materials usually refer to the structure of a composite material that consists of a set of layers overlapping in parallel, and with perfect joining between the layers. Each layer can have its own specific composition of reinforcement fibers, including their form and orientation. Layers can be not only impregnated fibers but also pre-processed prepregs. Each layer can provide its mechanical properties depending on the orientation of its fibers. And in order for the laminated composite to remain perfectly jointed as a whole, the matrix needs to be identical across every single layer. Common laminated composite materials include unidirectional, bidirectional, multidirectional or random oriented. As a matter of course, laminated composite materials can also be

components that are axisymmetric or have complex geometry.

Sandwich-structured composite materials consist mainly of skin materials along with a core material to form a sandwich composition. The skin materials and the core material are joined by means of an adhesive substance. The skin material can be a laminated composite, while the core material typically includes cellular foam, cellular wood (balsa), honeycomb structured materials, thermoplastic materials, or a mixed core material. For laminated skins, they support external stresses. And the core's role is to transmit the stresses between the skins. The core can also help to provide good rigidity, particularly in a bending condition. The selection of the core material could be determined based on the structure's requirements in terms of mechanical properties. For example, balsa wood as the core material can provide characteristics such as lightweight, buoyancy, vibration absorption, thermal insulation, and compatibility with different resins, that make it suitable for the construction of hulls that require lightweight and sailing speed. Accordingly, for the hulls of medium to large-sized vessels, where the stiffness provided by the core material is more important, a closed cellular foam material, such as PVC, could be the preferred choice.

The selection of a composite's matrix material requires consideration of a number of factors, such as marine environmental factors, mechanical property requirements and compatibility with reinforcement fibers. For fiber-reinforced composite materials used in marine environments, the matrix mainly consists of resins such as polyester, vinyl ester, epoxy, and phenolic resins.

The mechanical properties of the matrix are also one of the important factors to consider when selecting the matrix for building the structural components of vessels. Polyester, vinyl ester and epoxy resins can all provide good mechanical properties. Polyester resin is often paired with glass fiber for hull construction and it is an economical choice. In contrast, the mechanical properties of vinyl ester resin are better than those of polyester and it provides good resistance to chemical attack, moisture absorption and hydrolysis [31, 48]. Vinyl

ester resin can enable the structure to be more flexible and to have higher hardness, thus providing improved fatigue resistance [49]. At the same time, vinyl ester resin provides good resilience and enables the realization of larger-sized structural components, which is frequently used in the construction of naval vessels. However, compared to the former two, epoxy resin offers superior mechanical properties, with higher modulus, tensile strength and better elongation property, and it also has good processability and eco-friendly characteristic [31]. But epoxy resin is also more expensive. In addition to these, the use of phenolic resin often takes into account the fire resistance needs of the structure, which can withstand temperatures of up to $200\,^{\circ}\mathrm{C}$, and it produces very few fumes and toxic gases. Nevertheless, phenolic resin does not have favorable mechanical properties.

1.3 Wave Load Calculation Method

The calculation and analysis of wave loads are an important part of the design of marine structures. The static and dynamic loads induced by waves are important factors that lead to the fatigue of marine structures and determine their safety and durability [14]. Frequently used methods for obtaining wave load data include the empirical method, the physical experiment and the numerical simulation.

In the case of empirical method, Morison's equation and its improved formulations are often used to calculate the wave-induced hydrodynamic forces acting on floating structures. Usually, the application of the Morison's equation requires a condition that the characteristic dimension of the floating structure should be smaller than the wavelength parameter [50]. Therefore, it is more commonly used for load analysis of offshore wind turbines or small-scale structures.

Physical experiment usually refers to the method of performing scaled-

down simulation experiments in a physical wave tank. Wave tanks, depending on their specifications and complexity, can generate different water wave conditions through the movement of individual or grouped wavemakers, whether it is regular waves or irregular waves. And the scaling lows will be employed to evaluate the real water wave effects. This approach involves the construction of a wave tank, the construction of a structure model, the sensors for data collection, and so on. And this needs expensive investment.

With the increase of computational power and the development of related CFD software, numerical simulation has become one economical and reliable method to compute the wave loads. This approach involves either building numerical wave tanks through CFD software or modeling the simplified fluid-structure problem. Also, numerical simulation can improve the efficiency of load calculation under different wave conditions. However, it is worth noting that the wave load data obtained through numerical simulations still need to be verified by theoretical results or physical experiments.

1.3.1 Numerical Wave Flume

The construction of a numerical wave flume is an effective method used to generate and study various wave phenomena. Wave generation is based on wavemaker theory as well as different wave theories. Well-known water wave theories include linear water wave theory (also called Small-amplitude theory or Airy wave theory), nonlinear finite amplitude wave theory (Stokes wave theory), Boussinesq wave theory, Cnoidal wave theory, Solitary wave theory, and other complex theories used to study particular water wave phenomena. Certainly, it is feasible to carry out the study of a fluid-structure interaction (FSI) problem through a numerical wave flume, which needs the target structure to be coupled into the wave flume model. In order to compute wave loads, it involves actually the simulation of wave generation, water wave impacting the structure and the computation of mechanical response of the structure through an appropriate

coupling method.

The simulation of different wave conditions needs to follow the appropriate wavemaker theory. Piston-type wavemaker and flap-type wavemaker are two most commonly used approaches for the generation of water waves. The selection of wavemaker type can depend on different water depth conditions, and existing research has suggested that the piston-type wavemaker is more suitable for intermediate and shallow water environments, while the flap-type wavemaker works well for the deep-water conditions [51–53]. Anbarsooz *et al.* modeled numerical wave tanks with piston-type wavemaker and also with flap-type wavemaker, linear and nonlinear waves were generated under intermediate water depth condition and deep-water condition, and the models of numerical wave tanks were validated by comparing the experimental data [54]. Park *et al.* modeled a piston-type numerical wave tank based on the Boussinesq equation in order to study the cnoidal waves and solitary waves, and the mean power characteristic range of the related theories was then verified [55]. Francis *et al.* also modeled a piston-type numerical wave tank to study solitary wave phenomena [56].

For the numerical simulation of water waves, the treatment of reflected waves is one of the major factors that need to be considered, which will directly affect the accuracy of generated water waves. Miquel *et al.* studied different wave generation methods for CFD-based numerical wave tanks, related wave absorption methods were also analyzed [57]. Ohyama and Nadaoka modeled a numerical wave tank with open boundary conditions, the sponge layer and the Sommerfeld's radiation condition were applied to eliminate wave reflections, then, the generation of nonlinear and irregular waves were studied [58].

The modeling of numerical wave tanks to study the FSI problem is also one of the research hotspots. Hu *et al.* modeled a numerical wave tank to study the FSI problem, first order and second order Stokes waves and the extreme wave were respectively generated, the responses between these waves and a cylindrical structure under floating or fixed conditions were simulated [59].

Westphalen *et al.* modeled a numerical wave tank to study the interactions between focused waves and the structure, the numerical wave tank model was validated and related simulation results were approved through comparing the experimental data [60].

1.3.2 Fluid-Structure Interaction Simulation

Fluid-structure interaction problems typically concern the responses between a structure, rigid or deformable, and the fluid flows surrounding or inside that structure. When it comes to water waves impacting a structure, the generated waves propagate and reach the structure, and the impact process is completed in a very short period of time, where large material deformations may present. This FSI problem involves the target structure, the seawater in contact with the structure, and the air layer surrounding the structure located at the water surface. Thus, the typical numerical approach of finite element method (FEM) for this type of FSI simulations usually needs to deal with both solid and fluid elements in one model. And it is inevitable that fluids may be present in the same element cell in this case. Conventional finite element numerical simulations usually use Lagrangian method or Eulerian method, both methods have their own advantages and disadvantages when dealing with solid computation or fluid computation individually. When using the Lagrangian description, the interface between different materials can be easily traced because the mesh nodes depend on and follow the movement of the material nodes during the computation process. However, when large material deformation occurs, a remesh process of the grid may be required and this can cause mesh distortion and lead to erroneous computation. Accordingly, the Eulerian description is commonly used for fluid problems, and it has no problem in cases of large deformations of materials since the mesh nodes are fixed and only the material nodes are allowed to move. Yet, in this case, the interface tracking issue becomes difficult. In other words, when both solid element and fluid element

are present in the model, the use of Lagrangian or Eulerian methods alone cannot efficiently solve the problem when large deformation occurs, as well as the problem of tracking the fluid-structure interface, which can lead to mesh distortion and computational instability. Consequently, suitable method needs to be applied to deal with such problems in FSI simulations.

The Arbitrary Lagrangian Eulerian (ALE) method is one of the methods often used to solve FSI problems. This method was specifically developed to address the above-mentioned problems in a FE numerical simulation of FSI problems. The ALE method was proposed by Hughes *et al.* and subsequently further investigated by Donea *et al.* [61, 62]. Their research described the ALE formulation and the coupling algorithms in detail, and a number of FSI examples were demonstrated to present the great development potential of the ALE method. This method combines the advantages of Lagrangian method and Eulerian method. The ALE description introduces a referential domain that can be displaced arbitrarily, this referential domain permits the possibility of the ALE method to deal with FSI problems where Lagrangian and Eulerian elements present together, and where large deformations may occur.

The interface tracking issue in the simulation of the FSI problems, on the other hand, can be solved by the Volume-of-fluid (VOF) method or Young's method. And for the calculation of contact forces between the structure and fluids in the FSI problems, a contact algorithm based on the penalty method is the commonly used.

The ALE method has been proven by many research to be an effective approach for solving the FSI problems. Relevant FSI problems include airbag inflation, bird impact, soil-structure interaction, sloshing tanks, slamming phenomena and underwater explosion. Hughes *et al.* described the FE formulation of incompressible viscous flows based on the ALE method for solving the free surface and relevant FSI problems [61]. Souli and Zolesio solved the free surface problem of viscous and incompressible flows by the ALE method [63]. Souli and Gabrys simulated the problem of bird impact into an aircraft radome using

ALE method and validated the model through experimental data [64]. Souli and Shahrour analyzed the effect of blast loading on a soil-structure system using the ALE method [65]. Ozdemir *et al.* simulated the sloshing tank response under earthquake conditions using ALE method, the coupling forces between water and tank material were calculated and their results were validated by comparing analytical results in other research [66]. Aquelet *et al.* simulated the slamming phenomena in the shipbuilding industry through ALE method [67]. Gong conducted an underwater explosion simulation using the ALE method for calculating the response of a submersible hull build of glass/epoxy composite due to explosive shock and bubble [68].

Above investigation illustrates that it is feasible to use the ALE method to simulate the scenario of water waves impacting a structure and to compute the wave loads. The wave generation of water involves the resolution of the free surface problem, similarly in the sloshing tank problem. And the computation of coupling forces between the structure and fluids has also been presented in the literature.

1.4 Conclusion

The investigation of research context permits a better understanding of the research subject and the establishment of research objectives.

This research aims at the wave glider, a small-sized hybrid surface vehicle that consists of a float on the water surface, a glider sub underwater capable of harnessing the wave motion energy, and an umbilical cable that connects them together. The characteristic of the wave glider is its ability to achieve long-duration missions by harvesting solar energy and converting wave motion energy into propulsion. This means that the wave glider will need to go through prolonged wave impact scenarios. And for applications, the wave glider can be deployed for the observation of extreme ocean climates such as the tropi-

cal cyclone. This requires the wave glider to approach as close as possible to the center of a tropical cyclone where the sea state is extremely rough, and to make continuous tracking and measurements. This means that the wave glider needs to be capable of withstanding intense wave impacts, placing demands on the safety of its structure, especially hull structure of the float. Furthermore, the analysis of environmental load factors affecting the structural safety of the wave glider also showed that the main environmental loads threatening the wave glider's safety are wave loads. It is clear that the subject of this research lies in the investigation of mechanical responses of a wave glider's float that is subjected to wave impacts. Understanding and analyzing wave load data can help guarantee the structural safety and durability of the wave glider from the structural design level of the float's hull structure.

By analyzing the available information, it can be learned that the hull structure of the wave glider's float is made of a sandwich-structured composite material. Composite materials used in marine environments provide sufficient mechanical strength and stiffness, and possess the characteristics of aging resistance and long service life in marine environments, making them a reliable alternative to metal materials in the shipbuilding industry and the construction of offshore structures. The investigation of composite materials focuses on the fiber-reinforced polymer composite materials. The main composition of such composite materials includes the reinforcement fibers and the matrix. Commonly used reinforcement fibers for marine applications include glass fiber, aramid fiber and carbon fiber. The investigation of these three reinforcement fibers demonstrates their mechanical properties, strength and other reference data. Matrices suitable for marine applications are also investigated. The main types of composite materials used for structural components in marine applications are laminated composite materials as well as sandwich-structured composite materials. Sandwich composites are the preferred choice of the hull material, which provides sufficient stiffness as well as strength, and the core material can provide excellent buoyancy.

In order to solve the problem of wave impacting on a structure and the associated wave load computation problem, the numerical simulation is a cost-effective and efficient approach. Wave impact on structure is a fluid-structure interaction problem, and its numerical simulation can be realized through the establishment of a numerical wave flume. The numerical wave flume can be used to generate target waves and to study the interaction between waves and the target structure coupled in the model, including the calculation of wave loads along the fluid-structure interface and the dynamic responses of the structure subjected to wave impacts. A method commonly used for the numerical simulation of FSI problem is the Arbitrary Lagrangian Eulerian method. Effectiveness of the ALE method has been verified by existing research on related FSI problems, such as bird impact, sloshing tanks, underwater explosion, and so on. The ALE method allows the presence of multi-materials, fluid elements and solid elements, to be in the model at the same time, and it enables scenarios with large material deformations as well as the tracking of interfaces between different materials. The free surface resolution ability of the ALE method in FSI problems proves the reliability of this approach for the wave generation. The computation of wave loads can then rely on a contact algorithm based on the penalty method.

In summary, the objectives of this study is to conduct wave impact investigations on the wave glider's float structure using a numerical wave flume. This first involves the generation of water waves. While the target wave conditions are primarily selected to correspond to the general operating wave conditions for the wave glider, specifically sea states $2-4$. The wave absorption method must be applied to reduce the impact of reflected waves. For wave impacts, the fluid domain and the float structure must be coupled within the same model. Wave impact loads must be calculated. Moreover, the simulation results should allow the visualization of wave-structure's interface evolution and the dynamic motion of the structure.

Chapter 2

Wave Theories and Wave Generation

2.1 Linear Wave Theory

The phenomena of water waves can be understood as unsteady free surface flow as subjected to gravitational force. Wave phenomena and the ways in which waves are generated are diverse, different types of waves can be observed on the ocean surface. For example, waves can be distinguished by the duration of their period. In this way, wave phenomena include wind-induced waves (with periods less than 25 s, second), storm-induced wave $-$ the swells, seiche phenomena induced by the resonance of long period wave components, tsunami phenomena with periods of up to one hour, and tide phenomena with periods of half a day to one day induced by the gravitational pull of the sun and the moon [69]. On the other hand, from a physical point of view, water waves can be categorized into two types, the oscillatory waves and the translatory waves. In those two cases, the average transport (the discharge or mass transport) of fluid in oscillatory waves is zero, whereas the translatory waves involve the transport of fluid along the wave propagation direction[70].

The wave scenarios experienced by the wave glider in normal working conditions are mainly considered here as waves below sea state 4. This type of water waves can be regarded as wind-induced waves, which have short periods, high frequencies, and can be classified as oscillatory waves. The Airy wave theory is a fundamental and commonly used theory for describing water waves, developed by Airy in 1845 [71]. The Airy wave theory, also known as the small amplitude wave theory or linear wave theory, it applies to wind-induced water waves. And for some special water wave phenomena, they can be described by higher-order water wave theories, which are usually called finite amplitude wave theories, and they can be used to describe nonlinear regular water waves.

The Airy wave theory adopts a hypothesis that, for the studied water waves, the ratio of the wave height (or amplitude) to the wavelength is a minor amount, and as such, there is very little free surface motions. The small amplitude assumption enables the nonlinear terms in the free surface boundary conditions to be neglected, so that the equations can be linearized. This linearized wave theory describes simplified water waves in a mathematical form of 2D, sinusoidal waves. The motions of water particles are periodically closed circular or elliptical orbits, so, there is no mass transport. And these waves can be defined by given parameters such as water depth, wave height, wavelength, period, and so on. Figure 2.1 below shows the linear wave with basic wave parameters and the water particle trajectories in deep-water condition.

The linear wave takes the form of a sinusoidal function and propagates along the x direction with the water depth being d. Taking the still water level as a reference, the water wave consists of the crests and troughs. The vertical distance between the crest and the adjacent trough is the wave height H, the wave amplitude a is half of the wave height, and the horizontal distance between adjacent crests or troughs is the wavelength L. The trajectory of water particles under deep-water conditions is a closed circle.

Other commonly used parameters in the description of water waves include wave period T, wave frequency f (equals $2\pi/T$), phase velocity of the wave c

(equals L/T), wave number k (equals $2\pi/L$), wave steepness H/L, and relative water depth d/L.

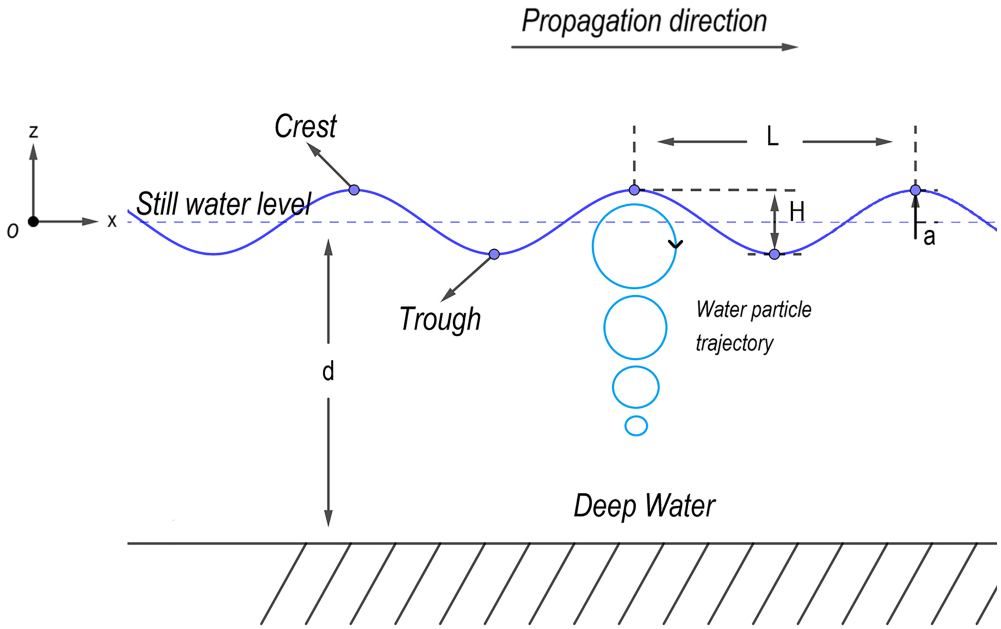


Figure 2.1: Linear Wave Schema

In order to establish the linear water wave problem, the following assumptions are adopted. First, the water wave is a 2D problem which states that the water wave propagates along the x direction in the xOz plane. Next, the Coriolis force caused by the rotation of the Earth can be ignored, and the pressure on the free surface is uniformly distributed and constant, as the water wave is only affected by the gravitational force. Then, the fluid (seawater) is considered to be uniform and incompressible, so that the density of the fluid, ρ, is a constant. Also, the effect of viscosity on the flow field is considered to be negligible compared to the inertia, and the fluid is irrotational. These two assumptions about the fluid make it possible to determine the governing equation of the fluid, which is the Laplace's equation.

Taking the origin O which is located at the still water level as a reference, at any point of the fluid, the fluid velocity vector can be written as $\boldsymbol{u}(u, w)$ with re-

spectively u and w the components in x-direction and z-direction. The principle of mass conservation gives the continuity equation of the fluid as follows,

$$\frac{\partial \rho}{\partial t} + \nabla \cdot (\rho \boldsymbol{u}) = 0, \tag{2.1}$$

where t represents time, ∇ is the Nabla operator.

Then, by introducing the material derivative in equation (Eq.) 2.1 as follows,

$$\frac{D}{Dt} \equiv \frac{\partial}{\partial t} + \boldsymbol{u} \cdot \nabla, \tag{2.2}$$

and for the incompressible fluids,

$$\frac{D\rho}{Dt} = 0, \tag{2.3}$$

the following equation can be obtained,

$$\nabla \cdot \boldsymbol{u} = \frac{\partial u}{\partial x} + \frac{\partial w}{\partial z} = 0. \tag{2.4}$$

Since the fluid is considered to be irrotational and this assumption is consistent with the description of fluids in the potential flow theory, the fluid velocity field in the potential flow theory can be introduced. First for an irrotational fluid, the vorticity field $\boldsymbol{\omega}$ equals 0, as follows,

$$\boldsymbol{\omega} \equiv \nabla \wedge \boldsymbol{u} = 0, \tag{2.5}$$

with the introduction of the velocity potential $\boldsymbol{\phi}(x, z, t)$, the velocity field can be expressed as the gradient of the velocity potential, as follows,

$$\boldsymbol{u} = \nabla \phi, \tag{2.6}$$

therefore, for an incompressible and irrotational fluid which satisfies Eq. 2.4 and

Eq. 2.6, the velocity potential also satisfies the Laplace's equation as follows,

$$\nabla^2\phi = \frac{\partial^2\phi}{\partial x^2} + \frac{\partial\phi^2}{\partial z^2} = 0. \tag{2.7}$$

To complete the description of the water wave problem, the boundary conditions for the water waves should also be established. These boundary conditions include the lateral boundary condition, the bottom boundary condition, and the free surface boundary conditions in the 2D water wave problem.

The lateral boundary condition describes the periodic inflow water wave on the left border, as follows,

$$\phi(x, z, t) = \phi(x - ct, z). \tag{2.8}$$

Regarding the bottom boundary condition, the bottom material is usually considered to be impermeable in the water wave problem. In other words, water particles located at the bottom of the water cannot penetrate the bottom boundary. For this condition, consider an object $\mathbf{\Gamma}$, whose surface is an impermeable boundary, and the expression for the object's surface is $\Gamma(x, y, z, t) = 0$. Since the fluid cannot penetrate the surface of the object $\mathbf{\Gamma}$, the variation of fluid particles on the object's surface with respect to time would be zero. Therefore, the material derivative of Γ equals zero, and can be expressed as follows,

$$\frac{D\Gamma}{Dt} = \frac{\partial\Gamma}{\partial t} + (\nabla\phi \cdot \nabla)\Gamma = 0. \tag{2.9}$$

For the bottom boundary located at $z = -d$, the bottom can be written in the form of a function which is $z = -d$. Then the surface expression of the bottom can be written as $B(x, z, t) = z + d = 0$. The material derivative of B can be expressed as follows,

$$\frac{DB}{Dt} = \frac{\partial B}{\partial t} + (\nabla\phi \cdot \nabla)B = \frac{\partial\phi}{\partial z} = 0, \tag{2.10}$$

therefore, for the bottom boundary condition of the water wave problem, the equation as follows should be satisfied,

$$\frac{\partial \phi}{\partial z} = 0 \text{ on } z = -d, \tag{2.11}$$

where z represents vertical distance.

As for the free surface boundary conditions, the kinematic free surface boundary condition and the dynamic free surface boundary condition need to be satisfied. The former assumes that the moving surface which is composed of fluid particles should also be considered as a special kind of impermeable boundary. Thus, the water particles located at the free surface of the water should always remain at corresponding positions of the free surface and cannot penetrate the free surface all along the propagation of the water wave. In the same way, the free surface can be written in the form of a function which is $z = \eta(x, t)$, and the surface expression for the free surface can be written as $F(x, z, t) = z - \eta(x, t) = 0$. The material derivative of F can be expressed as follows,

$$\frac{DF}{Dt} = \frac{\partial F}{\partial t} + (\nabla \phi \cdot \nabla) F = 0, \tag{2.12}$$

next, it can be written as,

$$\frac{\partial (z - \eta)}{\partial t} + \left(\frac{\partial \phi}{\partial x}, \frac{\partial \phi}{\partial z} \right) \cdot \left(\frac{\partial (z - \eta)}{\partial x}, \frac{\partial (z - \eta)}{\partial z} \right) = 0, \tag{2.13}$$

then the condition as follows needs to be satisfied for the kinematic free surface boundary condition,

$$\frac{\partial \phi}{\partial z} = \frac{\partial \eta}{\partial t} + \frac{\partial \eta}{\partial x} \frac{\partial \phi}{\partial x} \text{ on } z = \eta, \tag{2.14}$$

where η represents the free surface elevations of the water wave from still water level.

The dynamic free surface boundary condition describes that, since the fluid is non-viscous, the surface tension of the water is neglected and the pressure

near the free surface is equal to atmospheric pressure exerted on the water surface, and the pressure along the free surface should be uniformly distributed. First of all, the water wave problem considered as an ideal fluid needs to satisfy the Euler's equation which is expressed as follows,

$$\frac{\partial \boldsymbol{u}}{\partial t} + \boldsymbol{u} \cdot \nabla \boldsymbol{u} = -\frac{1}{\rho} \nabla p + \boldsymbol{f}, \tag{2.15}$$

where p represents the pressure which is the short-range local force to the fluid, and $\boldsymbol{f}$ represents the body force exerted on the fluid including all water particles. And for the term $\boldsymbol{u} \cdot \nabla \boldsymbol{u}$, it can be written as follows by introducing the identity,

$$\boldsymbol{u} \cdot \nabla \boldsymbol{u} = \nabla \left(\frac{1}{2} \boldsymbol{u} \cdot \boldsymbol{u} \right) - \boldsymbol{u} \wedge (\nabla \wedge \boldsymbol{u}), \tag{2.16}$$

where $\nabla \wedge \boldsymbol{u}$ is the vorticity $\boldsymbol{\omega}$ defined above. Then, since the fluid is incompressible, the fluid density ρ is constant. And the body force is usually considered as the gravity force, the body force can thus be represented by a potential function $\boldsymbol{\Omega}$, with $\boldsymbol{f} = -\nabla \boldsymbol{\Omega}$. So, the right side part of the equal sign of Eq. 2.15 can be written as $-\nabla(\frac{p}{\rho} + \boldsymbol{\Omega})$. The Euler's equation can be rewritten as follows.

$$\frac{\partial \boldsymbol{u}}{\partial t} + \nabla \left(\frac{1}{2} \boldsymbol{u} \cdot \boldsymbol{u} + \frac{p}{\rho} + \boldsymbol{\Omega} \right) = \boldsymbol{u} \wedge \boldsymbol{\omega}. \tag{2.17}$$

As the fluid is considered to be irrotational, the vorticity $\boldsymbol{\omega}$ of the fluid is negligible. The equation as follows can be obtained,

$$\nabla \left(\frac{\partial \phi}{\partial t} + \frac{1}{2} \boldsymbol{u} \cdot \boldsymbol{u} + \frac{p}{\rho} + \boldsymbol{\Omega} \right) = 0, \tag{2.18}$$

this means,

$$\frac{\partial \phi}{\partial t} + \frac{1}{2} \boldsymbol{u} \cdot \boldsymbol{u} + \frac{p}{\rho} + \boldsymbol{\Omega} = constant. \tag{2.19}$$

Since the body force is considered as the gravity force, the potential func-

tion $\mathbf{\Omega}$ can be expressed as follows,

$$\mathbf{\Omega} = gz, \tag{2.20}$$

where g stands for the gravitational acceleration.

In the water wave problem, waves are considered to become stationary as it propagates to a distance of infinity. So at infinity, the stationary water surface gives $z = 0$, with the pressure being the atmospheric pressure p_a, therefore, $p = p_a$. These two conditions allow the constant in Eq. 2.19 to be obtained, as follows,

$$constant = \frac{p_a}{\rho}. \tag{2.21}$$

Finally, the equation of motion of the fluid in the water wave problem can be obtained as follows,

$$\frac{\partial \phi}{\partial t} + \frac{1}{2}\boldsymbol{u} \cdot \boldsymbol{u} + \frac{p - p_a}{\rho} + gz = 0 \text{ on } z \leq \eta. \tag{2.22}$$

More precisely, on the free surface, the pressure equals atmospheric pressure p_a on the surface $z = \eta$. Then, the dynamic free surface boundary condition in the water wave problem can be expressed as follows,

$$\frac{\partial \phi}{\partial t} + \frac{1}{2}\left[\left(\frac{\partial \phi}{\partial x}\right)^2 + \left(\frac{\partial \phi}{\partial z}\right)^2\right] + g\eta = 0 \text{ on } z = \eta. \tag{2.23}$$

Above Eq. 2.7, Eq. 2.8, Eq. 2.11, Eq. 2.14, and Eq. 2.23 constitute the governing equation and boundary conditions used to describe the 2D water wave problem. Solving these equations is difficult. Because the kinematic free surface boundary condition Eq. 2.14 and the dynamic free surface boundary condition Eq. 2.23 are nonlinear. Also, these two equations should be satisfied on the free surface which is unknown.

These problems can be linearized with the help of the assumption made by the Airy wave theory, that is, the ratio of the wave amplitude to the wavelength

is a small quantity, expressed as follows,

$$\frac{a}{L} \ll 1. \tag{2.24}$$

This condition admits the linearization of Eq. 2.14, Eq. 2.23, and it indicates that the variation of the free surface η is considered to be small. Then, the kinematic free surface boundary condition and the dynamic free surface boundary condition can be satisfied on the still water level $z = 0$.

The small variation of the free surface can lead to the consideration that the velocity of water particles of the water wave is small. Thus, the kinematic free surface boundary condition Eq. 2.14 can be linearized as follows,

$$\frac{\partial \phi}{\partial z} = \frac{\partial \eta}{\partial t} \text{ on } z = 0. \tag{2.25}$$

The dynamic free surface boundary condition Eq. 2.23 can be linearized as follows,

$$\frac{\partial \phi}{\partial t} + g\eta = 0 \text{ on } z = 0, \tag{2.26}$$

and the expression of the free surface η can be obtained as follows,

$$\eta = -\frac{1}{g}\frac{\partial \phi}{\partial t}. \tag{2.27}$$

By combining Eq. 2.27 and the linearized kinematic free surface boundary condition Eq. 2.25, the free surface boundary condition under the linear wave theory can be obtained as follows,

$$g\frac{\partial \phi}{\partial z} + \frac{\partial^2 \phi}{\partial t^2} = 0. \tag{2.28}$$

Then, above Eq. 2.7, Eq. 2.11, and Eq. 2.28 constitute the governing equation and boundary conditions used to describe the 2D linear water wave problem. The Figure 2.2 shows the governing equation and the boundary con-

ditions for the linear water wave problem.

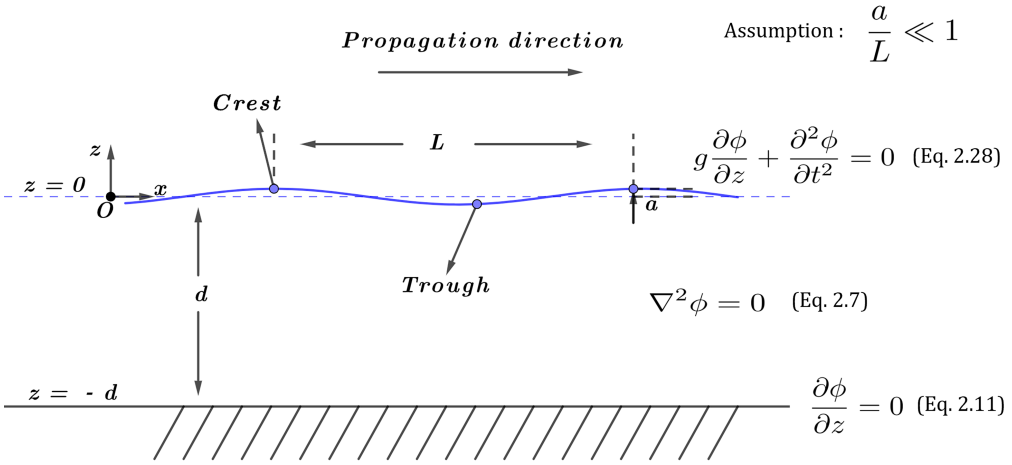


Figure 2.2: Governing Equation and Boundary Conditions of Linear Wave

From these three equations which characterize the linear water wave, the expression of the velocity potential ϕ of the linear wave can be solved by separation of variables. The expression as follows can be given,

$$\phi = \frac{gA}{\alpha} \sin(ix - \alpha t) \frac{\cosh i(z+d)}{\cosh id}, \tag{2.29}$$

where A, α and i are the proposed constant for the expression.

Next, the assumption that the water depth approaches infinity needs to be made, that means, d is a large quantity compared to others. Thus, the expression can be further expressed as follows,

$$\phi = \frac{gA}{\alpha} \sin(ix - \alpha t) e^{iz}, \tag{2.30}$$

where e is the mathematical constant of exponential function.

Then, by combining the expression of the velocity potential ϕ (Eq. 2.30) with that of the free surface of the linear water wave η (Eq. 2.27), the expression of the free surface can be solved, which is expressed as follows,

$$\eta = A \cos(ix - \alpha t). \tag{2.31}$$

In fact, by cross-referencing the water wave parameters, it can be concluded that the constant A is equivalent to the wave amplitude a, that the constant i is equivalent to the wave number k, and that the constant α is equivalent to the cyclic frequency which equals $\frac{2\pi}{T}$. Eventually, the wave profile of the linear water wave is of sinusoidal form.

2.2 Wave Generation

In order to study the water wave phenomena and its associated FSI problems, the generation of accurate target wave profiles is an indispensable step. The construction of a wave flume, or wave tank, is a common way to generate water waves. And waves are generated through disturbances caused by the mechanical movement of the paddles mounted at the boundary. This method of water wave generation can be traced back to Havelock's research in 1929, in which forced surface waves were generated by small oscillations of a solid body [72]. Based on this approach, different types of wavemakers as well as different installation conditions were further investigated for the generation of different water waves. The theory of water wave generation using piston-type, flap-type, and some variant types of wavemakers was described and analyzed by Biésel and Suquet in their 1951 and subsequent studies [73, 74]. Their study characterized the solution of a wave flume's wavemaker that generates linear water waves. The Biésel transfer function is introduced to describe the relation between the wavemaker's stroke and the amplitude of generated waves. Physical wave flumes and wave tanks have been developed to be able to handle the generation of nonlinear water waves as well as irregular waves.

Usually, the generation of linear and nonlinear water waves can be realized through a wave flume. Common wavemakers for a wave flume include the piston-type and the flap-type, and it has been mentioned previously that these two types of wavemakers can be respectively applied to the generation of wa-

ter waves under different water depth conditions. Generating water waves by means of a wave flume is sufficient to install a wavemaker on one side of the flume for creating mechanical disturbances. The piston-type wave flume generates disturbances through the reciprocating horizontal motion of the wavemaker. The Figure 2.3 illustrates a schematic diagram of the generation of water waves by a typical piston-type wavemaker, and the wavemaker is a paddle.

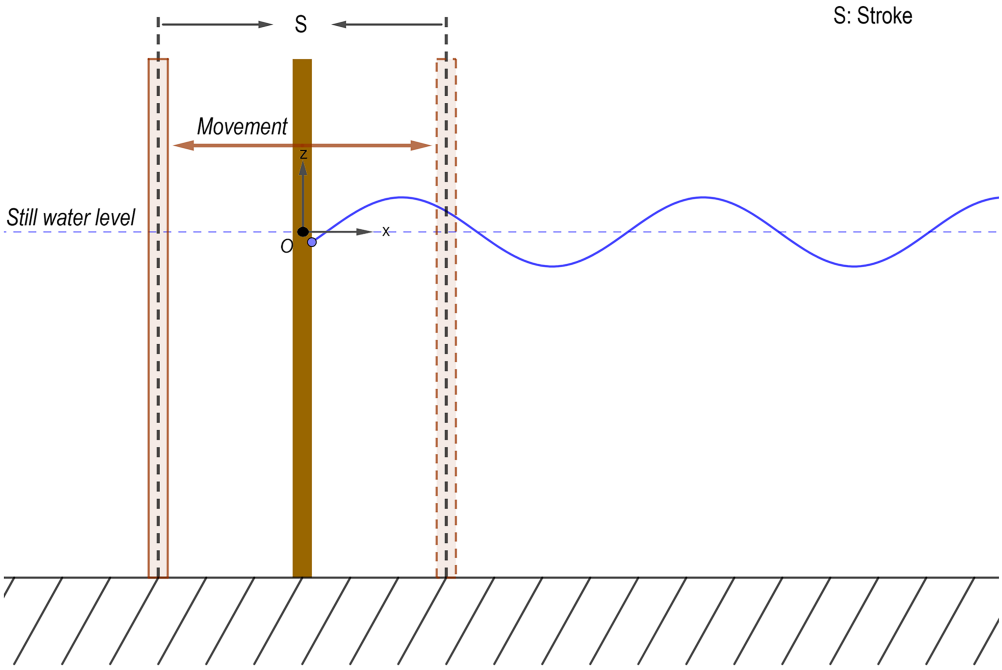


Figure 2.3: Piston-Type Wavemaker

Sarmento validated the oscillating surface pressure theory for the wave energy absorption of oscillating water column devices under linear water waves through a piston-type experimental wave flume [75]. Izquierdo *et al.* validated their CFD wave flume model through a piston-type narrow wave flume, their study mainly focused on the generation and the propagation of different monochromatic regular waves in a large range of wave parameter combinations [76]. Wu *et al.* generated solitary waves through a piston-type wave flume, the stability of generated waves was observed and the previously proposed solitary wave generation method was verified [77]. Schimmels *et al.* described the ex-

periment using a piston-type wavemaker to generate tsunami-like waves in a large-scale wave flume [78]. Lee *et al.* studied the breaking wave phenomena using a piston-type wave flume and compared the results with the corresponding numerical simulations [79]. Nouioui and Dogan presented the design and execution of a piston-type wave flume that can be used to generate both regular and irregular waves, and the generation of irregular waves was verified by corresponding numerical wave flume models [80].

The flap-type wave flume is basically as same as the piston-type wave flume, with the difference being that the wavemaker used to produce fluid disturbances performs a reciprocating rotational motion at a certain angle. The Figure 2.4 illustrates a schematic diagram of the generation of water waves by a typical flap-type wavemaker, using a paddle wavemaker.

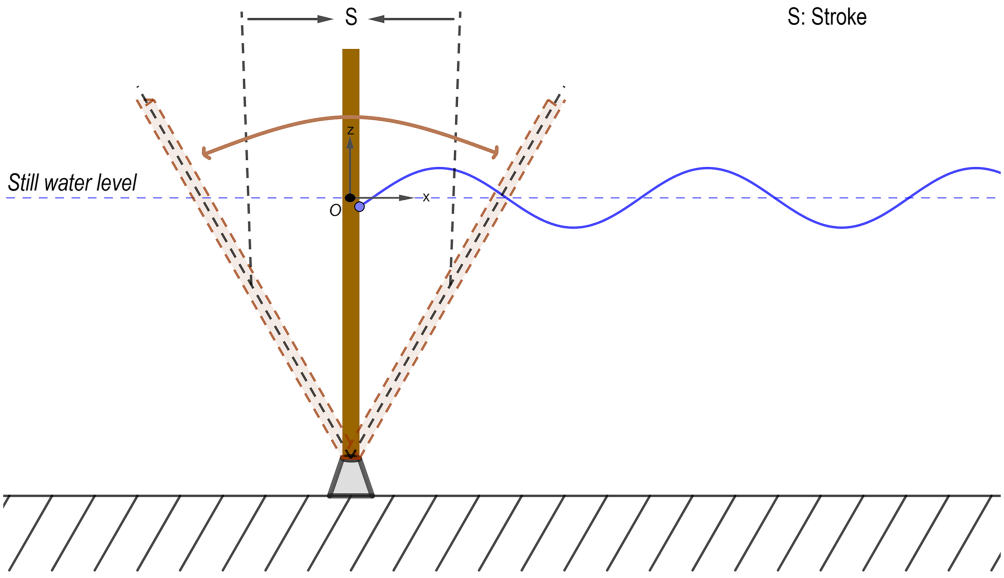


Figure 2.4: Flap-Type Wavemaker

Spinneken and Swan validated the experimental generation of regular waves in a flap-type wave flume based on the second-order wavemaker theory using force-feedback control [81]. Khalilabadi and Bidokhti presented the design, construction, and testing of a small-scale flap-type wave flume device that can be used to generate both regular and irregular waves [82]. Lal and Elango-

van constructed and validated a flap-type wavemaker model that can be used to simulate the generation of regular waves in experimental wave flume [83]. Shehab *et al.* established a flap-type numerical water tank that can generate regular and irregular waves, and the model was verified with theoretical solutions and published experimental data [84]. Saincher and Banerjeea described the design and development of a flap-type wave flume and its corresponding numerical model for studying the hydrodynamics of breaking waves [85]. Dao *et al.* established a flap-type numerical wave flume, in which regular waves and focused waves were generated and then experimentally verified [86].

In addition to the two types of wavemakers mentioned above, there is another type of wave tank used to generate irregular wave surfaces. Such a wave tank is generally a circular area with a combined array of piston-type or flap-type wavemakers mounted in parallel at the boundary, which is often referred to as a snake-type wavemaker. These wavemakers can each produce different disturbances to generate a region of irregular water waves to simulate real ocean wave conditions which are random. Nurdin *et al.* studied the propagation of waves generated by a snake-type wavemaker based on linear wave theory [87]. Park *et al.* generated fully nonlinear multi-directional waves using a snake-type viscous three-dimensional numerical wave tank model, and the hydrodynamic forces acting on an advancing ship under such wave conditions were also studied [88].

The construction of a large-scale physical wave flume requires an expensive investment. Consequently, the construction of a corresponding numerical wave flume model is an economical and efficient solution. Physical experiments of water wave generation can basically be reproduced by numerical simulations. The numerical wave flume model makes reference from the physical flume device, and the generation of water waves is also achieved through the wavemaker (solid body) which creates disturbances in the two-phase fluid region (air-water). The numerical wave flume model is capable of simulating complex physical wave flume devices and it is equally capable of generating both regular

and irregular waves. Meanwhile, the numerical wave flume model can be validated through the theoretical solutions of the target waves or by experimental wave flume data.

In numerical water wave simulations, the disturbances produced by the wavemaker's motion are the key factor for the accuracy of the target wave profiles. It is necessary to derive the expression of the wavemaker's movement according to the corresponding wavemaker theory and the wave theory used for target waves. Then, it is required to execute the exact wavemaker movements in the numerical simulation.

2.2.1 Piston-Type Wavemaker Theory

Wavemaker theory views the generation of water waves as the result of free surface disturbances due to the wavemaker's motion. On the basis of the mathematical description of linear water wave problem in the previous section, the wavemaker can now be integrated into the water wave problem forming the mathematical description of the water wave generation problem. Instead, the periodic inflow of water waves described by the lateral boundary condition in the water wave problem can be replaced by the movement expression of the wavemaker. The purpose of this discussion of wavemaker theory is to explore how to generate accurate target waves in a wave flume. Therefore, the relationship between the main characteristic parameters of generated water waves and the wavemaker's movement needs to be clarified.

In order to form the description of water wave generation problem, it is as well necessary to construct the related boundary conditions. And for a wave flume actuated by a piston-type wavemaker, the horizontal displacement of the wavemaker will constitute a kinematic boundary condition of the lateral boundary. As shown in Figure 2.3, the wavemaker is a rectangular paddle. Taking the intersection point of the paddle and the still water level as the origin O to set up the coordinate system, the horizontal rightward direction is the x direction, and

the vertical upward direction is the z direction. Then, the stroke of the paddle can be expressed as $S(z)$. And the horizontal displacement of this piston-type wavemaker can be described as follows,

$$x = \frac{S(z)}{2}\sin(\theta t), \tag{2.32}$$

where θ is the frequency of the paddle's motion, and $\theta = 2\pi/T$ with T representing the period of paddle's motion.

As for the paddle, its surface is in contact with the water particles, so it must also be considered as an impermeable boundary and the kinematic boundary condition needs to be satisfied on its surface. As in the previous section, the expression of the paddle's surface can be similarly expressed by a function $P(x, z, t)$, as follows,

$$P(x, z, t) = x - \frac{S(z)}{2}\sin(\theta t) = 0. \tag{2.33}$$

Then, the material derivative of the paddle's surface $P(x, z, t)$ can be expressed as follows,

$$\frac{DP}{Dt} = \frac{\partial P}{\partial t} + (\nabla\phi \cdot \nabla)P = 0, \tag{2.34}$$

and the following equation can be obtained,

$$\frac{\partial \phi}{\partial x} - \frac{1}{2}\frac{\partial \phi}{\partial z}\sin(\theta t) = \frac{S(z)}{2}\theta\cos(\theta t) \text{ on } P(x, z, t) = 0. \tag{2.35}$$

Given that the target water waves are in the realm of linear wave theory, it is possible to transition from the assumption of small amplitude of water waves to the assumption of a small displacement of the wavemaker. This allows that the second term on the left side of the Eq. 2.35 can be neglected and thus linearized, as follows,

$$\frac{\partial \phi}{\partial x} = \frac{S(z)}{2}\theta\cos(\theta t) \text{ on } P(x, z, t) = 0. \tag{2.36}$$

Above boundary condition for the wavemaker should be satisfied during its movement. It is much more convenient to select the kinematic condition of the paddle when it is in its main position ($x = 0$) in order to further simplify the description of the water wave generation problem. This can be obtained by expanding Eq. 2.36 into a Taylor series equation, whose first two terms can be expressed as follows,

$$\begin{aligned}\left[\frac{\partial\phi}{\partial x} - \frac{S(z)}{2}\theta\cos(\theta t)\right]_{x=\frac{S(z)}{2}\sin(\theta t)} &= \left[\frac{\partial\phi}{\partial x} - \frac{S(z)}{2}\theta\cos(\theta t)\right]_{x=0} \\ &+ \frac{S(z)}{2}\sin(\theta t)\frac{\partial}{\partial x}\left[\frac{\partial\phi}{\partial x} - \frac{S(z)}{2}\theta\cos(\theta t)\right]_{x=0} \\ &+ \ldots .\end{aligned} \tag{2.37}$$

In the same way, based on the assumption that the wavemaker's motion is small, the second term, as well as the following terms, will be considered as small quantities and be neglected. The first term will then be the lateral kinematic boundary condition for linear water wave generation using a piston-type wavemaker, expressed as follows,

$$\frac{\partial\phi}{\partial x} = \frac{S(z)}{2}\theta\cos(\theta t) \text{ on } P(x,z,t) = 0, \text{ at } x = 0. \tag{2.38}$$

The Eq. 2.7, Eq. 2.11, Eq. 2.28, Eq. 2.38 constitute respectively the governing equation, the bottom boundary condition, the free surface boundary condition, and the lateral boundary condition as the mathematical description of linear water wave generation problem by a piston-type wavemaker. And in fact, there is another lateral boundary condition used to describe water waves propagating into the distance. The propagating waves need to maintain a constant wave profile, as described by the radiation boundary condition. Thus, the lateral boundary condition for far-field water waves can be expressed as follows,

$$\frac{d\phi}{dt} = 0. \tag{2.39}$$

The Eq. 2.39 along with the other four equations complete the description. And the Figure 2.5 shows the governing equation and boundary conditions for the piston-type wavemaker problem.

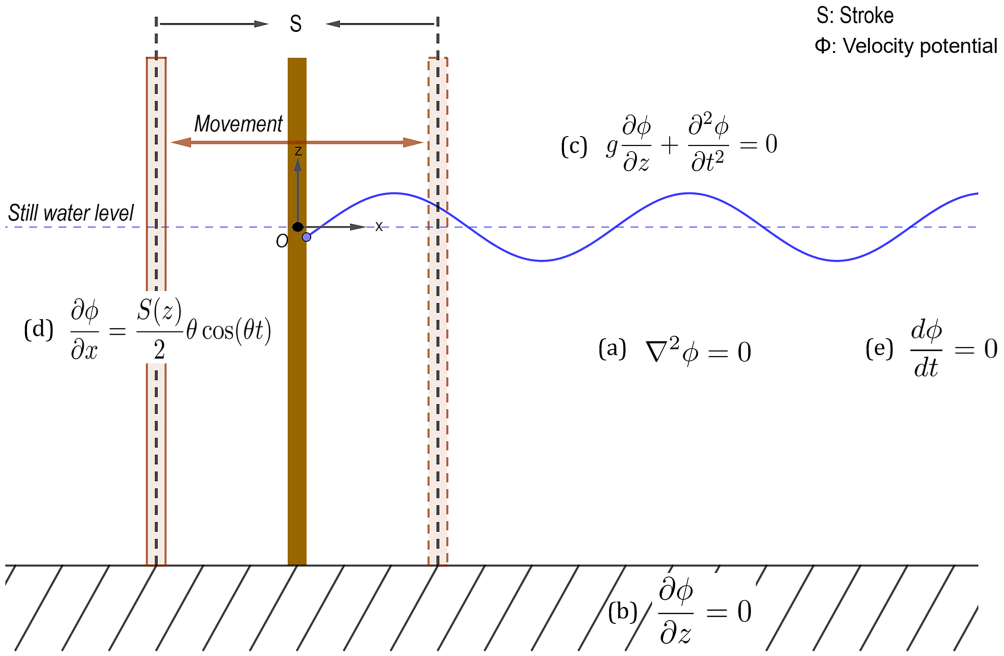


Figure 2.5: Governing Equation and Boundary Conditions of Piston-Type Wave Generation

This water wave generation problem provides a governing equation that needs to be satisfied by the velocity potential, as well as four boundary conditions. It is desirable to find a solution to the velocity potential that satisfies the boundary conditions centered on the governing equation, and to explore therein the relationship between the characteristic parameter that determines the generated wave, the wave height H, and the wavemaker's kinematic parameter, the stroke S.

To do so, a general solution satisfying the Laplace's equation Eq. 2.7 and the boundary conditions Eq. 2.11, Eq. 2.28 Eq. 2.38 can be first found. In this step, the boundary condition Eq. 2.38 is for the moment considered as a

simplified case, expressed as follows,

$$\frac{\partial \phi}{\partial x} = 0 \text{ on } P(x, z, t) = 0. \tag{2.40}$$

Thus, the homogeneous solution that satisfies the conditions can be expressed by a linear combination of functions as follows,

$$\phi_H(x, z, t) = A_H \cdot \cos(k_i x) \cdot \cosh(k_i(z + d)) \cdot \cos(\theta_i t - a_0), \tag{2.41}$$

where A_H and a_0 are arbitrary constants, and k_i represents the solution to the dispersion relation expressed as follows,

$$\theta_i^2 = k_i \cdot g \cdot \tanh(k_i d). \tag{2.42}$$

Next, the particular solution satisfying the Laplace's equation Eq. 2.7 and the boundary conditions Eq. 2.11, Eq. 2.28 Eq. 2.38 should be obtained. And the particular solution can be expressed as follows,

$$\begin{aligned}
&\phi_P(x, z, t) = \left(\sum_{n=0}^{\infty} B_n \phi_n \right) \cos(\theta t) \\
&\text{with} \\
&\phi_0 = \frac{\theta}{k_0} \cosh(k_0(z + d)) \cdot \sin(k_0 x) \\
&B_0 = 2 \cdot k_0 \frac{\int_{-d}^{0} e(z) \cdot \cosh(k_0(z + d)) \cdot dz}{\sinh(k_0 d) \cdot \cosh(k_0 d) + k_0 d} \\
&\phi_n = -\frac{\theta}{k_n} \cos(k_n(z + d)) \cdot e^{-k_n x} \ , \ n > 0 \\
&B_n = 2 \cdot k_n \frac{\int_{-d}^{0} e(z) \cdot \cos(k_n(z + d)) \cdot dz}{\sin(k_n d) \cdot \cos(k_n d) + k_n d} \ , \ n > 0 \ ,
\end{aligned} \tag{2.43}$$

where $e(z)$ is the general expression of the wavemaker's displacement, ex-

pressed as follows,

$$e(z,t) = \frac{S(z)}{2}\sin(\theta t), \tag{2.44}$$

and k_0 represents the solution to the dispersion relation expressed as follows,

$$\theta^2 = k_0 \cdot g \cdot \tanh(k_0 d), \tag{2.45}$$

then, the $k_1 ...$ to k_n are the first and subsequent positive solutions to the equation expressed as follows,

$$\theta^2 = -k_n \cdot g \cdot \tan(k_n d). \tag{2.46}$$

Eventually, the final solution also satisfying the boundary condition Eq. 2.39 can be determined. The velocity potential ϕ which satisfies Laplace's equation and all four boundary conditions can be composed of $\phi = \phi_H + \phi_P$, and the expression can be written as follows,

$$\begin{aligned}\phi(x,z,t) = &-\frac{\theta}{k} \cdot B_0 \cdot \cosh(k(z+d)) \cdot \sin(\theta t - kx) \\ &- \sum_{n=1}^{\infty} B_n \cdot \frac{\theta}{k_n} \cdot \cos(k_n(z+d)) \cdot e^{-k_n x} \cdot \cos(\theta t).\end{aligned} \tag{2.47}$$

Once the expression of the velocity potential is obtained, the final expression of the free surface η can also be obtained through Eq. 2.27, expressed as follows,

$$\begin{aligned}\eta(x,t) = &B_0 \cdot \sinh(kd) \cdot \cos(\theta t - kx) \\ &+ \sum_{n=1}^{\infty} B_n \cdot \sin(k_n d) \cdot e^{-k_n x} \cdot \sin(\theta t).\end{aligned} \tag{2.48}$$

It should be noted that the two terms of above equation Eq. 2.48 each describe a different stage of the generated water waves. The first term, known as the far-field solution, is often employed to determine the free surface of generated water waves. It describes the steady progressive waves generated by

the wavemaker, that is, the target water wave profile. And the second term describes standing waves that travel away from the wavemaker as they propagate, and these waves gradually decay with distance. Thus, the system of equations which determines the relationship between the piston-type wavemaker and the generated linear water waves can be expressed as follows,

$$\begin{cases} \eta(x,t) = B_0 \cdot \sinh(kd) \cdot \cos(\theta t - kx), \\ B_0 = 2 \cdot k_0 \frac{\int_{-d}^{0} e(z) \cdot \cosh(k_0(z+d)) \cdot dz}{\sinh(k_0 d) \cdot \cosh(k_0 d) + k_0 d}, \\ e(z,t) = \frac{S(z)}{2} \sin(\theta t). \end{cases} \tag{2.49}$$

For the stroke of the piston-type wavemaker S, it can be expressed as $S(z) = S_0$. And the expression of the free surface η determines the wave height H of generated target water waves. Thus, the Biésel transfer function can be obtained and expressed as follows,

$$\frac{H}{S_0} = \frac{2\sinh^2(kd)}{\sinh(kd)\cosh(kd) + kd}. \tag{2.50}$$

In some other studies, the equivalent equation of above equation Eq. 2.50 was obtained [52, 89]. The equivalent equation can be written as follows,

$$\frac{H}{S_0} = \frac{2(\cosh(2kd) - 1)}{\sinh(2kd) + 2kd}. \tag{2.51}$$

The Biésel transfer function is an essential tool to characterize the accuracy and rationality of water waves generated by the wave flume being constructed.

2.2.2 Wave Flume and Wave Characteristics

Whether for physical wave flume experiments or numerical wave flume simulations, dimensions of the wave flume are determined, which defines the limit of water waves that it can generate. So, it is important to verify that the characteristics of generated water waves are consistent with applied wave theory as

well as with actual situation of the target water waves. In reference to the description of the applicability of water wave theories in literature studies, for the linear wave theory, its main application range is to water waves in deep water and intermediate water depth conditions [90, 91]. In some studies, linear wave theory can also be applied to a limited range of water wave phenomena in shallow water depth conditions [92–94]. As for the piston-type wavemaker, it has been mentioned that this type of wavemaker is more suitable for water waves under intermediate and shallow water depth conditions.

In the characterization of water waves, three characteristic parameters are often used, that are, the wave height H, the wavelength L, and the water depth d. And from these three parameters, three characteristic ratios can be obtained, respectively, the wave steepness H/L, the relative wave height H/d, and the relative wave depth d/L. The wave steepness can be used to distinguish between linear and nonlinear water waves. And the relative water depth can be used to characterize environmental water depth conditions of generated water waves. Table 2.1 shows the classification of water waves by relative water depth.

Water depth condition	Relative water depth (d/L)
Shallow water	$0 - 1/20$
Intermediate water depth	$1/20 - 1/2$
Deep water	$> 1/2$

Table 2.1: Classification of Water Waves by Relative Water Depth

When performing the design of numerical simulations of water wave generation, target waves need to meet the requirement of a reasonable wave height and also consider the constraints imposed by water depth of the wave flume on the water wave profiles. Length of the flume is also an important factor to take into account, which involves dealing with the problem of the water wave reflections, and this will be discussed in the next section.

2.3 Wave Absorption and Non-reflective Boundary

Whether it is a physical wave flume or a numerical wave flume, the reflection of water waves propagating in a bounded area is unavoidable. Reflected waves will affect the accuracy of generated target water waves, and certain means are needed to reduce their impact.

In a typical wave flume, the reflection of water waves occurs when water waves generated from one side propagate and come into contact with the boundary on the other side. Without considering energy dissipation, the amplitude and period of reflected water waves are as same as those of the incident water waves. When these two waves meet and interfere, the standing wave phenomena occur. If incident wave is the target water wave, the observed wave profile will be distorted. This is quite noticeable in a smaller sized wave flume. Therefore, building a wave flume as large as possible or with one end open is one of the options to avoid this problem. Figure 2.6 demonstrates the standing wave phenomena resulting from the incident and reflected waves.

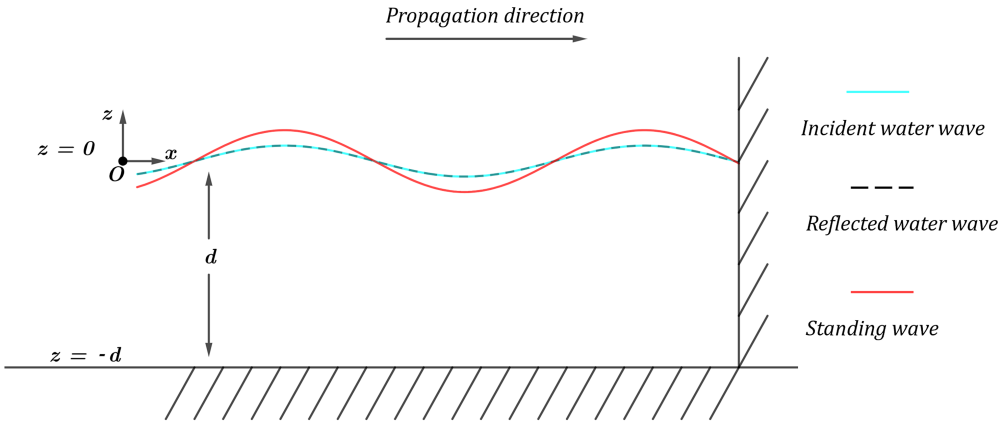


Figure 2.6: Schema of Standing Wave Phenomena

For physical water wave generation experiments, if the construction of a large-scale wave flume is unaffordable, the construction of a relaxation zone using suitable materials or a slope on the far side is also a commonly used method of wave absorption. This method is often referred to as passive wave

absorption. It is worth mentioning that the use of porous materials and the sloping beach have also been applied in numerical water wave generation. This is because large-scale numerical wave flume would likewise take up a large number of computational resources, increasing time and economic expenses.

Porous structures, such as naturally formed sandy beaches, are acting as a kind of natural wave absorber. When water waves come into contact with a porous structure, due to the permeability of the structure and the roughness of the material, seawater will rub against the bottom surface and cause turbulence. This will dissipate the energy of water waves and disrupt the wave profile. On the other hand, the surface of the beach is flat and sloped, which increases the amount of time that water waves are in contact with the porous structure and this can trigger the breaking of water waves that rush onto the beach. Breaking waves are also a form of energy dissipation in water waves, a phenomenon that is particularly common on sandy beaches. In beach areas with shallow water depths, wave heights of the water waves are amplified, and the energy of the waves' crest is transformed into forward curved-like wave turbulence energy, accompanied by foam. Therefore, the geometrically shaped beaches composed of sand are able to dissipate the energy of water waves, resulting in a lower reflection coefficient of water waves from such porous structures [95].

In studies on the suppression of water wave reflection by porous structures, the focus is usually on the role of structural geometry and different materials. Different strategies include the use of materials such as sand, gravel, stone, or wire mesh to change the roughness and permeability of the structure's surface, as well as changing the geometry of the structure's surface to increase the duration and complexity of the contact [96–99]. Saprykina *et al.* studied the local reflection of long waves from underwater slopes with different inclination angles, the results showed that the coefficient of the local reflection of waves decreases with the increase of the slope's distance from the coast (the decrease of the slope inclination) [100]. Urrego-Pabón *et al.* studied and evaluated effects of six wave absorbers of different geometries on the dissipation of water wave

energy [101]. Porosity of a porous structure is also one of the factors affecting the water wave absorption efficiency. Based on the linear water wave theory, Das and Bora considered the reflection of water waves in a vertical rectangular porous structure placed on an elevated impermeable horizontal bottom, and the behavior of the reflection coefficient with different relevant parameters such as depth and porosity was evaluated [102].

In physical wave flume experiments, active water wave absorption can also be applied. This is a method that eliminates the effects of reflected water waves by observing and measuring wave profile data and through the control of the wavemaker's restrained motion. Schäffer and Klopman studied and analyzed existing 2D systems for active absorption in wave flumes and fully 3D systems including coupling between adjacent feedback signals in the case of shallow water waves [103]. In the research of Milgram, a self-actuating wave absorbing system set up at the end of the wave flume was designed, which utilizes the perturbations generated by a moving termination for water wave absorption [104].

For numerical wave flumes, porous structures and slopes mentioned above are also applicable. However, the modeling of a passive wave absorber device with a complex geometry of materials different from the fluids embedded in a numerical model not only increases the computational complexity and time cost like extending the length of the wave flume, but also requires an advance verification of the efficiency of the absorber device which is suitable for the constructed wave flume. And the implementation of an active wave absorption system in the numerical simulation will be more complex.

In the case of numerical wave flume simulations, however, engineers of different CFD software have taken the issue of wave absorption into consideration when designing the fluid calculation environment. In certain fluid computation environments, such as the Structured Arbitrary Lagrangian Eulerian (SALE) code environment of LS-DYNA, it is possible to set a "Non-reflective boundary condition" for water waves directly on the boundaries. But the computational

environments of most CFD software do not provide this direct function. In more cases, creating a damping zone or a relaxation zone is the preferred choice. Anbarsooz *et al.* established numerical wave tanks with piston-type and flap-type wavemakers for water wave generation simulations, a damping zone was set up in the model to suppress the reflection of water waves [54]. Chen *et al.* studied the effect of relaxation method applied to numerical water tanks on the absorption of different types of waves, an improvement of the relaxation method that allows shortening the length of the relaxation zone and saving computational resources was proposed [105]. De Vita *et al.* constructed a numerical wave tank using a pressure-based relaxation zone method, and an absorption zone was set up to suppress the reflection of water waves [106]. Jacobsen *et al.* performed numerical simulations of water wave generation using a generic wave generation method, the same method was used to construct a wave relaxation zone for absorbing water waves, and the reflection coefficient was analyzed with different parameters setup [107]. Perić *et al.* used an implicit relaxation zone to minimize wave reflections at domain boundaries in free surface wave simulations, and an analytical method was proposed to optimize the relaxation effect and predict the optimal relaxation parameters [108].

In computational environments where water wave generation is simulated via the ALE method (software such as LS-DYNA, Radioss and OpenRadioss), the Rayleigh mass and stiffness damping options are a reliable solution for suppressing water wave reflections without increasing the model complexity. The Rayleigh damping, also usually referred to as proportional damping, can be traced back to Rayleigh's work on vibration in 1877 [109, 110]. The concept of Rayleigh damping is an approximation to viscous damping and it has been subsequently developed and applied to the dynamic analysis of structures. In numerical studies, the Rayleigh damping can also be used to model the energy dissipation characteristics of a structure due to internal friction. Therefore, it is desirable to use the Rayleigh damping in water wave generation simulations to set up a damping zone at the far-field boundary to dissipate the energy of water

waves propagating to this zone and thus suppress the reflected water waves.

With the Rayleigh damping method, the damping matrix $[C]$ is constructed from a linear combination of the mass matrix $[M]$ and the stiffness matrix $[K]$ that are respectively multiplied by the proportional coefficients α and β. Both two coefficients are pre-defined constants, where α is the mass weighted damping coefficient and β is the stiffness weighted damping coefficient. So, the damping matrix $[C]$ can be expressed as follows,

$$[C] = \alpha\,[M] + \beta\,[K]. \tag{2.52}$$

For a finite element model, the application of a proportional damping matrix permits the global equilibrium equation to be reduced to n number of uncoupled equations by using the orthogonal transformation. Taking a global equilibrium equation that is expressed as follows,

$$[M]\,\{\ddot{X}\} + [C]\,\{\dot{X}\} + [K]\,\{X\} = \{F_T\}, \tag{2.53}$$

where $\{X\}$ may represent matrices of displacement or deformation depending on the analyzed case, and $\{F_T\}$ represents the matrix of total force.

Then, the transformed uncoupled system of equations can be written as follows,

$$[\varphi]^T\,[M\ \boldsymbol{I}\ \varphi]\,\{\ddot{\xi}\} + [\varphi]^T\,[C\ \boldsymbol{I}\ \varphi]\,\{\dot{\xi}\} + [\varphi]^T\,[K\ \boldsymbol{I}\ \varphi]\,\{\xi\} = [\varphi]^T\,\{F_T\}, \tag{2.54}$$

from which the second term about the damping can be expressed as follows,

$$[\varphi]^T\,[C\ \boldsymbol{I}\ \varphi] = \begin{bmatrix} \alpha+\beta\omega_1^2 & 0 & ... & 0 \\ 0 & \alpha+\beta\omega_2^2 & ... & 0 \\ . & . & ... & 0 \\ . & . & ... & 0 \\ 0 & . & ... & \alpha+\beta\omega_n^2 \end{bmatrix}, \tag{2.55}$$

where $[\boldsymbol{I}]$ is the identity matrix.

As for the uncoupled equation system, every uncoupled equation can be expressed as follows,

$$\ddot{\xi}_i + 2\omega_i\zeta_i\dot{\xi}_i + \omega_i^2\xi_i = f_i^t \text{ with } i = 1 \ldots n, \tag{2.56}$$

where ω_i represents the i^{th} natural frequency of the system, and ζ_i represents the i^{th} damping ratio.

Then, the relationship between the damping coefficients, natural frequency and damping ratio can be obtained. The related equation is expressed as follows,

$$2\omega_i\zeta_i = \alpha + \beta\omega_i^2. \tag{2.57}$$

It can be clearly derived that the damping ratio is nonlinear with respect to the natural frequency when only mass damping is used, with the expression written as follows,

$$\zeta_i = \frac{\alpha}{2\omega_i}, \tag{2.58}$$

and accordingly, when only elastic damping is used, damping ratio is linear with respect to the natural frequency, with the expression written as follows,

$$\zeta_i = \frac{\beta\omega_i}{2}. \tag{2.59}$$

Thus, for a system using both mass damping and stiffness damping, the relationship between damping ratio and natural frequency can be described by Figure 2.7.

And furthermore, it can be concluded that these two damping options are more significant under different scenarios. That is, for the damping of low-frequency structures, the use of a mass weighted damping is a favored choice, whereas the stiffness weighted damping is more suitable to act on high-frequency structures.

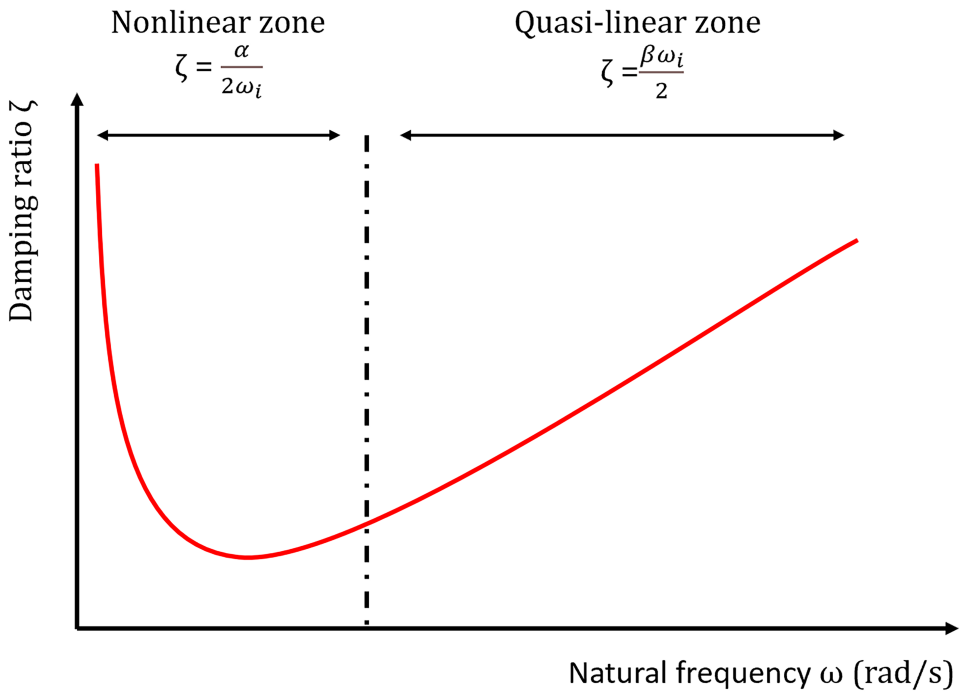


Figure 2.7: Diagram of the Rayleigh Mass and Stiffness Damping

2.4 Conclusion

This chapter discussed the linear water wave theory, the piston-type wave-maker theory used for water wave generation experiments, and the Rayleigh damping model used for water wave absorption.

There are various theories used to study water wave phenomena. The relevant theories have been able to cover linear, nonlinear water waves, as well as more complex irregular water waves. The linear wave theory was chosen for the numerical simulation of water wave generation. This theory assumes that the amplitude of water waves is small to allow for the linearization of the problem. Although it is a basic water wave theory, it is widely used in water wave research, wave load calculations, and coastal protection against water waves. First, in order to establish the mathematical description of the water wave problem, a model is proposed with Laplace's equation Eq. 2.7 as the governing equation,

including the lateral boundary condition Eq. 2.8, the bottom boundary condition Eq. 2.11, and the free-surface boundary conditions Eq. 2.14, Eq. 2.23. Then, above conditions are linearized as much as possible by the linear wave assumption, and the simplified linear water wave description is given, including Eq. 2.7, Eq. 2.11 and Eq. 2.28.

The construction of a wave flume is a commonly used approach to study water wave generation and related FSI problems, both in physical experiments and numerical simulations. This method uses the disturbances created by a wavemaker to generate water waves. The commonly used wavemakers include the piston-type and flap-type. The piston-type wavemaker has been selected for intermediate water depth and shallow water conditions. Appropriate utilization of the transfer function between the wavemaker and target wave profile is an important step in accurately generating water waves. The transfer function of the linear water wave generation via the piston-type wavemaker is derived, that is, the Biésel transfer function, Eq. 2.50, Eq. 2.51.Then, three characteristic ratio parameters used to characterize the water waves are discussed, and dimensions of the wave flume also determines, to some extent, the range of reasonable water waves that can be generated.

In wave flume experiments, the reflection of water waves after contacting the boundary is unavoidable. Commonly used methods for absorbing water waves are discussed, including passive methods using porous structures and slopes, and active method that controls the motion of the wavemaker. However, for numerical wave flume simulations, a damping zone set at the distal end represents a better alternative. Commonly used damping model is the Rayleigh damping method. This method consists of both mass weighted damping and stiffness weighted damping. The relationship Eq. 2.57 between damping ratio and natural frequency in the Rayleigh damping method is given. And it is analyzed and concluded that the Rayleigh mass damping is more suitable for low frequency scenarios such as water waves.

Chapter 3

Numerical Method for Fluid-Structure Interaction Simulation

3.1 Arbitrary Lagrangian Eulerian Method

For the solution of FSI problems, both the classical Lagrangian method and Eulerian method have shortcomings, hence the ALE method was developed. The ALE method can be traced back to Noh's work published in 1963, where the Coupled Euler-Lagrange (CEL) code through difference approximation was described and used for coupling the Eulerian approximation of a fluid with a Lagrange approximation for each of the adjacent fluid regions [111]. Then, the ALE method combined with the finite element method had been developed to solve FSI problems. Donea *et al.* first developed a finite element method for dealing with the nonlinear transient response of coupled hydrodynamic-structure problems in the safety analysis of nuclear reactor components [112]. Donea *et al.* then proposed a finite element model using the ALE method for predicting the

nonlinear response of fluid-structure systems under transient dynamic loading [62]. Belytschko *et al.* proposed a quasi-Eulerian finite element formulation for transient analysis of a fluid containing pressurized bubbles [113]. Since then, the ALE method has been developed to be able to solve a wide range of FSI problems involving free surface, multi-material, coupled fluid-structure loads, and so on. The ALE method has been implanted in many finite element solvers such as LS-DYNA, Radioss, OpenRadioss.

The application of ALE method in FSI problems has been mentioned before. In particular, the effectiveness of the ALE method for the water wave problem and computation of wave loads has also been verified by many studies. Loiseau used the ALE method to study the boundary layer behavior of water waves or ocean currents for the sediment transport problem [114]. Wang and Jin used the ALE method to simulate the wave transformation, impact and overtopping on a rubble mound breakwater [115]. Xiang and Istrati used the ALE method to evaluate the impact of extreme waves on coastal decks with different geometries [116]. Pákozdi *et al.* proposed a new approach of numerical wave tank modeling for wave force estimation using the α-grid with strip theory and the Morison equation in ALE framework [117]. Tsao and Kees used the ALE based regularized boundary integral method to simulate the water wave transformation over complex topography and wave–structure interaction problem based on a fully nonlinear potential theory [118]. Fan *et al.* used the ALE method to study the fluid-structure interaction process of high-speed vehicles during water entry, and the flow field pressure distribution, cavitation evolution characteristics and vehicle force characteristics were analyzed in order to understand the impact of the water-entry angle [119].

3.1.1 ALE Description and Referential Domain

The Lagrangian and Eulerian formulations are respectively the classical methods for processing numerical simulations of structural analysis and fluid

dynamics. For the Lagrange formulation, the elements deform with the material. Whereas for the Eulerian formulation, the nodes are fixed in space and the material travels through the mesh. However, in the face of FSI problems with potentially large deformations and interface tracking requirements, using one of these formulations in isolation is not an effective approach. The ALE formulation, on the other hand, is a combination of two different finite element modeling techniques, the Lagrangian formulation and the Eulerian formulation. In the ALE description, the internal nodes move with the material to minimize possible element distortions, while the boundary nodes remain fixed at the domain boundaries.

In order to achieve this, in addition to the classical material domain (Lagrangian configuration) and spatial domain (Eulerian configuration), a new domain, the referential domain, is introduced to identify the grid points. In other words, the ALE description considers two superimposed meshes, including a deformable Lagrangian mesh for structures and a fixed Eulerian or ALE mesh for fluids. When large deformations are present, the mesh distortion can be reduced by realizing a motion of the internal nodes through the referential domain.

Now, consider three domains, the material domain Ω_0, the spatial domain Ω_t and the referential domain $\hat{\Omega}$. Material domain represents the initial configuration of a finite continuum body at $t = 0$, with its boundary being Γ_0. Spatial domain represents the configuration of this continuum body at the time t, and its boundary is Γ_t. Then, the referential domain represents an arbitrary grid domain whose boundary is $\hat{\Gamma}$. For material domain, the coordinates of all the material points of which the continuum body is composed are expressed in terms of $\vec{X}$. And at the time t, the coordinates of all material points comprising the spatial domain are expressed by $\vec{x}$. In addition, the coordinates of all material points of the referential domain are then expressed by $\vec{\xi}$.

It is necessary to relate these three domains. Therefore, it is desirable to find the transformation functions between the coordinates of the three domains. If there exists an injective function $\vec{\Phi}$ that allows expressing the coordinates of

the spatial domain $\vec{x}$ in terms of coordinates of the material domain $\vec{X}$ and time t, expressed as follows,

$$\vec{x} = \vec{\Phi}(\vec{X}, t). \tag{3.1}$$

And also, an injective function $\vec{\hat{\Phi}}$ that allows the coordinates of the spatial domain $\vec{x}$ to be expressed using coordinates of the referential domain $\vec{\xi}$ and time t, expressed as follows,

$$\vec{x} = \vec{\hat{\Phi}}(\vec{\xi}, t). \tag{3.2}$$

Then, the description of three domains and the transformation of their coordinates through injective functions $\vec{\Phi}$ and $\vec{\hat{\Phi}}$ can be shown in Figure 3.1, with $\vec{t}_0$, $\vec{t}$ and $\vec{\hat{t}}$ representing respectively the traction set at boundaries $\Gamma_0^{\vec{t}}$, $\Gamma_t^{\vec{t}}$ and $\hat{\Gamma}^{\vec{t}}$, and with $\vec{v}_0$, $\vec{v}$ and $\vec{\hat{v}}$ representing respectively the velocity set at boundaries $\Gamma_0^{\vec{v}}$, $\Gamma_t^{\vec{v}}$ and $\hat{\Gamma}^{\vec{v}}$.

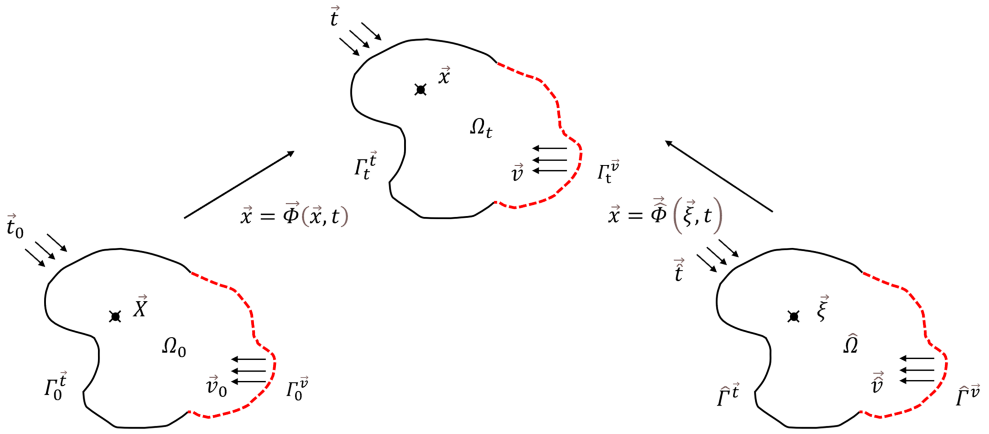


Figure 3.1: Material Domain, Spatial Domain, Referential Domain and the Transformation of Coordinates

Lagrangian to Eulerian description

For the transformation from the material domain to the spatial domain, following discussion is carried out. Coordinates of the material domain adopt the Lagrangian description and are associated with the material points. In the per-

spective of the material domain as the reference, the coordinates are independent of time. In contrast, coordinates of the spatial domain adopt the Eulerian description, and these coordinates are independent of space and time, no matter which perspective is taken as the reference.

For the displacement vector $\vec{u}$ of a material mass, it can be expressed as follows,

$$\begin{aligned} &\vec{u}(\vec{X},t) = \vec{\Phi}(\vec{X},t) - \vec{X} = \vec{x} - \vec{X} \\ &\text{or} \\ &u_i(\vec{X},t) = \Phi_i(\vec{X},t) - X_i = x_i - X_i, \end{aligned} \tag{3.3}$$

where the index i depends on dimensions of the studied problem.

Then, the velocity vector $\dot{\vec{u}}$ of a material point can be obtained through the time derivative of the displacement vector, expressed as follows,

$$\begin{aligned} &\dot{\vec{u}}(\vec{X},t) = \vec{v}(\vec{X},t) = \frac{\partial \vec{u}}{\partial t} = \frac{\partial \vec{\Phi}}{\partial t}(\vec{X},t) \\ &\text{or} \\ &\dot{u}_i(\vec{X},t) = v_i(\vec{X},t) = \frac{\partial u_i}{\partial t} = \frac{\partial \Phi_i}{\partial t}(\vec{X},t). \end{aligned} \tag{3.4}$$

In the same way, the acceleration vector $\dot{\vec{v}}$ can be obtained and expressed as follows,

$$\begin{aligned} &\dot{\vec{v}}(\vec{X},t) = \vec{a}(\vec{X},t) = \frac{\partial \vec{v}}{\partial t} = \frac{\partial^2 \vec{\Phi}}{\partial t^2}(\vec{X},t) \\ &\text{or} \\ &\dot{v}_i(\vec{X},t) = a_i(\vec{X},t) = \frac{\partial v_i}{\partial t} = \frac{\partial^2 \Phi_i}{\partial t^2}(\vec{X},t). \end{aligned} \tag{3.5}$$

Above equations are expressed as a function of spatial coordinates. And in order to transfer to the Eulerian description, a further application of the material

derivatives is required, which is expressed as follows,

$$\frac{D}{Dt} = \frac{\partial}{\partial t} + \vec{v} \cdot \vec{\nabla}. \tag{3.6}$$

Therefore, the material domain and the spatial domain can also be connected in such a way, that is, the material derivative in terms of space domain coordinates and time is equivalent to the partial derivative in terms of material domain coordinates and time, which is expressed as follows,

$$\frac{D}{Dt}(\vec{x}, t) = \frac{\partial}{\partial t}(\vec{X}, t). \tag{3.7}$$

ALE description

In analogy to above discussion of the transformation from the Lagrangian description to the Eulerian description, for the referential domain representing an arbitrary grid domain, the grid displacement $\vec{\hat{u}}$ can be expressed as follows,

$$\begin{aligned} &\vec{\hat{u}}(\vec{\xi}, t) = \vec{\hat{\Phi}}(\vec{\xi}, t) - \vec{\xi} = \vec{x} - \vec{\xi} \\ &\text{or} \\ &\hat{u}_i = \hat{\Phi}_i(\vec{\xi}, t) - \xi_i = x_i - \xi_i \end{aligned} \tag{3.8}$$

Then, the grid velocity vector $\vec{\hat{v}}$ can be obtained through the time derivative of the grid displacement vector, expressed as follows,

$$\begin{aligned} &\vec{\hat{v}}(\vec{\xi}, t) = \frac{\partial \vec{\hat{u}}}{\partial t}(\vec{\xi}, t) = \frac{\partial \vec{\hat{\Phi}}}{\partial t}(\vec{\xi}, t) \\ &\text{or} \\ &\hat{v}_i(\vec{\xi}, t) = \frac{\partial \hat{u}_i}{\partial t}(\vec{\xi}, t) = \frac{\partial \hat{\Phi}_i}{\partial t}(\vec{\xi}, t). \end{aligned} \tag{3.9}$$

Now, consider a function $f(\vec{x}, t)$ with spatial domain coordinates $\vec{x}$ and time t as variables, and the expression of this function in the referential domain can

be written as follows,

$$f(\vec{x},t) = f\left(\vec{\hat{\Phi}}(\vec{\xi},t),t\right) = f_{ale}(\vec{\xi},t). \tag{3.10}$$

And the partial derivative of time of the function $f_{ale}(\vec{\xi},t)$ with respect to the referential domain can be expressed as follows,

$$\frac{\partial f_{ale}(\vec{\xi},t)}{\partial t} = \frac{\partial f(\vec{x},t)}{\partial t} + \frac{\partial \vec{\hat{\Phi}}(\vec{\xi},t)}{\partial t} \cdot \vec{\nabla} f(\vec{x},t). \tag{3.11}$$

It can be seen that the grid velocity $\vec{\hat{v}}$ is involved.

On the other hand, by means of the Eq. 3.7 defined earlier which connects the material and spatial domains, the material derivative of the function $f(\vec{x},t)$ can be expressed as follows,

$$\frac{Df(\vec{x},t)}{Dt} = \frac{\partial f(\vec{x},t)}{\partial t} + \vec{v} \cdot \vec{\nabla} f(\vec{x},t). \tag{3.12}$$

Combining Eq. 3.11 and Eq. 3.12, the partial derivative with respect to time in the referential domain can be related to the material derivative with respect to time, expressed as follows,

$$\frac{Df}{Dt} = \frac{\partial f_{ale}}{\partial t} + (\vec{v} - \vec{\hat{v}}) \cdot \vec{\nabla} f, \tag{3.13}$$

where the term $\vec{v} - \vec{\hat{v}}$ can be defined as the convective velocity $\vec{w}$, that is, $\vec{w} = (\vec{v} - \vec{\hat{v}})$. Thus, convective velocity represents the difference in velocity between the fluid and the grid in the referential domain.

The term of convective velocity can help understand the ALE description. There are two special cases:

– When the velocity of material points $\vec{v}$ in the material domain is identical to the grid velocity $\vec{\hat{v}}$ in the referential domain, that is, $\vec{v} = \vec{\hat{v}}$, the convective velocity is equal to zero, $\vec{w} = 0$. Then, the Eq. 3.13 is reduced to Eq. 3.7,

as follows,

$$\frac{Df}{Dt} = \frac{\partial f_{ale}}{\partial t}. \tag{3.14}$$

The ALE formulation is reduced to the Lagrangian description.

– When the grid velocity $\vec{\hat{v}}$ in the referential domain equals zero, that is, $\vec{\hat{v}} = 0$, the convective velocity $\vec{w}$ is equal to the velocity of material points $\vec{v}$ in the material domain, $\vec{w} = \vec{v}$. Thus, the Eq. 3.13 is reduced to Eq. 3.6, as follows,

$$\frac{Df}{Dt} = \frac{\partial f_{ale}}{\partial t} + \vec{v} \cdot \vec{\nabla} f. \tag{3.15}$$

The ALE formulation is reduced to the Eulerian description.

3.1.2 ALE Navier–Stokes Governing Equations

In most CFD solvers, the governing equations implanted to describe fluids are the Navier-Stokes (NS) equations. NS equations take into account the viscosity of fluids, which is considerably more realistic and can be applied to a wider range of fluid analysis. In general, for a compressible Newtonian fluid, the NS equations include the continuity equation, momentum conservation equation and energy conservation equation that need to be satisfied, expressed as follows,

$$\begin{aligned}
&\frac{\partial \rho}{\partial t} + \vec{\nabla} \cdot (\rho \vec{v}) = 0 \\
&\rho \frac{\partial \vec{v}}{\partial t} + \vec{v} \cdot \vec{\nabla}(\rho \vec{v}) = -\vec{\nabla} p + \vec{\nabla} \cdot \mathbf{\Omega} + \rho \vec{g} \\
&\rho \frac{\partial E}{\partial t} + \vec{\nabla} \cdot (\rho E \vec{v}) = \vec{\nabla} \cdot (\mathbf{\Sigma} \cdot \vec{v}) + \rho \vec{g} \vec{v},
\end{aligned} \tag{3.16}$$

where ρ represents the density of the fluid, $\vec{v}$ represents the velocity of a fluid particle, p represents the pressure, $\mathbf{\Omega}$ represents the viscous stress tensor, $\vec{g}$ represents the gravity, E represents the total energy per unit mass, $\mathbf{\Sigma}$ represents the stress tensor with $\mathbf{\Sigma} = \mathbf{\Omega} - p\boldsymbol{I}$, and $\boldsymbol{I}$ is the identity matrix. Also,

above equations do not include the heat term.

Although in the description of water wave problem in the previous chapter, the linear wave theory was used, the NS governing equations can still be applied. This is because when considering incompressible non-viscous fluids, the momentum equation in the NS equations can be reduced to Euler's equation Eq. 2.15, which in combination with the continuity equation Eq. 2.4 can still lead to the governing equation of the linear water wave, the Laplace's equation Eq. 2.7.

Subsequently, the NS governing equations under the ALE description in the considered case can be obtained. The mass conservation equation can be expressed as follows,

$$\frac{\partial \rho}{\partial t}(\vec{\xi}, t) + (\vec{v} - \hat{\vec{v}}) \cdot \vec{\nabla}\rho + \rho\vec{\nabla} \cdot \vec{v} = 0 \text{ in } \Omega_t \ . \tag{3.17}$$

The momentum conservation equation can be expressed as follows,

$$\rho\frac{\partial \vec{v}}{\partial t}(\vec{\xi}, t) + \rho(\vec{v} - \hat{\vec{v}}) \cdot \vec{\nabla}\vec{v} = \vec{\nabla} \cdot \mathbf{\Sigma} + \rho\vec{b} \text{ in } \Omega_t \ , \tag{3.18}$$

where $\vec{b}$ represents a force per unit mass from the body force generally being the gravity.

And the energy conservation equation can be expressed as follows,

$$\rho\frac{\partial e}{\partial t}(\vec{\xi}, t) + \rho(\vec{v} - \hat{\vec{v}}) \cdot \vec{\nabla}e = \vec{\nabla} \cdot (\mathbf{\Sigma} \cdot \vec{v}) + \rho\vec{b}\vec{v}, \tag{3.19}$$

where e represents the internal energy with $E = e + v_i v_i/2$.

In order to complete the description of the problem, the constitutive equation of the fluid need to be first constructed. Constitutive equation allows the stress tensor $\mathbf{\Sigma}$ to be described in terms of strain rate of the fluid. And stress tensor $\mathbf{\Sigma}$ can be considered to consist of a part related to the pressure and a part related to the viscous force, the viscous stress tensor $\mathbf{\Omega}$. Then, the stress

tensor $\boldsymbol{\Sigma}$ can be expressed as follows,

$$\begin{aligned} &\boldsymbol{\Sigma} = \boldsymbol{\Omega} + \frac{1}{3} tr(\boldsymbol{\Sigma})\ \boldsymbol{I} \\ &\text{or} \\ &\sigma_{ij} = \omega_{ij} + \frac{1}{3}(\sigma_{kk}\delta_{ij})\ , \end{aligned} \tag{3.20}$$

where σ_{ij}, ω_{ij} are respectively the components of $boldsymbol\Sigma$ and $\boldsymbol{\Omega}$. And δ_{ij} is the Kronecker symbol.

The $\boldsymbol{\Omega}$ is the part that relates to strain of the fluid. For a viscous Newtonian fluid, $\boldsymbol{\Omega}$ represents the viscous force and it depends linearly on the strain rate tensor $\boldsymbol{D}$. Then, the condition of isotropy allows relating the stress tensor to the instantaneous values of strain using the Lamé coefficients (λ and μ) of the fluid. Thus, the constitutive equation that describes the behavior of the fluid can be expressed as follows,

$$\begin{aligned} &\boldsymbol{\Sigma} = -p\boldsymbol{I} + 2\mu\boldsymbol{D} + \lambda tr(\boldsymbol{D})\boldsymbol{I} \\ &\text{or} \\ &\sigma_{ij} = -p\delta_{ij} + 2\mu d_{ij} + \lambda(d_{kk}\delta_{ij})\ , \end{aligned} \tag{3.21}$$

where d_{ij} represents the components of $\boldsymbol{D}$. The term p represents the thermodynamic pressure which depends on the equation of state of the fluid.

In the same way, the strain rate tensor $\boldsymbol{D}$ can be regarded as symmetric and consists of a spherical tensor related to the variation of volume of the fluid and a deviatoric tensor $\tilde{\boldsymbol{D}}$ related to the strain of the fluid without volume change ($tr(\tilde{\boldsymbol{D}} = 0)$). And the relationship can be obtained as follows,

$$\begin{aligned} &\frac{1}{3} tr(\boldsymbol{\Sigma}) = -p + \eta\ tr(\boldsymbol{D}) \\ &\text{or} \\ &\boldsymbol{\Omega} = 2\mu\tilde{\boldsymbol{D}}\ , \end{aligned} \tag{3.22}$$

where μ here represents the dynamic viscosity coefficient with $\nu = \mu/\rho$, and ν is the kinematic viscosity coefficient. Then, η represents the bulk viscosity coefficient with $\eta = (2\mu + 3\lambda)/3$.

Usually, for common fluids such as water and air, the bulk viscosity is considered to be small with $2\mu + 3\lambda = 0$. The constitutive equation of the fluid can finally be obtained as follows,

$$\begin{aligned} &\boldsymbol{\Sigma} = -p\boldsymbol{I} + 2\mu\left[\boldsymbol{D} - \frac{1}{3}tr(\boldsymbol{D})\boldsymbol{I}\right] \\ &\text{or} \\ &\sigma_{ij} = -p\delta_{ij} + 2\mu(d_{ij} - \frac{1}{3}d_{kk}\delta_{ij}) \ . \end{aligned} \tag{3.23}$$

Then, for the boundary conditions regarding traction and velocity in Figure 3.1, they can be expressed as follows,

$$n_j(\vec{\xi}, t)\ \sigma_{ji}(\vec{\xi}, t) = t_i(\vec{\xi}, t) \text{ on } \Gamma^t, \tag{3.24}$$

and

$$v_i(\vec{\xi}, t) = v_i(\vec{\xi}, t) \text{ on } \Gamma^v. \tag{3.25}$$

Finally, the initial conditions on the domain Ω_0 can be expressed as follows,

$$\begin{aligned} &\vec{v}(\vec{X}, 0) = \vec{v_0}(\vec{X}) \\ &\text{and} \\ &\boldsymbol{\Sigma}(\vec{X}, 0) = \boldsymbol{\Sigma_0}(\vec{X}) \ . \end{aligned} \tag{3.26}$$

3.1.3 Weak Formulation

For the resolution of the ALE NS equations Eq. 3.17, Eq. 3.18, and Eq. 3.19, the difficulty lies in the treatment of nonlinear terms related to the convective velocity. First of all, the most straightforward solution is to solve the fully coupled ALE NS equations. Through the Galerkin method, weak formula-

tion of the ALE NS equations can be obtained. Weak formulation of the mass conservation equation can be expressed as follows,

$$\int_{\Omega_t} \delta\rho \frac{\partial \rho}{\partial t}(\vec{\xi}, t)\ d\Omega_t + \int_{\Omega_t} \delta\rho \frac{\partial \rho}{\partial x_i} w_i\ d\Omega_t + \int_{\Omega_t} \delta\rho\rho \frac{\partial v_i}{\partial x_i}\ d\Omega_t = 0. \tag{3.27}$$

Weak formulation of the momentum conservation equation can be expressed as follows,

$$\begin{aligned} \int_{\Omega_t} \delta v_i \rho \frac{\partial v_i}{\partial t}(\vec{\xi}, t)\ d\Omega_t + \int_{\Omega_t} \delta v_i \rho \frac{\partial v_i}{\partial x_j} w_j\ d\Omega_t = & \int_{\Omega_t} \frac{\partial(\delta v_i)}{\partial x_j} \sigma_{ij}\ d\Omega_t \\ & + \int_{\Gamma_t^t} \delta v_i t_i\ d\Gamma_t \\ & + \int_{\Omega_t} \delta v_i \rho b_i\ d\Omega_t\ . \end{aligned} \tag{3.28}$$

And weak formulation of the energy conservation equation can be expressed as follows,

$$\begin{aligned} \int_{\Omega_t} \delta e \frac{\partial e}{\partial t}(\vec{\xi}, t)\ d\Omega_t + \int_{\Omega_t} \delta e \rho \frac{\partial e}{\partial x_i} w_i\ d\Omega_t = & \int_{\Omega_t} \delta e \frac{\partial v_i}{\partial x_j} \sigma_{ij}\ d\Omega_t \\ & + \int_{\Omega_t} \delta e v_i \rho b_i\ d\Omega_t\ . \end{aligned} \tag{3.29}$$

For above three equations, the terms $\delta\rho \in \mathbb{H}^1(\Omega_t)$, $\delta v_i \in \mathbb{H}^1(\Omega_t)$ and $\delta e \in \mathbb{H}^1(\Omega_t)$ are test functions applied respectively to balance the errors generated within three conservation equations.

However, this approach may cause unstable results when dealing with second-order advection terms. To solve this problem, a Petrov-Galerkin (PG) type approximation method can be used. The computation results can be stabilized by an improved test function, expressed as follows,

$$\delta v_i^{PG} = \delta v_i + |\alpha| \frac{L}{2} \frac{c_j}{\|\vec{c}\|} \frac{\partial(\delta v_i)}{\partial x_j} \text{ with } \alpha = \coth(\mathcal{P}_e) - \frac{1}{\mathcal{P}_e}\ , \tag{3.30}$$

where L represents a characteristic parameter and corresponds to the length

of elements. The term $\mathcal{P}_e$ is the Péclet number that describes the stability of results, written as follows,

$$\mathcal{P}_e = \frac{v\Delta x}{2\nu} \ , \tag{3.31}$$

where v represents the flow velocity, Δx represents a characteristic length that equals the discretization length, and ν the kinematic viscosity coefficient.

This improved method is called the Streamline Upwind Petrov-Galerkin (SUPG) method [120]. Some discussion of this method and about some of these parameters can be found in the studies of Hughes *et al.* [121, 122].

3.1.4 Split Method

Except for solving directly the fully coupled equations, there is a second method that is more commonly used and effective, and this method is called the "split" method. This approach can be traced back to the work of Chorin *et al.*, where the product formulas that effectively related the functional analysis and numerical methods are discussed, some cases are presented and the accuracy of the method is verified [123]. This approach has been developed and applied. Benson summarized in detail the hydrodynamic computational algorithms including the Lagrangian, Eulerian, and ALE methods in his study, and the "operator split" method has also been described [124]. In the works introducing the application of ALE method in FSI simulations, the split method is also used as the main approach to solve the NS governing equations [125, 126].

Applied to the ALE formulation, the split method separates the Lagrangian and advection terms in the governing equations Eq. 3.17, Eq. 3.18 and Eq. 3.19 at each time step and solves them in two sequential computational cycles, namely the Lagrangian phase and the advection phase.

For introducing this approach, consider the simple case of an equation con-

taining the Lagrangian and advection terms, written as follows,

$$\frac{\partial \phi(\vec{x},t)}{\partial t} + \vec{w} \cdot \vec{\nabla}\phi(\vec{x},t) = S(\vec{x},t) \ , \tag{3.32}$$

where $\phi(\vec{x},t)$ represents a solution function in terms of space variables $\vec{x}$ and time t, and $S(\vec{x},t)$ represents the source term.

The split method divides above equation into two equations that need to be solved successively, the first step solves the Lagrangian equation expressed as follows,

$$\frac{\partial \phi(\vec{x},t)}{\partial t} = S(\vec{x},t) \ . \tag{3.33}$$

In the second step, the equation containing the advection term expressed as follows is solved,

$$\frac{\partial \phi(\vec{x},t)}{\partial t} + \vec{w} \cdot \vec{\nabla}\phi(\vec{x},t) = 0 \ . \tag{3.34}$$

Following this approach, the NS governing equations can be separated. In the Lagrangian phase, the equations are written as follows,

$$\begin{aligned} &\frac{\partial \rho}{\partial t} + \rho \vec{\nabla} \cdot \vec{v} = 0 \\ &\rho \frac{\partial \vec{v}}{\partial t} - \vec{\nabla} \cdot \mathbf{\Sigma} - \rho \vec{b} = 0 \\ &\rho \frac{\partial e}{\partial t} - \vec{\nabla} \cdot (\mathbf{\Sigma} \cdot \vec{v}) - \rho \vec{b} \vec{v} = 0 \ . \end{aligned} \tag{3.35}$$

And in the advection phase, the equations are written as follows,

$$\begin{aligned} &\frac{\partial \rho}{\partial t}(\vec{\xi},t) + \vec{w} \cdot \vec{\nabla}\rho = 0 \\ &\rho \frac{\partial \vec{v}}{\partial t}(\vec{\xi},t) + \rho \vec{w} \vec{\nabla} \vec{v} = 0 \\ &\rho \frac{\partial e}{\partial t}(\vec{\xi},t) + \rho \vec{w} \vec{\nabla} e = 0 \ . \end{aligned} \tag{3.36}$$

In the Lagrangian phase, the explicit finite element method (FEM) is applied and the mesh moves following with the fluid particles. Since at this phase

the mass conservation equation reduces to an algebraic equation, only the weak formulation of the momentum conservation and energy conservation are treated. By applying Eq. 3.13 which relates the material derivative in the Lagrangian description to the partial derivative in the ALE description, the weak formulation of the momentum conservation Eq. 3.28 can be rewritten as follows,

$$\int_{\Omega_t} \delta v_i \rho \frac{Dv_i}{Dt} \, d\Omega_t = \int_{\Omega_t} \frac{\partial(\delta v_i)}{\partial x_j} \sigma_{ij} \, d\Omega_t + \int_{\Gamma_t^t} \delta v_i t_i \, d\Gamma_t + \int_{\Omega_t} \delta v_i \rho b_i \, d\Omega_t \, . \tag{3.37}$$

And the weak formulation of the energy conservation Eq. 3.29 can be rewritten as follows,

$$\int_{\Omega_t} \delta e \frac{De}{Dt} \, d\Omega_t = \int_{\Omega_t} \delta e \frac{\partial v_i}{\partial x_j} \sigma_{ij} \, d\Omega_t + \int_{\Omega_t} \delta e v_i \rho b_i \, d\Omega_t \, . \tag{3.38}$$

For a general simulation of water wave generation where the fluid is considered incompressible, the approximate computational steps for a cycle of the Lagrangian phase are as follows:

(a) Compute nodal internal forces and accelerations based on the stress and pressure data of each element at time t^n;

(b) Integrate the acceleration data to get the velocities at time $t^{n+1/2}$;

(c) Integrate the velocity data to get the nodal displacement at time t^{n+1}, and update the mesh position based on the displacement data;

(d) Compute the strain rate and the corresponding internal forces related to the materials;

(e) Upgrade internal energy data;

(f) Compute the pressure data using the equation of state based on the density and internal energy data;

(g) Compute the next time step until convergence according to convergence condition by Courant-Friedrichs-Lewy (CFL).

Then, in the advection phase, the equations Eq. 3.36 are treated. These equations are also called equations of transport, involving the hyperbolic problems. The time t at this phase does not correspond to the physical time, because it's the transport of the results obtained in the Lagrangian phase that needs to be processed. In fact, the movement of the fluid is fixed in the physical configuration, whereas it is the mesh that moves. And the equations of transport do not determine the physical convection of the fluid. Therefore, the initial conditions of the advection phase, $\rho(\vec{\xi},t)$, $\vec{v}(\vec{\xi},t)$ and $e(\vec{\xi},t)$, correspond respectively to the results derived from the Lagrangian phase.

The advection phase is solved using the finite volume method (FVM), which involves dealing with the conservative form of the equations Eq. 3.36. First, it is needed to introduce the Jacobian $J_{\hat{\Phi}}$ of the injective function $\vec{\hat{\Phi}}$, which is expressed as follows,

$$\frac{\partial J_{\hat{\Phi}}}{\partial t}(\vec{\xi},t) = J_{\hat{\Phi}}\vec{\nabla}\vec{v}(\vec{\xi},t)\ . \tag{3.39}$$

Then, the conservative form of the equations Eq. 3.36 can be written as follows,

$$\begin{aligned}
&\frac{\partial(\rho J_{\hat{\Phi}})}{\partial t}(\vec{\xi},t) + J_{\hat{\Phi}}\vec{\nabla}(\rho\vec{w}) = 0\\
&\frac{\partial(\rho\vec{v} J_{\hat{\Phi}})}{\partial t}(\vec{\xi},t) + J_{\hat{\Phi}}\vec{\nabla}(\rho\vec{w}\otimes\vec{v}) = 0\\
&\frac{\partial(\rho e J_{\hat{\Phi}})}{\partial t}(\vec{\xi},t) + J_{\hat{\Phi}}\vec{\nabla}(\rho\vec{w}e) = 0\ .
\end{aligned} \tag{3.40}$$

These equations allow the projection of the physical variables obtained in the Lagrangian phase onto a new mesh determined by the convective velocity $\vec{w}$. The process of the advection phase can be divided into following steps:

(a) Depending on the convective velocity, either go back to the initial fixed mesh according to the Eulerian description, or generate a new mesh by relaxing

the Lagrangian mesh according to the ALE description;

(b) Project element based variables such as stress and internal energy through an advection algorithm;

(c) Projects the nodal velocities through, for example, a Half index shift (HIS) scheme.

3.1.5 Lagrangian Phase Computation

In the Lagrangian phase, important computations include: nodal acceleration, velocity, displacement, internal energy and pressure.

Consider that the fluid computational domain is composed of the typical 8-node solid element Ω_t^e, as shown in Figure 3.2.

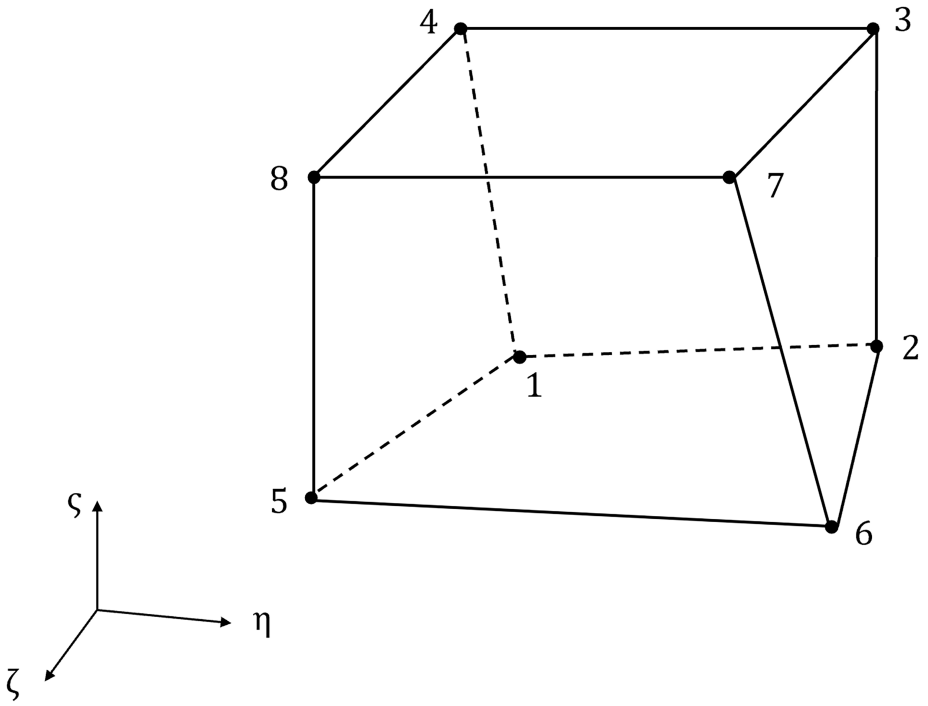


Figure 3.2: 8-Node Solid Element

Then, the displacement of the element can be expressed as follows,

$$\vec{x}(\vec{\zeta}, t) = \sum_{I=1}^{8} \vec{x}_I(t) N_I(\vec{\zeta}) \ , \tag{3.41}$$

where ζ represents coordinates of the element, while $\vec{x}_I$ represent coordinates of the eight nodes that constitute the element. And N_I is a shape function expressed as follows,

$$N_I = \frac{1}{8}(1 + \zeta\zeta_I)\ (1 + \eta\eta_I)\ (1 + \varsigma\varsigma_I) \ , \tag{3.42}$$

where ζ_I, η_I and ς_I take the value ± 1 according to the node number I in Figure 3.2.

Thus, the ALE coordinates in the referential domain can be expressed as follows,

$$\vec{\xi}(\vec{\zeta}) = \sum_{I=1}^{8} \vec{\xi}_I N_I(\vec{\zeta}) \ . \tag{3.43}$$

Next, based on Eq. 3.13, the material derivative of a physical variable g corresponding to the ALE description can be expressed as follows,

$$\frac{Dg}{Dt} = \sum_{I=1}^{8} \frac{dg_I(t)}{dt} N_I(\vec{\zeta}) + w(\vec{\zeta}, t)\vec{\nabla} N_I(\vec{\zeta}) g_I(t) \ . \tag{3.44}$$

The weak formulation of the momentum conservation equation Eq. 3.28

can be rewritten as follows,

$$
\begin{aligned}
&\boldsymbol{M}\frac{D\boldsymbol{v}}{Dt} + \boldsymbol{f_{int}} = \boldsymbol{f_{ext}} \\
&\text{with} \\
&\boldsymbol{M} = \boldsymbol{I}\left[\int_{\Omega_t^e} \rho N_I N_J \, d\Omega_t\right] = \boldsymbol{I}[\tilde{M}_{IJ}] \\
&\boldsymbol{f_{int}} = \left[\int_{\Omega_t^e} \frac{\partial N_I}{\partial x_j}\sigma_{ij} \, d\Omega_t\right] \\
&\boldsymbol{f_{ext}} = \left[\int_{\Omega_t^e} \rho N_I b_i \, d\Omega_t + \int_{\Gamma_t^e} N_I t_i \, d\Gamma_t^e\right] \\
&\boldsymbol{v} = [\vec{v}_J] \\
&\frac{D\boldsymbol{v}}{Dt} = \left[\frac{D\vec{v}_J}{Dt}\right] \ .
\end{aligned}
\tag{3.45}
$$

Thus, from the momentum conservation equation, the nodal acceleration can be obtained and expressed as follows,

$$
\begin{aligned}
&\dot{a}_{iI}^n = \frac{(f_{iI}^{ext})^n - (f_{iI}^{int})^n}{\tilde{M}_{II}} \\
&\text{with} \\
&\tilde{M}_{II} = \frac{1}{8}\rho Vol(\Omega_t^e) \ ,
\end{aligned}
\tag{3.46}
$$

where $Vol(\Omega_t^e)$ represents the volume of an element Ω_t^e.

The nodal velocity can be expressed as follows,

$$
v_{iI}^{n+1/2} = v_{iI}^{n-1/2} + \dot{a}_{iI}^n \Delta t \ . \tag{3.47}
$$

Similarly, the displacement can be expressed as follows,

$$
x_{iI}^{n+1} = v_{iI}^{n-1} + v_{iI}^{n+1/2} \Delta t \ . \tag{3.48}
$$

Internal energy and pressure

The calculation of internal energy is based on the integration with a quadrature point at center of the element. This allows for the simplification of weak formulation of the energy conservation equation Eq. 3.38, with variables ρ, stress σ_{ij}, strain rate d_{ij} and the test function δe are constants in the element Ω_t^e. Then, the simplified equation can be expressed as follows,

$$\delta e \rho \frac{De}{Dt} V = \delta e d_{ij} \sigma_{ij} V + \delta e \rho \vec{g} \vec{\vec{v}}^e V \ , \tag{3.49}$$

where $V = Vol(\Omega_t^e) = \int_{\Omega_t^e} \ d\Omega_t$, and $\vec{\vec{v}}^e V = \int_{\Omega_t^e} \vec{v} \ d\Omega_t$. The term $\vec{g}$ represents the gravity with $\vec{g} = \vec{b}$.

In fact, δe is an arbitrary test function that allows reducing the body force b_i to zero. Therefore, the energy conservation equation is further reduced as follows,

$$\rho \frac{De}{Dt} V = d_{ij} \sigma_{ij} V \ . \tag{3.50}$$

By dividing the stress tensor and strain rate tensor into its spherical part ($\sigma_{ij}^{'}, d_{ij}^{'}$) and deviatoric part($1/3\sigma_{ii}, 1/3d_{ii}$). Without considering the shock viscosity, Eq. 3.50 can be rewritten as follows,

$$\rho \frac{De}{Dt} V = \left(\frac{1}{3} d_{kk} \delta_{ij} + d_{ij}^{'} \right) \left(\sigma_{ij}^{'} - P \delta_{ij} \right) V \ . \tag{3.51}$$

With trace of the volume strain rate equal to $\Delta V / V \Delta t$, and the total internal energy of the element as $E_e = \rho e V$, a central finite difference scheme can be

applied to above equation and expressed as follows,

$$
\begin{aligned}
&E_e^{n+1} = E_e^n + \Delta t \; \sigma_{ij}^{'\,n+1/2} \; d_{ij}^{'\,n+1/2} \; V^{n+1/2} - P^{n+1/2} \Delta V^{n+1/2} \\
&\text{with} \\
&\sigma_{ij}^{'\,n+1/2} = \frac{1}{2}(\sigma_{ij}^{'\,n} + \sigma_{ij}^{'\,n+1}) \\
&P_{ij}^{'\,n+1/2} = \frac{1}{2}(P_{ij}^{'\,n} + P_{ij}^{'\,n+1}) \; .
\end{aligned}
\tag{3.52}
$$

The relationship between internal energy and pressure makes the above equation implicit. The internal energy depends on the pressure at t^{n+1} and the pressure depends on the internal energy, which can be expressed as follows,

$$
P(E_e, \rho) = A_1(\rho) + A_2(\rho) \frac{E_e}{V} \; . \tag{3.53}
$$

The terms $A_1(\rho)$ and $A_2(\rho)$ are related to the material equation of state and can be expressed as follows,

$$
\begin{aligned}
A_1(\rho) &= C_0 + C_1 \mu + C_2 \mu^2 \\
A_2(\rho) &= C_3 + C_4 \mu + C_5 \mu^2 + C_6 \mu^3 \; ,
\end{aligned}
\tag{3.54}
$$

where C_i are constants corresponding to the material equation of state, and μ represents the relative rate of the volume fraction expressed as follows,

$$
\mu = \frac{\rho - \rho_{ref}}{\rho_{ref}} \; , \tag{3.55}
$$

where ρ_{ref} represents the reference density.

3.1.6 Advection algorithm

In the advection phase, the mesh needs to be repositioned again after undergoing distortion in the Lagrangian phase. This means that if the convective velocity $\vec{w}$ equals the material velocity $\vec{v}$, the mesh needs to return to its initial

position according to the Eulerian description; in the opposite case, the mesh will change again according to the convective velocity. And displacement of the grid is independent of the movement of fluids. Therefore, this remap step maps the physical variables obtained in the Lagrangian phase to the new mesh.

The remap process requires two assumptions. First, topology of the mesh should be fixed, then, the mesh motion during a step is less than the characteristic lengths of the surrounding elements. The latter can be described by a condition that the Courant number, C, should be less than or equal to 1, expressed as follows,

$$C = \frac{|\vec{w}|\Delta t}{L} \leq 1 \ , \tag{3.56}$$

where $|\vec{w}|\Delta t$ represents the volume transported between adjacent elements. And Δt is arbitrary because the mesh motion does not correspond to any physical time scale. Then, L represents a characteristic dimension of the mesh, so that this condition demands the displacement of the grid in a time step should be less than this length.

The transport volume computation is not associated with any of the calculation of physics variables. Therefore, a good advection algorithm should be accurate, stable, conservative and monotonic. Although some of the variables like the stress and plastic strain are not governed by momentum or energy conservation equations, it is desirable that the volume integral of all such variables remain unchanged by through the remap process. Then, the monotonicity requires that the range of the solution variables does not increase during the remap process. This is especially critical with mass and energy that negative values may lead to the instability and termination of the computation.

Commonly used advection algorithms include the Donor Cell algorithm and the Van Leer Monotone Upwind Schemes for Conservation Laws (MUSCL) algorithm. The former can be traced back to a difference scheme for the numerical solution of discontinuous solution of hydrodynamic equations proposed by Godunov [127]. The Donor Cell algorithm is a simple, stable, monotonic,

conservative and diffusive advection algorithm, but only with first order accuracy. The latter can be traced back to the work of Van Leer, where an approach to numerical convection that exclusively yields upstream-centered schemes is presented, some examples of second-order and third-order schemes are given, and the accuracy, monotonicity issues are discussed [128]. The MUSCL algorithm is a monotonic, conservative and dispersive advection algorithm, and with second order accuracy.

In presenting the advection algorithms, the simple Eulerian scenario is considered, that is, the case where the ALE grid velocity $\vec{v}$ equals zero and $J_{\hat{\Phi}} = 1$ in Eq. 3.39.

Donor Cell algorithm

Consider $f = g\vec{w}\Delta t$ with f representing a flux of a physical variable. That is, f represents the mass flux if g is the density, then, f the internal energy flux with g the volume internal energy, and f the momentum flux with g the momentum per unit volume. The Donor Cell algorithm for 1D advection is presented as follows,

$$
\begin{aligned}
& g_{j+1/2}^{n+1} = g_{j+1/2}^{n} + \frac{1}{\Delta x}(f_j - f_{j+1}) \\
& \text{with} \\
& f_j = \frac{1}{2} w_j \Delta t (g_{j-1/2}^{n} + g_{j+1/2}^{n}) + |w_j| \Delta t (g_{j-1/2}^{n} - g_{j+1/2}^{n}) \ .
\end{aligned}
\tag{3.57}
$$

In above equation, j represents a node, while $g_{j-1/2}^{n}$ and $g_{j+1/2}^{n}$ represent the values of corresponding physical variables g located at the left and right sides of the node, respectively.

Then, the value of f_j depends on the velocity w_j of the node j. If $w_j > 0$, $f_j = w_j g_{j-1/2}^{n} \Delta t = g_{j-1/2}^{n} V_j$, which means that the flux of g is shifting in the direction of the increase of the index j from left to right. Correspondingly, if $w_j < 0$, $f_j = w_j g_{j+1/2}^{n} \Delta t = g_{j+1/2}^{n} V_j$, which means that the flux of g is shifting in

the direction of the decrease of the index j, from right to left.

MUSCL algorithm

In the Donor Cell algorithm, the distribution of g is assumed to be constant over an element. However, the MUSCL algorithm replaces the piecewise constant distribution with a higher order interpolation function. The piecewise linear distribution can be expressed as follows,

$$g^n_{j+1/2}(x) = S^n_{j+1/2}(x - x^n_{j+1/2}) + g^n_{j+1/2} \ , \tag{3.58}$$

where x represents the coordinate inside the volume of an element, $x^n_{j+1/2}$ represents the center coordinate of the element mesh, and $S^n_{j+1/2}$ is the slope of the line formed by previous two coordinates.

For the monotonicity of the algorithm, the slope $S^n_{j+1/2}$ should respect the condition as follows,

$$\begin{aligned} &S^n_{j+1/2} = \frac{1}{2}\left(sgn(s^L) + sgn(s^R)\right) min(|s^L| \ , |s^n_{j+1/2}| \ , |s^R|) \\ &\text{with} \\ &s^L = \frac{1}{2\Delta x_{j+1/2}}(g^n_{j+1/2} - S^n_{j-1/2}) \\ &s^R = \frac{1}{2\Delta x_{j+1/2}}(g^n_{j+3/2} - S^n_{j+1/2}) \ , \end{aligned} \tag{3.59}$$

where sgn represents the sign function, and s^L and s^R are the slope limits respectively on the left and right of $s^n_{j+1/2}$.

In fact, $s^n_{j+1/2}$ is a second-order approximation of the slope calculated from a quadratic interpolation consisting of the values of the three adjacent elements

meshes with g as the center. The approximation can be expressed as follows,

$$s^n_{j+1/2} = \frac{(g^n_{j+3/2} - g^n_{j+1/2})\Delta x_j^2 + (g^n_{j+1/2} - g^n_{j-1/2})\Delta x_{j+1}^2}{\Delta x_{j+1}\Delta x_j(\Delta x_{j+1} + \Delta x_j)}$$
$$\text{with} \tag{3.60}$$
$$\Delta x_j = x^n_{j+1/2} - x^n_{j-1/2} \ .$$

The second approach is similar to Eq. 3.59, but with different slope limits, expressed as follows,

$$\begin{aligned} s^L &= \frac{g^n_{j+1/2} - g^n_{j-1/2}}{x_{j+1/2} - (x_j + \frac{1}{2}max(0, w_j)\Delta t)} \\ s^R &= \frac{g^n_{j+3/2} - g^n_{j+1/2}}{x_{j+1} - \frac{1}{2}min(0, w_{j+1}\Delta t) - x_{j+1/2}} \ . \end{aligned} \tag{3.61}$$

Then, the flux f_j at node j can be evaluated by a scheme similar to the Donor Cell method, expressed as follows,

$$f_j = \frac{1}{2}w_j(g_j^- + g_j^+)\Delta t + \frac{1}{2}|w_j|(g_j^- - g_j^+)\Delta t$$
$$\text{with}$$
$$\begin{aligned} g^- &= S^n_{j-1/2}(x^e - x^n_{j-1/2}) + g^n_{j-1/2} \\ g^+ &= S^n_{j+1/2}(x^e - x^n_{j+1/2}) + g^n_{j+1/2} \\ x^e &= x^n_j + \frac{1}{2}\Delta t w_j \ . \end{aligned} \tag{3.62}$$

Thus, the advection of the variable g can be expressed using the incoming and outgoing flux, as follows,

$$g^{n+1}_{j+1/2} = g^n_{j+1/2} + \frac{1}{\Delta x}(f_j - f_{j+1}) \ . \tag{3.63}$$

The MUSCL algorithm can be applied to all the element-centered physical variables obtained during the Lagrangian phase. And for node-centered velocity data, some modifications need to be applied.

Advection of the momentum

In commonly used algorithms, the velocity is centered at the nodes or the edges, and it is the momentum to be advected instead of the velocity, in order to ensure the conservation of momentum. The element-centered advection algorithms should be modified for the advection of node-centered momentum.

The advection of momentum can be achieved in two different approaches. First, it is possible to construct a new mesh so that nodes are located at the centers of the elements in the new mesh, and then element-centered advection algorithms can be applied. Another approach, by constructing a number of element-centered auxiliary variables from the momentum, and the advection is achieved by element-centered advection algorithms, then, the nodal velocity data can be computed from the auxiliary variables.

The Staggered mesh algorithm adopts the first approach. The YAQUI code proposed by Amsden and Hirt is the first code to compute fluid flow velocity by constructing a new mesh that is staggered with respect to the original mesh for the momentum advection [129]. With this method, the advection of momentum can be done with the transport volumes, the advection of velocity can be done with the mass. For the velocity advection through mass, it can be expressed as follows,

$$M_j^{'} v_j^{'} = M_j v_j + (\rho v)_{j-1/2}\, V_{j-1/2} - (\rho v)_{j+1/2}\, V_{j+1/2}\ , \tag{3.64}$$

where M_j represents the nodal mass of node j, and the index $'$ indicates the advected term.

For a 1D case with the length $\Delta x_{j\pm1/2}$, the nodal mass can be expressed as follows,

$$M_{j\pm1/2}^{'} = \rho_{j\pm1/2}\, V_{j\pm1/2}\ , \tag{3.65}$$

where $V_{j\pm1/2}$ represents the volume of the element mesh $j \pm 1/2$.

Then, advection of the nodal mass is interpolated based on the advected

masses, expressed as follows,

$$\begin{aligned} M_j^{'} &= \frac{M_{j+1/2}^{'} + M_{j-1/2}^{'}}{2} \\ &= \frac{1}{2}\left(M_{j+1/2} + (\rho V)_j - (\rho V)_{j+1} + M_{j-1/2}\right) + \frac{1}{2}\left((\rho V)_{j-1} - (\rho V)_j\right) \\ &= M_j + \frac{1}{2}((f_j - f_{j+1}) + (f_{j-1} - f_j)) \ . \end{aligned} \tag{3.66}$$

Another technique, the SALE Algorithm proposed by Amsden *et al.*, approximates the momentum at the center by taking the average of the neighbor nodal momentum [130]. Taking half of this quantity for each element sharing node j, we obtain the variation in momentum of this node can be expressed as follows,

$$M_j^{'} v_j^{'} = M_j v_j + \frac{1}{2}\left((\rho v)_{j-1}\, V_{j-1} - (\rho v)_{j+1}\, V_{j+1}\right) \ . \tag{3.67}$$

3.2 Interface Tracking Method

When dealing with multi-material scenarios, such as air-water in the water wave problem, where elements may contain multiple materials, the interface tracking is required as well as the free surface reconstruction for the visualization of simulation results in post-processing.

3.2.1 Multi-material formulation

In the simulation of FSI problems, the motion of material interfaces between different fluids and the structure also needs to be evaluated. Multiple materials may exist in an element at the same time, consider the volume fraction of a material in an element denoted as V_f^k with $k = 1, 2, 3, ...$ representing the amount of material, then $0 \leq V_f^k \leq 1$.

Benson described the mixture theory dealing with Eulerian multi-material models [131]. Different mixture theories differ in the way they deal with the

distribution of the strain rate between different materials. The average strain rate $\dot{\bar{\varepsilon}}$ of an element needs to meet the condition as follows,

$$\dot{\bar{\varepsilon}} = \sum_k \dot{\varepsilon}^k \; V_f^k \; , \tag{3.68}$$

where $\dot{\varepsilon}^k$ represents the strain rate of the material k.

The method presented here considers the pressure equalization between each material in the element. Then, an unknown equilibrium pressure p^{eq} is defined, and the pressure $p^k(\rho^k, e^k)$ calculated from the equation of state of each material should be equal to that equilibrium pressure, expressed as follows,

$$\begin{aligned} & p^{eq} = p^k(\rho^k, e^k) \; V_f^k \\ & p_i^k = p_j^k, (i \neq j) \\ & \text{with} \\ & \sum_k |V_f^k| = 1 \; . \end{aligned} \tag{3.69}$$

The calculation of volume fraction of the material in each element is implanted in the advection phase. Resolution of the volume fraction requires dealing with the nonlinear system of equations Eq. 3.69 for the number of materials. The variation of the volume fraction ΔV_f^k can be described by an iterative Newton-Raphson scheme, expressed as follows,

$$\Delta V_f^k = \frac{p^{eq} - p^k}{\partial p^k / \partial V_f^k} \; , \tag{3.70}$$

where the term $\partial p^k / \partial V_f^k$ is obtained based on the state equation.

With the additional condition $\sum_k (V_f^k + \Delta V_f^k) = 1$ on volume fraction, the

equilibrium pressure can be obtained and expressed as follows,

$$p^{eq} = \frac{1 + \sum_k \left(p^k / \frac{\partial p^k}{\partial V_f^k} - V_f^k \right)}{\sum_k 1 / \frac{\partial p^k}{\partial V_f^k}} \ . \tag{3.71}$$

3.2.2 Interface Tracing and Reconstruction

After acquiring the volume fraction data of materials in each element, it is possible to identify where the interfaces between different materials are located. Reconstruction of the interface is usually carried out using the VOF method. Discontinuous interface segments are constructed to approximate the real interface. And these interface segment are determined using the volume fraction information of a material in each element cell and its surrounding neighboring element cells.

A commonly used and effective method is the Young's method, Young proposed the interface reconstruction techniques for both 2D and 3D problems [132, 133]. After determining location of the interface segments, the material distribution is defined based on volume fraction of different materials in each element cell. And then, in each cell, interface segments are approximated by straight lines, thus reconstructing the entire free surface. This technique, also known as the Piecewise Linear Interface Construction (PLIC), is more accurate than Simple Line Interface Calculation (SLIC). And orientation of the interface can be fixed parallel or perpendicular to the advection direction.

First, the normal $\vec{n}$ of each interface segment can be determined through gradient of the volume fraction calculated from the adjacent element cells, expressed as follows,

$$\vec{n} = \frac{\vec{\nabla}(V_f)}{\|\vec{\nabla}(V_f)\|} \ . \tag{3.72}$$

Then, with volume fraction data of the material considered in an element cell, the projection distance $d = \vec{n} \cdot \vec{x}$ is adjusted to determine position of the interface segment in the element.

For a 2D problem with two fluids, the material interface segment in an element cell is calculated using volume fractions of that element and other 8 adjacent element cells. Taking a square region consisting of 9 element cells as an example, the center element is given with the coordinate $(i+1/2, j+1/2)$, then the volume fraction gradient of the center element can be expressed as follows,

$$\frac{\partial V_f}{\partial x} = \frac{V^*_{f\ (i+3/2,\ j+1/2)} - V^*_{f\ (i-1/2,\ j+1/2)}}{x_{(i+3/2,\ j+1/2)} - x_{(i-1/2,\ j+1/2)}}$$
$$\frac{\partial V_f}{\partial y} = \frac{V^*_{f\ (i+1/2,\ j+3/2)} - V^*_{f\ (i+1/2,\ j-1/2)}}{y_{(i+1/2,\ j+3/2)} - y_{(i+1/2,\ j-1/2)}}$$

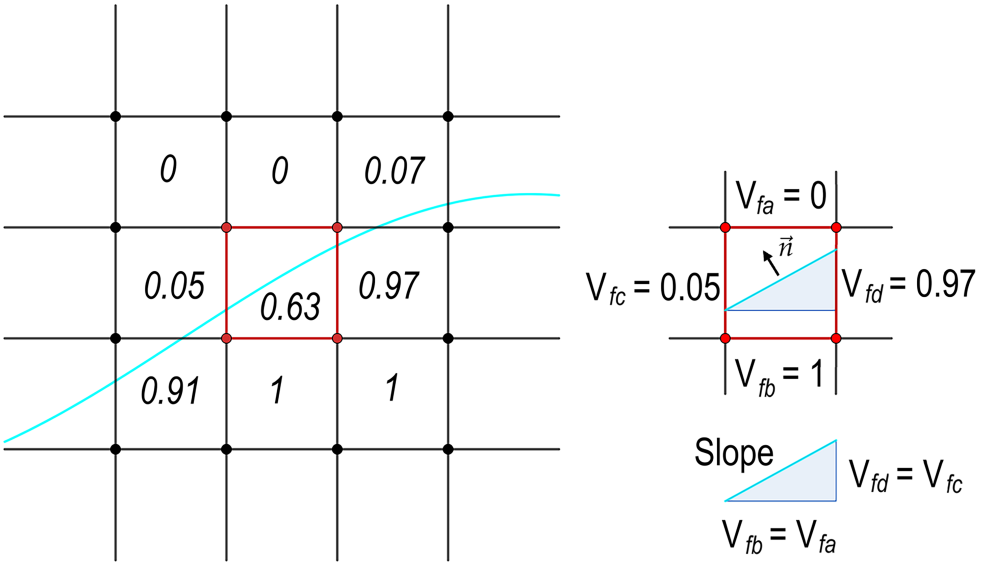
with

$$V^*_{f\ (i+3/2,\ j+1/2)} = \frac{V_{f\ (i+3/2,\ j-1/2)} + 2V_{f\ (i+3/2,\ j+1/2)} + V_{f\ (i+3/2,\ j+3/2)}}{4} \tag{3.73}$$
$$V^*_{f\ (i-1/2,\ j+1/2)} = \frac{V_{f\ (i-1/2,\ j-1/2)} + 2V_{f\ (i-1/2,\ j+1/2)} + V_{f\ (i-1/2,\ j+3/2)}}{4}$$
$$V^*_{f\ (i+1/2,\ j+3/2)} = \frac{V_{f\ (i-1/2,\ j+3/2)} + 2V_{f\ (i+1/2,\ j+3/2)} + V_{f\ (i+3/2,\ j+3/2)}}{4}$$
$$V^*_{f\ (i+1/2,\ j-1/2)} = \frac{V_{f\ (i-1/2,\ j-1/2)} + 2V_{f\ (i+1/2,\ j-1/2)} + V_{f\ (i+3/2,\ j-1/2)}}{4}\ .$$

Figure 3.3 illustrates the approximation of an interface segment through volume fraction data.

3.3 Coupling Algorithm Based on Penalty Method

An important objective of performing numerical simulations of the wave impact FSI problem is to evaluate the fluid forces acting on a rigid or deformable structure. And acquiring these force data requires the implantation of the coupling algorithm between fluid elements and structure elements in the ALE model. The coupling forces act at the interface between fluids and the structure. And the coupling algorithm needs to be capable of transferring the fluid pressure acting on the structure, as well as applying the velocity produced by the motion of the structure to the fluid.



(a) Real interface (b) Approximate interface

Figure 3.3: Interface Reconstruction

A fundamental approach to dealing with the interaction between fluids and the structure is the contact method. This method is used to solve the tracking and computation of moving interfaces in numerical methods for continuum mechanics. Bourago and Kukudzhanov conducted a literature review of different types of contact algorithms[134]. Wriggers presented contact modeling in the finite element method and discussed the situation regarding the presence of large deformations [135]. Zhong discussed about the finite element modeling of contact-impact problems, and the use of contact algorithms to compute the contact forces between the fluid and the structure was introduced [136]. In methods modeling the contact, the presence of a contact interface is used to separate the fluid mesh from the structure mesh. Since fluid nodes at the contact interface need to move to maintain the contact with the Lagrangian structure, a rezoning or automatic remesh method is required for the fluid domain in face of large deformations.

Another effective method for dealing with FSI problems is the Euler–Lagrange

coupling method. This approach combines the ALE multi-material formulation with a penalty-based contact method that is capable of avoiding fluid mesh distortion as well as handling the fluid impact problem. In Euler-Lagrange coupling, the Eulerian formulation is used for fluids and the Lagrangian formulation is used for structures, with the Eulerian grid overlapping the structure mesh. The Eulerian fixed grid contains the Lagrangian structure and the ALE fluids. Fluids flow through the mesh so that no mesh distortion occurs. Then, velocity and history variables are updated with an advection scheme. In addition, the penalty-based contact method can ensure the conservation of momentum and energy.

3.3.1 Contact Conditions

In the presence of contact between fluids and the structure, it is essential to first construct the contact condition for the interaction between those two bodies, that is, the condition of non-interpenetration.

Consider the fluid domain Ω^F with boundary Γ^F and normal $\vec{n}^F$, the structure domain Ω^S with boundary Γ^S and normal $\vec{n}^S$, and their interface is Γ^C. Naturally, the description of the interface can be expressed as follows,

$$\begin{aligned} &\Omega^F \cap \Omega^S = 0 \\ &\Gamma^F \cap \Gamma^S = \Gamma^C \\ &\vec{n}^S = -\vec{n}^F \ . \end{aligned} \tag{3.74}$$

For a fluid particle and a material particle of the structure located at the interface and in contact, the first condition of non-interpenetration can be described as follows,

$$\begin{aligned} \dot{d}_n(\vec{x},t) &= \vec{v}^S \cdot \vec{n}^S + \vec{v}^F \cdot \vec{n}^F \\ &= \vec{v}_n^S(\vec{x},t) - \vec{v}_n^F(\vec{x},t) \leq 0 \text{ with } \vec{x} \in \Gamma^C \ , \end{aligned} \tag{3.75}$$

where $\vec{v}_n^S$ and $\vec{v}_n^F$ represent respectively the projection of the fluid particles' ve-

locity and the structural material particles in normal direction of the interface Γ^C at $\vec{x}$. And d_n represents the distance of penetration between a fluid and the structure, thus, $\dot{d}_n$ represents the penetration rates.

The contact can be determined based on the value of $\dot{d}_n$, with positive and negative values representing the presence and absence of the penetration, respectively. Then, $\dot{d}_n = 0$ represents the continuity of normal velocities at the interface.

The second condition aims to describe the principle of reciprocity of a pair of forces at the interface from the fluid and the structure. Consider the traction vectors of the Cauchy stress for the fluid and the structure denoted as $\vec{t}^{\,F}$ and $\vec{t}^{\,S}$ respectively, then, the reciprocity gives $\vec{t}^{\,F} + \vec{t}^{\,S} = 0$. Their projections at the interface in the normal direction also satisfy this relation, with $t_n^F + t_n^S = 0$. Then, in the absence of adhesion between the fluid and structure surfaces in the normal direction,the condition of compression can be expressed as follows,

$$t_n \equiv t_n^S(\vec{x}, t) = -t_n^F(\vec{x}, t) \leq 0 \text{ with } \vec{x} \in \Gamma^c \ . \tag{3.76}$$

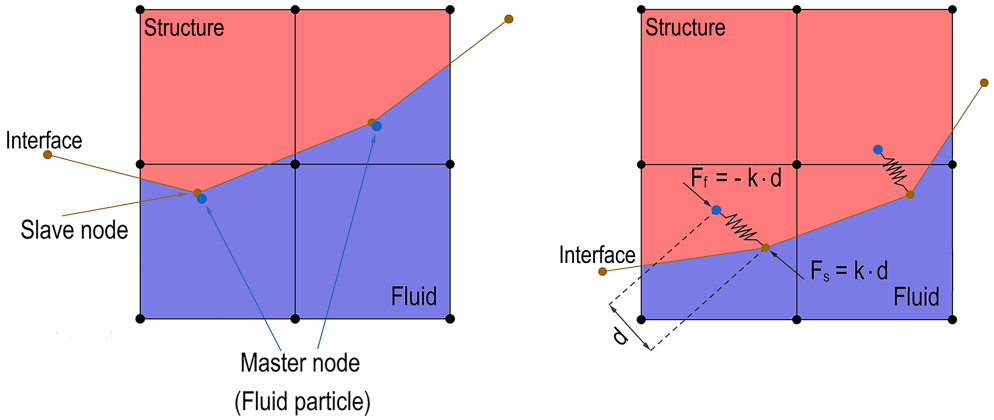
Then, from above equations, it is possible to derive the third condition that describes the relationship between the normal traction and the penetration rate, known as the unilateral contact condition, expressed as follows,

$$\dot{d}_n(\vec{x}, t)\ t_n(\vec{x}, t) = 0 \text{ with } \vec{x} \in \Gamma^C \ . \tag{3.77}$$

3.3.2 Coupling Forces Based on the Penalty Method

In the contact algorithm based on the penalty method, a master-slave description is used to define the fluid surface and the structure surface (or penetrating and reference surfaces) that will come into contact. And similarly, nodes or segments on the surface follow this same rule. In a FSI model, the Eulerian fluid is usually defined as the master part, while the structure of the Lagrangian

formulation is the slave part. The key concept of the penalty method is the implantation of a spring-like system where normal interface springs are placed between master nodes and slave nodes. Then, similar to the classical contact algorithm where the contact force is computed via a proportional function based on the penetration vector. Calculation of the contact force in the penalty method is based on the penetration depth and the spring stiffness. Figure 3.4 illustrates the coupling schema based on the penalty method.



(a) $t = t^0$ (b) $t = t^0 + \Delta t$

Figure 3.4: Penalty Coupling Schema

Calculation of the coupling force for the penalty method is as follows,

$$F = k \cdot d \ , \tag{3.78}$$

where k represents the spring stiffness and d represents the penetration depth.

And it should be pointed out that a pair of forces F_f and F_s is respectively imposed on the master and slave nodes in opposite directions, forming an equilibrium state at the coupling interface with $F_s = -F_f$. This is for the conformity with the fluid-structure interface condition previously mentioned as the reciprocity principle.

Then, for an explicit time integration scheme, the computed quantities within a single time step include the nodal forces of the fluid and the structure, as well

as the coupling forces between them. And the coupling forces affect only nodes located at the interface between the fluid and the structure. The penetration vector $\vec{d}$ is updated at each time step using the relative velocity $(\vec{v}_S - \vec{v}_F)$. Thus, the penetration vector is updated as follows,

$$\vec{d}^n = \vec{d}^{n-1} + (\vec{v}_S - \vec{v}_F)\Delta t \ . \tag{3.79}$$

The determination of the spring stiffness coefficient k is an important and difficult challenge in a coupling problem. This stiffness value depends on the problem to be studied and it needs to be obtained through a large number of experimental tests. A proper value of stiffness for the problem can reduce the energy interface for the total energy conservation and prevent the fluid from penetrating into the structure. The stiffness value k presented here will use the expression of stiffness in an explicit contact algorithm commonly used in fluid-structure interaction research, expressed as follows,

$$k = p_f \frac{KA^2}{V} \ , \tag{3.80}$$

where, for each placed spring, K is the bulk modulus of the coupling fluid element containing the structure slave node, V represents the volume of the fluid element containing the master fluid node and A represents the average area of structure elements connected to the structure node. Nevertheless, a scalar factor p_f is introduced in determining the stiffness, its value is specified in a range, $0 \leq p_f \leq 1$, in order to ensure numerical stability.

For impact events, it is possible that the coupling forces appear to be very large. This could lead to that the impact and the release occur at the same time step, thus distorting the simulation. A limit can be imposed on the coupling force, expressed as follows,

$$F \leq \frac{M_S M_F (\vec{v}_S - \vec{v}_F)}{(M_S + M_F)\Delta t} \ , \tag{3.81}$$

where M_S represents the mass of the structure node (slave) and M_F represents the mass of the fluid node (master) interpolated from fluid element nodes.

3.4 Conclusion

This chapter presented numerical methods used for the simulation of the wave impact FSI problem. In order to perform the simulation of water waves impacting on a structure, the ALE method can be used to compute the dynamic motions of fluids and the structure. Then, the interface tracking and reconstruction can be achieved through an approach using the material volume fraction data within each element cell. For the coupling between fluids and the structure, the Euler-Lagrange coupling method is applied, and the penalty method can be implanted to compute the coupling forces among the interface between fluids and the structure.

The ALE formulation combines advantages of the Lagrangian formulation and the Eulerian formulation, which allow for handling the presence of large material deformations. In addition to the material domain used to describe the structure and the spatial domain used to describe fluids, an arbitrary ALE referential domain is introduced (Figure 3.1). The Lagrangian formulation is used for structures and the Eulerian or ALE formulation is used for fluids. The NS governing equations used to describe fluids and their formulation under the ALE description are presented (Eq. 3.17, Eq. 3.18, Eq. 3.19). One of the main difficulties in solving the ALE NS equations remains the nonlinear advection terms containing convective velocity in the equations. In addition to solving the fully coupled NS equations directly, the split method is a commonly used and efficient resolution method. Computation is divided into Lagrangian phase and advection phase (Eq. 3.35, Eq. 3.36). The Lagrangian phase is performed using the FE method where nodal acceleration, nodal velocity, nodal displacement, internal energy as well as pressure are computed. During the advection

phase, a new mesh is generated based on the convective velocity and physical variables are remapped to the new mesh using an advection algorithm. The MUSCL advection algorithm with second-order accuracy is discussed, as well as algorithms for the advection of momentum.

The interface tracing and reconstruction are generally done using the VOF method. Multi-material formulations are discussed. Young's method based on the material volume fraction is presented (Figure 3.3).

For the coupling between fluids and the structure, the Euler-Lagrange coupling method is discussed. Contact conditions for the interaction between the fluid and the structure are presented. Then, the prediction of coupling forces based on the penalty method is discussed (Figure 3.4).

Chapter 4

Numerical Experiments of Water Waves and Wave–Structure Interaction

4.1 Wave Generation in a Numerical Wave Flume

LS-DYNA, Radioss, and OpenRadioss are all powerful solvers for simulating impacts and dynamic events. These solvers are embedded with the ALE formulation and the associated algorithms described in Chapter 3. Among them, OpenRadioss is a totally open source and user-friendly package. Therefore, OpenRadioss was selected for the main numerical experiments.

Numerical experiments are divided into two parts. In the first part, a numerical wave flume model is constructed according to the theoretical description in Chapter 2, and the generation of linear water waves is simulated. Then, generated water waves will be measured and compared to analytical solutions derived from the linear wave theory to verify the validity of the model. The second part performs simulations of water wave impacts on a structure using the ALE formu-

lation described in Chapter 3. A simple structure is coupled into the numerical wave flume to model the wave glider's float structure. Then, wave-structure interaction is investigated using water waves that have been validated in the first part. And the main focus is on wave loading at the wave-structure interface, as well as the posture changes of the structure subjected to wave impacts.

4.1.1 Wave Flume Configuration

The numerical wave flume here adopts linear water wave theory in order to target the generation of water waves for the typical operating sea states (up to sea state 4, Table 1.2) of the wave glider described in Chapter 1. For extreme sea states (above sea state 7), the solitary wave theory and associated wavemaker theory are required, which is not in the scope of numerical experiments here.

Dimensions of the numerical wave flume, mesh size, and the complexity of material models are major factors that determine the duration of computation. Simple models can be solved in minutes, while models with greater complexity may take days. Thus, constructing a suitable wave flume model helps to save computational resources. The constructed numerical wave flume is 30 m long, 5 m high and 0.2 m wide. The fluid domain consists of a water layer and an air layer, where the water depth is 3 m, and the air layer is 2 m. Fluids adopt the brick element, and an individual element is 0.1 m long, 0.1 m high, and 0.2 m wide. Because it is the regular waves of a single wave profile that are simulated, rather than superposed irregular waves or wave surface, maintaining only a single element in the width direction can economize computational resources. Thus, the total number of elements of the fluid domain is 15000. Disturbances are generated using a piston-type wavemaker, which is modeled as a paddle being positioned 5 m from the left boundary. Then respectively, on the left and right side of the water layer, a 2 m long damping zone is set up to suppress the reflection of water waves. Figure 4.1 illustrates the numerical wave flume with

damping zones.



Figure 4.1: Wave flume with damping zones

The water depth and the height of the air layer of the numerical wave flume are determined taking into account the wave height parameter of the target water waves as well as the intermediate water depth condition with respect to the target water waves. As for the length, the wavelength of the target water waves is considered and the observation of a complete wave profile is desirable.

Regarding the wavemaker, it adopts the shell element. In some applications solved with LS-DYNA, the paddle is placed at the left boundary and merged with the boundary nodes, as a technique to simplify the modeling. This modeling technique is difficult to perform when working with OpenRadioss. And if the paddle is too close to the boundary, the disturbances may cause anomalous motion of fluids. This phenomenon was observed in the preliminary phase of the simulation attempts. Therefore, a suitable paddle position needs to be determined.

Following the theoretical description in Chapter 2, the wavemaker is governed by a periodic reciprocal displacement motion Eq. 2.32, and water waves are generated from the disturbances created by the wavemaker. Due to the presence of a start-up hysteresis, water waves will stabilize some time after the start of the simulation and then become the target water waves that need to be measured.

4.1.2 Material Models

In terms of the selection of material models, a multi-material model is necessary due to the fact that the fluid domain consists of two fluids and their

presence together in a single element needs to be allowed. The OpenRadioss keyword $/MAT/LAW51$ allows the presence of materials with different laws, including elasto-plastic solid, liquid, gas and detonation products. Up to 4 different sub-materials are allowed. The admitted sub-materials include materials with $LWA3$, $LAW4$, $LAW5$, $LAW6$, $LAW10$ and $LAW102$. Then, the recommended equations of state (EOS) for materials include $/EOS/LINEAR$, $/EOS/POLYNOMIAL$, $/EOS/IDEAL-GAS$ and $/EOS/STIFF-GAS$.

For the constructed numerical wave flume model, material model of the water adopts the commonly used material law $LAW6$ for the description of fluids, and with the equation of state $/EOS/STIFF-GAS$. The density of water is set as $\rho = 1024\ kg/m^3$. The stiffed gas EOS is expressed as follows,

$$\begin{aligned} &P(\mu, E) = (\gamma - 1)\ (1 + \mu)E - \gamma P^* \\ &\text{with} \\ &E = \frac{E_{int}}{V_0} \\ &\mu = \frac{\rho}{\rho_0 - 1}\ , \end{aligned} \tag{4.1}$$

where γ is the heat capacity ratio, and P^* is an additional pressure term. And for water, $\gamma = 4.4$, $P^* = 56818181.82\ Pa$.

For air, its material model also adopts $LAW6$, but with a different EOS, the $/EOS/IDEAL-GAS/$. The ideal gas EOS is expressed as follows,

$$P = (\gamma - 1)\ (1 + \mu)E, \tag{4.2}$$

with $\gamma = 1.4$, $\rho = 1.22\ kg/m^3$.

For both water and air, the material flow is computed in ALE description.

As for the wavemaker, it is modeled as a rigid body represented by a mass point. Kinematic conditions can be imposed on this point to control the movement of the paddle for creating disturbances.

4.1.3 Analytical Target Waves

Regarding the dimension and water depth characteristics of the numerical wave flume, the approximate period range for generating effective waves from the constructed model is determined as $2\ s < T < 12\ s$. In order to observe a complete wave profile over the entire wavelength and to accurately measure wave parameters, four sets of target waves with different periods were selected. These waves have a wavelength not exceeding the available propagation distance of the wave flume. According to the Biésel transfer function Eq. 2.51 and for each set of waves, different stroke settings of the wavemaker are assigned to generate waves with different wave heights.

Period and stroke parameters for four selected sets of waves, as well as their corresponding analytical wavelength and wave height solutions, are given in Table 4.1.

Target wave	Period (s)	Stroke (m)	Analytical wavelength (m)	Analytical wave height (m)
E1	2.5	0.3	9.555	0.501
E2	2.5	0.5	9.555	0.835
E3	3.0	0.3	13.122	0.404
E4	3.0	0.5	13.122	0.674
E5	3.5	0.3	16.624	0.331
E6	3.5	0.5	16.624	0.551
E7	4.0	0.3	19.951	0.279
E8	4.0	0.5	19.951	0.465

Table 4.1: Target Wave Parameters and Analytical Solutions

Analytical solution of the free surface profile derived from the linear wave theory for the first set of target waves is shown in Figure 4.2, with a time point selected as $t = 10\ s$. And analytical solutions of free surface profiles for all four sets of target waves can be found in the Appendix A.

As mentioned in Chapter 2, the relative depth d/L, wave steepness H/L and relative wave height H/d are three important dimensionless parameters used for characterization of waves in the study of water wave problems. The

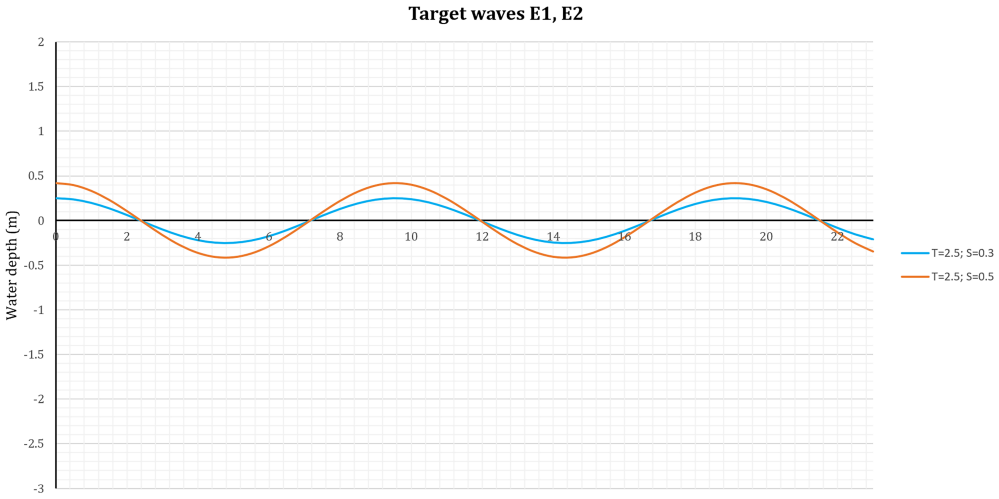


Figure 4.2: Analytical Wave Profiles of Target Waves E1, E2

relative depth, wave steepness and relative wave height parameters of the target waves are given in Table 4.2.

Target wave	Relative depth	Wave steepness	Relative wave height
E1	0.314	0.0524	0.167
E2	0.314	0.0873	0.278
E3	0.229	0.0308	0.134
E4	0.229	0.0513	0.224
E5	0.180	0.0199	0.111
E6	0.180	0.0331	0.184
E7	0.150	0.0140	0.093
E8	0.150	0.0233	0.155

Table 4.2: Relative Depth, Wave Steepness and Relative Wave Height of Target Waves

The wave steepness of target waves shown in Table 4.2 is small quantities, just as that the ratio of the wave height to the wavelength in linear wave theory is assumed to be small. And for relative depth, they settle into a range between $1/20-1/2$, this allows the target waves to be classified as an intermediate water depth condition as described in Table 2.1.

4.1.4 Simulation Results

For the numerical experiments of water wave generation, the OpenRadioss engine of a double precision version is used. The hardware configuration used for computation is shown in Figure 4.3.

```
NUMBER OF SPMD DOMAINS           1
NUMBER OF THREADS PER DOMAIN    48
NUMBER OF HMPP PROCESSES        48

COMPUTATION HARDWARE DESCRIPTION

HOSTNAME     CPU TYPE, FREQUENCY AND MEMORY
lamba   Intel(R) Xeon(R) w7-3455 (x86_64),  796 MHz, 128038 MB RAM,   2047 MB swap

STACKSIZE  . . . . . . . . . . . . . . . . . . . . . 8 MB
THREAD STACKSIZE . . . . . . . . . . . . . . . . . . 400 mB
```

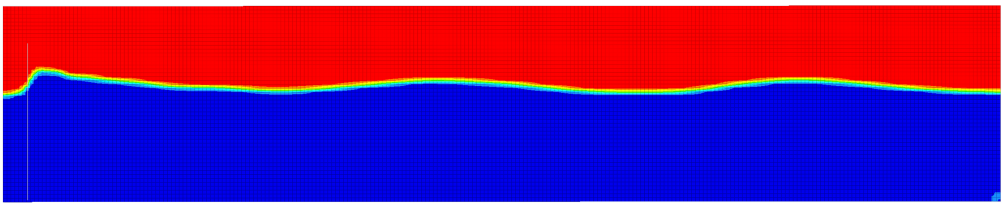
Figure 4.3: Computation Hardware Description

In order to save computation time, the number of threads for computation is set to the maximum number allowed by the processor, 48 threads.

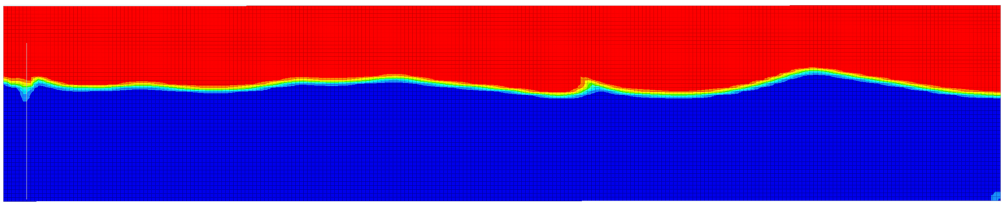
Experimental attempts are first conducted with no damping zone set up, and then, four sets of target water waves are simulated with the damping zones. The total simulation time is set to 30 s. After solving by OpenRadioss, the generated animation files can be post-processed by HyperView or converted to ".vtk" format for visualization by Paraview.

In the absence of damping zones, water wave starts to stabilize at about $t = 5\ s$ under the disturbances generated by the wavemaker. Water waves are reflected when they reach the right boundary, and a standing wave formed by the incident and reflected waves is observed at about $t = 12\ s$. The standing wave phenomena became more evident after about $t = 15\ s$ and a certain perturbation is produced against the incident wave. Figure 4.4 illustrates the stabilized water wave at $t = 10.4\ s$ and the disturbed water wave at $t = 20\ s$, where the standing wave and wave perturbation are observed.

Then, water waves are generated in the presence of damping zones. Similarly, water waves are stabilized after a period of time from the beginning of the simulation, and the damping zones on the left and right sides effectively reduce



a) Stabilized water wave



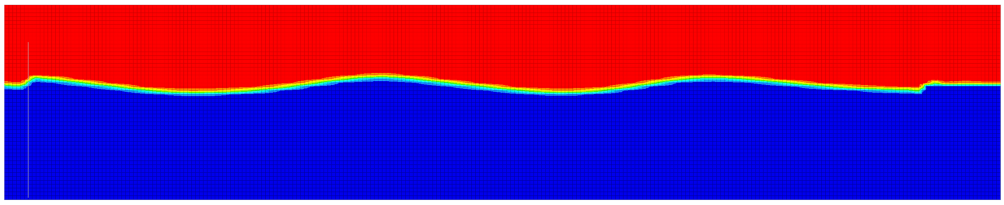
b) Disturbed water wave

Figure 4.4: Wave Generation Without Damping Zone

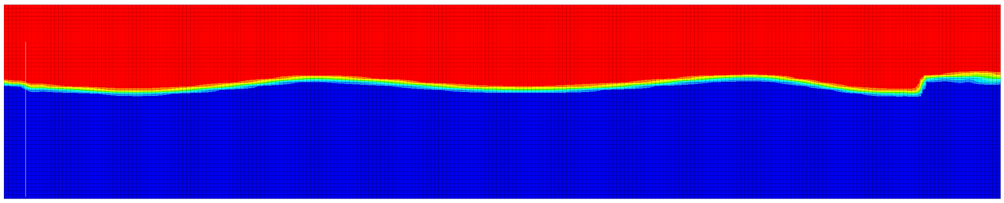
the reflection of water waves. Figure 4.5 illustrates the wave profile of the target water wave $E1$ at $t = 10\ s$ and $t = 17\ s$, where no significant standing wave phenomenon is observed.

Next, the effect of introducing damping zones on the absorption of water waves and the suppression of wave reflections is further verified by comparing the velocity of water particles located in different areas. Five nodes are selected and their velocity history data in the Y-direction is compared to verify the damping effect. Nodes A and B are a pair of neighbor nodes, while A is in the left damping zone and B is off the left damping zone. Same for nodes D and E, another pair of neighbor nodes that are separated by the interface between the normal water region and the right damping zone. While node D is located at the entering side of the right damping zone, and node E represents water particles that have just entered the right damping zone. Apart from this, a node C in the propagation region is also selected as a reference. The Figure 4.6 below shows the velocity data of selected nodes in Y-direction, velocity data of normal and damping nodes (node A, B, D, E) are also compared.

As shown, nodes B, C and D represent normally propagating water parti-

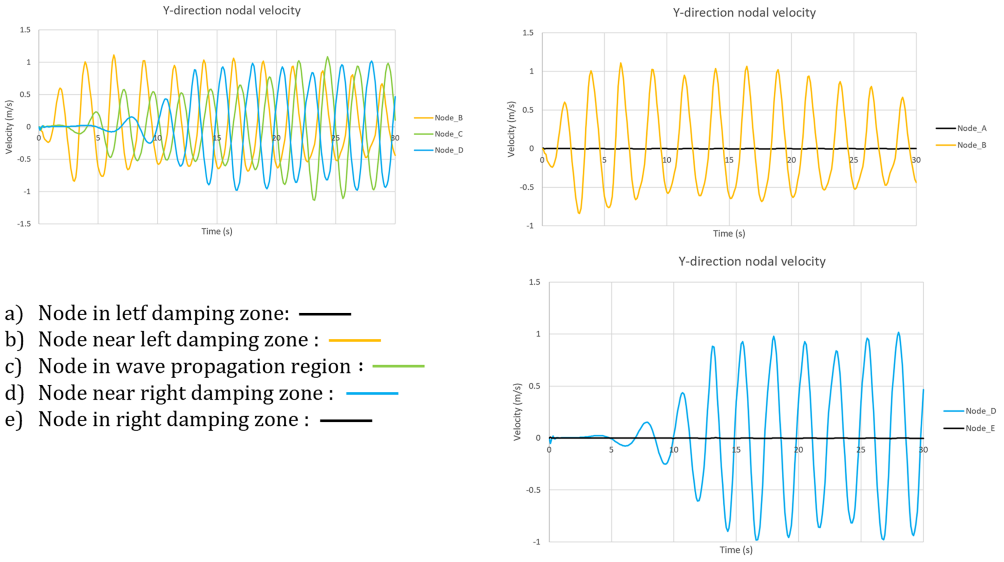


a) E1 at t = 10 s



b) E1 at t = 17 s

Figure 4.5: Simulated Target Wave E1 With Damping Zones



a) Node in letf damping zone:
b) Node near left damping zone :
c) Node in wave propagation region :
d) Node near right damping zone :
e) Node in right damping zone :

Figure 4.6: Comparison of Normal and Damping Nodal Velocities

cles that have almost similar velocity data. As for node A and node E, which are in damping zones, the damping effect dissipates the energy of water wave, resulting in a drastic reduction of the water particle velocity in Y-direction. And no significant standing wave phenomenon is observed. Incorporation of the damping zones effectively suppress the effect of wave reflection on the target waves.

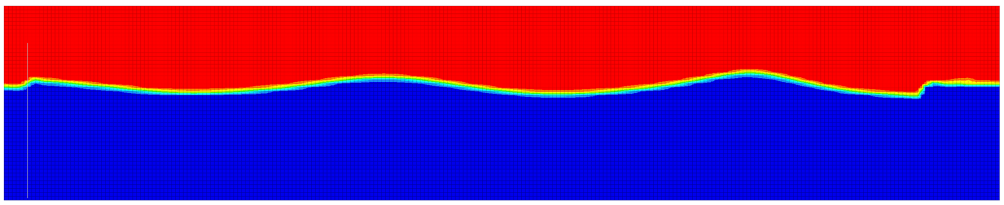
It is worth noting that seeking a good damping effect to absorb water waves requires a suitable damping coefficient. An inappropriate damping coefficient may lead to a low level of wave absorption or solid like behave of the damped water zone, thus enhancing the reflections, associated phenomenon was observed in the preliminary attempts of numerical experiments. In the water wave generation problem, the mass-weighted damping that is appropriate for the low-frequency cases possesses better effect. When it comes to determination of the damping coefficient, a reference frequency value is first obtained by analyzing the displacement data of water particles, and then this value is calibrated based on the damping efficiency in numerical experiments.

Then, all 4 sets of target water waves were simulated. Figure 4.7 illustrates wave profiles of the first set of target water waves $E1$, $E2$ at $t = 12.5\ s$, which are with the same period and different strokes. The complete wave profiles of $E1$ and $E2$ can be observed in the numerical wave flume, as well as the similarity and difference between $E1$ and $E2$ in terms of wavelength and wave height. This also made it easier to measure the parameters of all target water waves.

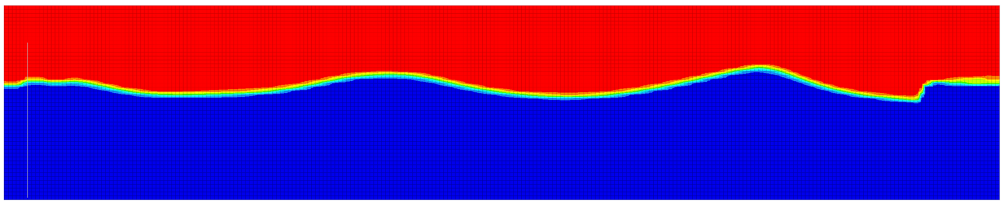
All 4 sets of simulated target water waves can also be found in the Appendix B.

4.1.5 Results Analysis

Firstly, in order to verify the accuracy of simulated water waves, parameters of generated target waves were measured and compared with their corresponding analytical solutions. During the measurement process, three time stops are



a) E1 at t = 12.5 s



b) E2 at t = 12.5 s

Figure 4.7: Simulated Target Waves E1, E2

selected, of which the water wave profiles are considered to be stabilized. Then, main parameters are measured and their average value is taken as the reference value of simulated target water waves. With the measured wavelength and wave height data, error rate is calculated by referring to target water wave parameters of their analytical solutions. The errors of the numerical wave flume model in generating effective waves with respect to the theoretical values were derived as follows in Table 4.3.

Target wave	Measured wavelength[1] (m)	Error rate[2] $(\%)$	Measured wave height[1](m)	Error rate[2] $(\%)$
E1	9.525	2.379	0.496	5.456
E2	9.337	2.282	0.880	5.389
E3	12.885	3.252	0.387	4.332
E4	12.913	1.595	0.645	5.638
E5	16.335	1.738	0.348	5.740
E6	16.531	0.559	0.524	4.900
E7	19.727	1.123	0.298	6.631
E8	19.738	1.068	0.495	6.452

[1] The value of measured wavelength and measured wave height are averaged over three measurements after the wave has stabilized.
[2] The error rate is an average value over three measurements.

Table 4.3: Simulated Wave Parameters and Errors

The error rate in wavelength of target waves is basically maintained at a level of less than 3.3 $\%$. The errors in wave height were more noteworthy, fluctuating between 4.3 $\% - 6.5$ $\%$. The simulated target waves are considered acceptable and have met theoretical expectations.

In addition to the evaluation of water wave parameters, computational resources are also investigated. All simulations of water wave generation are performed under the same hardware conditions using the same acceleration settings. The time duration used for simulations, the number of cycles of computation, and the percentage of the ALE computation are shown in Table 4.4.

Target wave	Computation duration (s)	Number of cycles	ALE computation (%)
E1 (non-damping)	1496.53	259160	49.23
E2 (non-damping)	1455.16	258693	50.40
E1	2512.67	464439	48.17
E2	2525.58	463997	48.37
E3	2511.57	464391	48.94
E4	2514.84	463858	47.99
E5	2516.46	464305	48.51
E6	2487.41	464075	49.26
E7	2538.49	464254	49.23
E8	2516.29	463798	49.36

Table 4.4: Statistics on Computation Resources (Wave Generation)

It can be noticed that if there is no increase in the complexity of the model, and only parameters are adjusted, the duration of computation as well as the number of cycles are very close to each other. Conversely, an increase in complexity, such as the inclusion of damping zones, will cost more computational resources. In the cases of target waves $E1$ $E2$ with and without damping zones, the computation time increases by about 67 $\%$ and 73 $\%$, respectively, and the corresponding number of cycles increases by about 79 $\%$. As for the proportion of corresponding ALE computation, it is maintained at a level that is not too high, because the water wave generation is mainly about the computation of the fluid motion and does not include additional Lagrangian structure.

4.2 Simulation of Wave–Structure Interaction

After verifying the accuracy of simulated water waves, FSI simulations can be launched with a structure coupled into the numerical wave flume model. The interaction between water waves and a floating structure was investigated using the same four sets of water waves. One of the focuses is the evaluation of wave loads at the wave-structure interface, and this loading data can support the study of fatigue behavior of composite hulls subjected to dynamic water wave impacts over long periods of time. The posture variation of the structure subjected to water wave impacts is then discussed. It has certain reference value for studying the change of incident water wave angle of the wave glider's float or other surface vehicles such as "AutoNaut" under the influence of wave impacts.

4.2.1 Coupling Structure in the Wave Flume

In this part, a structure of 2 m in length, 1.2 m in height and 0.2 m in width was placed at a distance of 20 m from the initial position of the paddle. The structure adopts the brick element with a total number of 240 elements, it maintains the same dimensions as the fluid element, which is 0.1 m in length, 0.1 m in height and 0.2 m in width. The consistency between structure element and fluid element does not complicate the computation. One third of the structure is immersed in water, and the translation in the X-direction and Y-direction along with the rotation in the Z-direction are kept free, in order to simulate a floating structure on the water surface. Figure 4.8 illustrates the numerical wave flume into which the structure is coupled.

The location of the structure is chosen to ensure that the water wave travels a certain distance and stabilizes before impact. It is desirable that a complete wave profile is formed and then impacts occur. In the numerical wave flume model, the left damping zone is maintained. And since it is difficult to use the



Figure 4.8: Wave Flume Coupled With Structure

damping effect to eliminate the reflection of waves upon contact with the structure, the damping zone on the right side is not preserved. The active water wave absorption method described in Chapter 2 is effective, that is, adjusting the motion of the wavemaker according to measured water wave parameters, thereby eliminating the effect of reflected waves. However, the active method is difficult to implement in this model, so it is not considered. Therefore, the first 20 seconds of the simulation were selected for the FSI experiments to ensure that the effect of water wave reflection is acceptable.

In order to simulate the composite hull as well as possible, the density of the structure was set to be roughly as same as a common glass/epoxy composite material, with $\rho = 1980\ kg/m^3$, but still modeled as a rigid body.

Then, structure adopts the Lagrangian formulation, fluids adopt the ALE formulation, with the Eulerian grid overlapping the structure mesh. And the MUSCL algorithm with second-order accuracy is used for the advection phase, as described in Chapter 3.

4.2.2 Simulation Results

The hardware configuration used for FSI simulations is the same as in the previous water wave generation simulations, shown in Figure 4.3.

A phenomenon is observed during the preliminary experimental attempts. That is, since the structure is initially set to be partially submerged in water, if the weight of the structure does not match the buoyancy of the structure, the structure may sink or float completely on the water surface at the beginning of the simulation. In the latter case, water wave disturbances will produce that

affect the incident wave profile. This requires adapting the mass of the structure to the situation. In order to eliminate this effect, parameters of the structure are adjusted so that the submerged depth is coincident with the depth of draft caused by the weight of the structure. Thus, at the beginning of the simulation, the structure is stationary in the water without causing disturbed water waves. It is worth noting that this phenomenon is not obvious when using the other solver.

Figure 4.9 illustrates the scene of impacts on the structure caused by target water waves $E1$, $E2$ at $t = 12.7\ s$. The simulation results are post-processed through Paraview in order to display more clearly the posture of the structure. Impact scenes for all four sets of target water waves can be found in the Appendix C.



a) Impact E1 at t = 12.7 s



b) Impact E2 at t = 12.7 s

Figure 4.9: Wave Impacts From Target waves E1, E2

Similarly, computational resources like the time duration, the number of cycles of computation and the percentage of the ALE computation used for the FSI simulations are investigated, shown in Table 4.5.

Compared with simulations of water wave generation, both the time duration and the total number of cycles are significantly increased, by an average of 266 $\%$ and 180 $\%$ respectively. And for the ALE computation, while the pro-

Target wave	Computation duration (s)	Number of cycles	ALE computation (%)
E1 (non-accelerated)	42229.22	1298377	90.50
E1	9123.26	1298377	38.09
E2	9145.16	1297636	38.13
E3	9114.62	1298489	38.34
E4	9125.83	1298349	38.10
E5	9205.46	1305021	37.84
E6	9235.61	1305504	37.68
E7	9343.72	1300580	32.46
E8	9363.45	1307179	33.26

Table 4.5: Statistics on Computation Resources (FSI)

portion decreased relatively, the time spent still increased by an average of 138 $\%$. In contrast, for an unaccelerated computation using only a single thread, the computation time spent is 4.6 times that of the accelerated computation for the same number of total cycles. Accordingly, ALE computation time accounts for as much as 90.5 $\%$ of total duration.

4.2.3 Water Wave Impact Loads

In order to compute the coupling forces at the fluid-structure interface, the interface setting of $/INTER/TYPE18$ is established between the left face of the Lagrangian structure, which is expected to be impacted, and fluid elements. This type of interface manages indirect coupling between ALE elements and Lagrangian structure for FSI applications, and the penalty method is used for the computation which requires the important stiffness coefficient and gap value.

Then, the coupling force data has been collected at the fluid-structure interface. Figure 4.10 illustrates nodes located on the fluid-structure interface.

Normal contact pressure in the X-direction and Y-direction are computed at the impact interface. The Figure 4.11 and Figure 4.12 below present respectively the historical pressure data in the X-direction and Y-direction generated by the target wave $E1$. Due to geometric symmetry, the figure shows only pressure data on one side. It is important to note that the nodes $Node - 31347$,

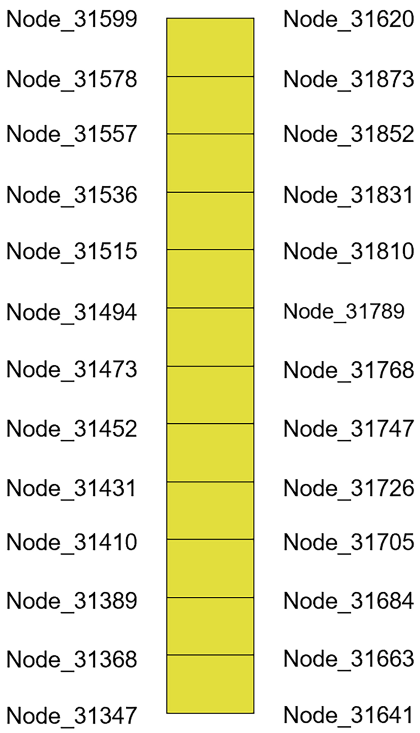


Figure 4.10: Nodes on the Fluid-Structure Interface

$Node-31368$, $Node-31389$ and $Node-31410$ are initially submerged in water, and nodes above the node $Node-31431$ can be considered to be above the still water level.

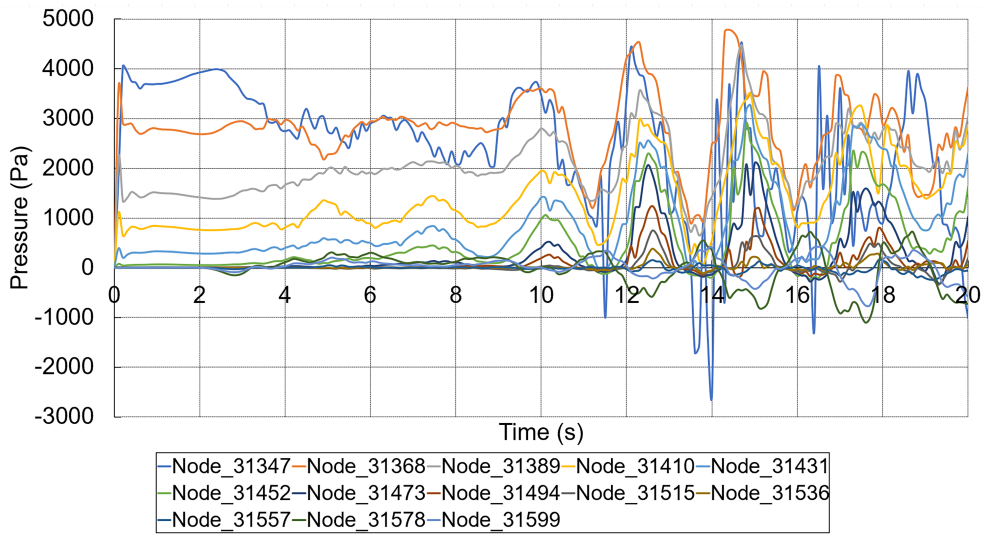


Figure 4.11: X-Direction Pressure Data From Impact E1

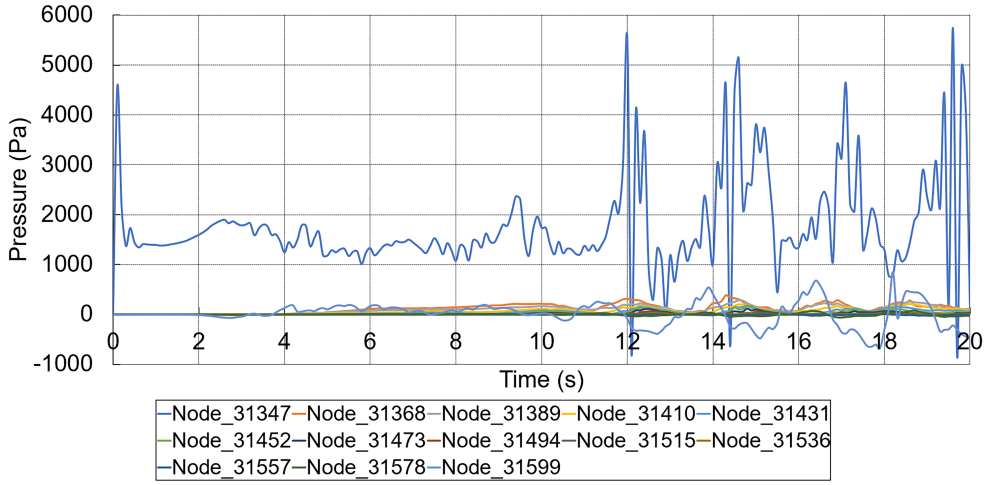


Figure 4.12: Y-Direction Pressure Data From Impact E1

Taking example of the bottom node $Node-31347$ and a node that is initially in a position above the free surface $Node-31452$, different phases of the impact can be easily distinguished based on the pressure data. The bottom node, as

it is submerged in water, undergoes a rapid initial hydrostatic pressure phase at the beginning of the simulation, with pressure values that correspond to the draft depth of the structure. Then, the wavemaker starts creating disturbances and the generated waves get gradually stabilized, which can be noted as the wave generation and stabilization phase. Next, the impacts follow, the structure experienced a total of four impacts in the simulated time. In contrast, hydrostatic pressure initialization is not required for nodes located above the free surface, which undergoes the same four impacts after that waves have stabilized. Taking the X-direction pressure data from the water wave $E1$, different impact phases of these two nodes are respectively indicated in the Figure 4.13 and Figure 4.14.

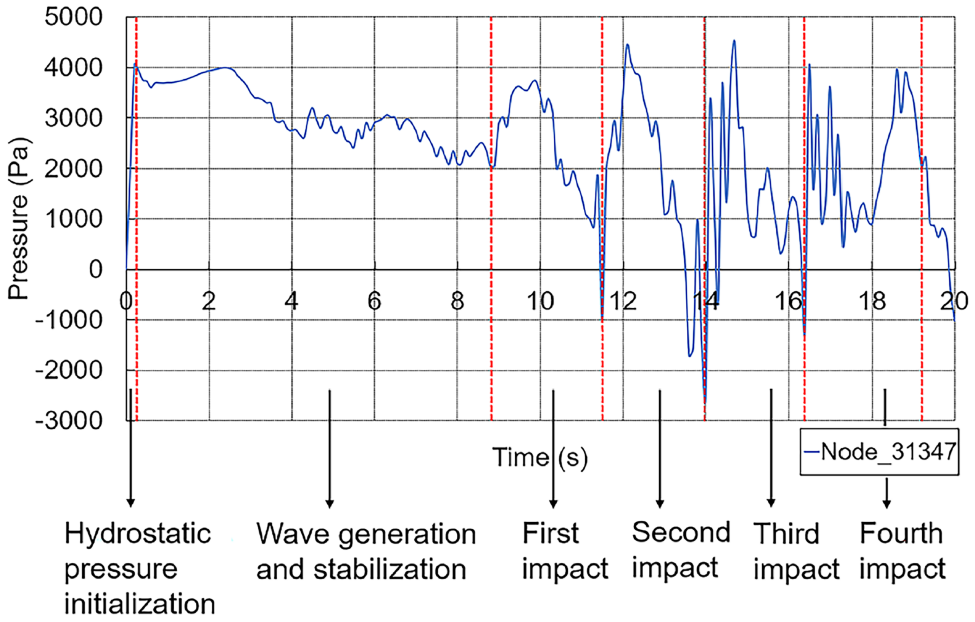


Figure 4.13: Impact Phase Analysis of Node-31347

According to mechanical characteristics of the structure, peak value of the impact pressure in the X-direction is 4783.337 Pa on $Node - 31368$. And in the Y-direction, only the bottom node $Node - 31347$ is subjected to high pressure loads, the peak value is 5741.385 Pa. This is due to the posture changes of the structure. In contrast to the average wave height of 0.496 m for the wave $E1$,

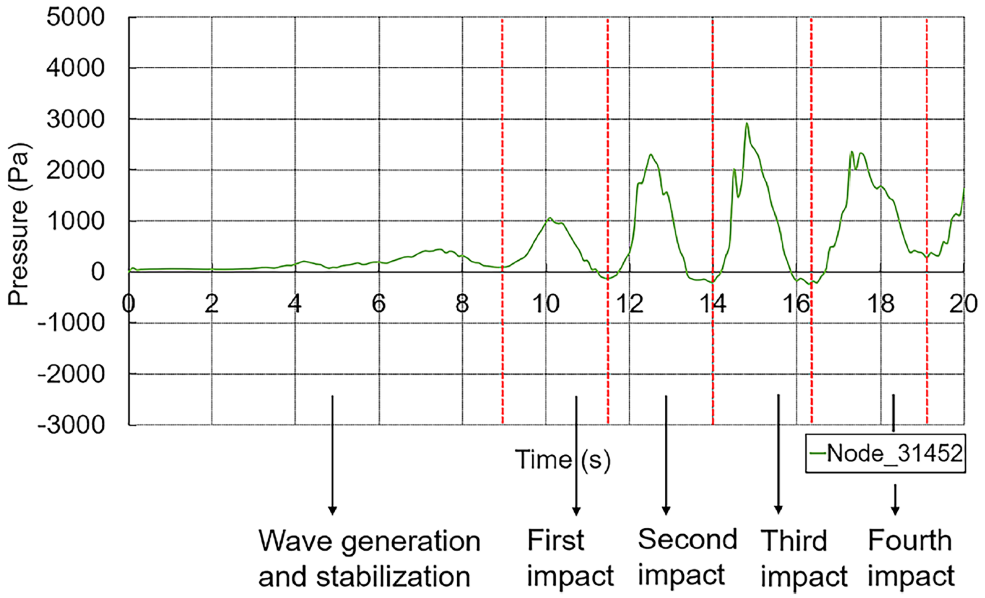


Figure 4.14: Impact Phase Analysis of Node-31452

the measured average wave height for the wave $E2$ is 0.880 m. Therefore, peak value of the impact pressure in the X-direction of the wave $E2$ is 6091.363 Pa on $Node - 31368$, and the peak value of the impact pressure in the Y-direction is 9122.550 Pa, always on the bottom node $Node - 31347$.

The Figure 4.15 and Figure 4.16 below present respectively the pressure data in the X-direction and Y-direction related to the wave $E2$.

The pressure data resulting from the impact of all four sets of water waves are compared and the node at the interface subjected to the greatest pressure is identified. These nodes and their corresponding X-direction and Y-direction pressure data are given in Table 4.6 below.

The impact pressure data of all four sets of target water waves can be found in the Appendix D.

Cross comparing these data, in this case of a floating and movable structure, wave loads are not only affected by the wave height, longer wavelength does not result in higher waves loads due to less water flows in a longer period. Of course, effect of the wave height is obvious, as a major factor affecting

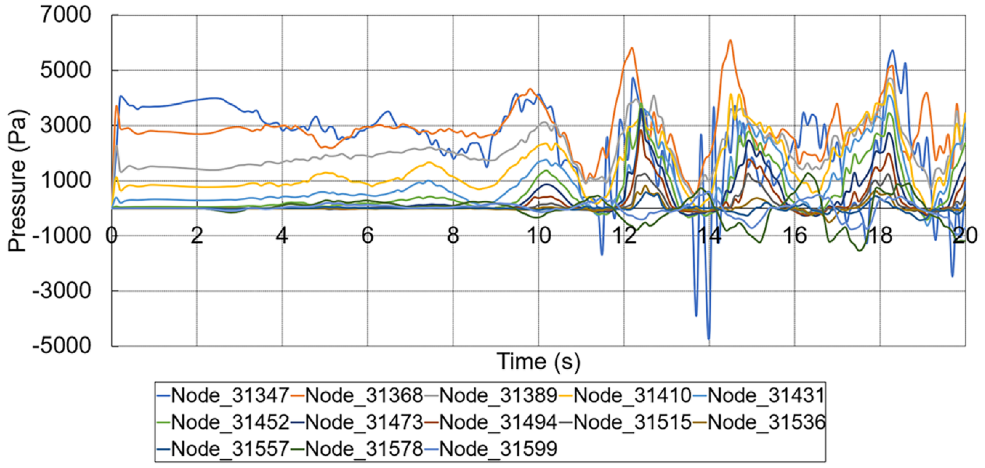


Figure 4.15: X-Direction Pressure Data From Impact E2

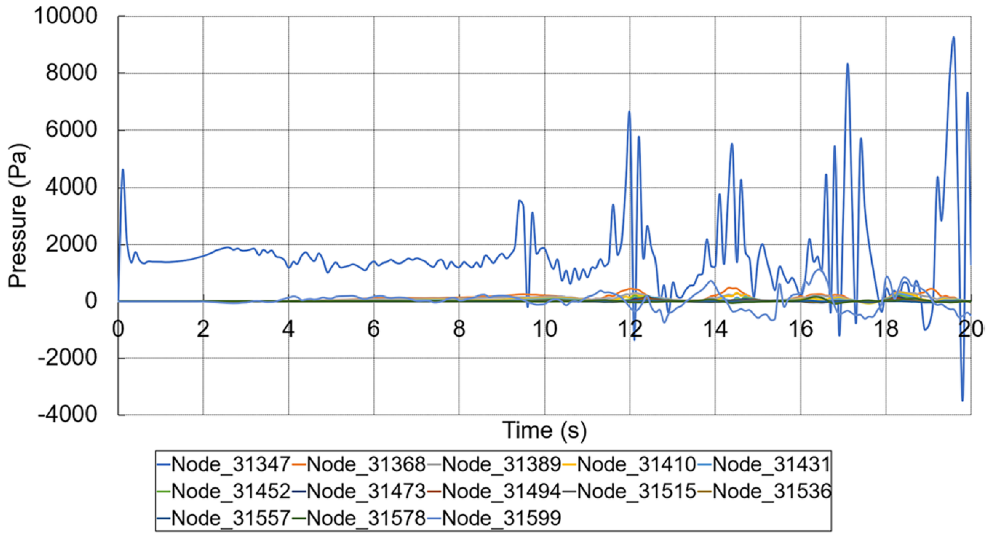


Figure 4.16: Y-Direction Pressure Data From Impact E2

Target wave	Node ID	X-direction max pressure (Pa)	Node ID	Y-direction max pressure (Pa)
E1	31368	4783.337	31347	5741.385
E2	31368	6091.363	31347	9122.550
E3	31368	4240.591	31347	4682.842
E4	31368	4455.750	31347	7751.569
E5	31368	4367.170	31347	4651.974
E6	31368	4252.086	31347	4611.549
E7	31368	4278.448	31347	4070.435
E8	31368	4313.105	31347	4608.937

Table 4.6: Max Normal Pressure Data on Fluid-Structure Interface

the wave loads than the wavelength. In maritime navigation safety, significant wave height is an essential parameter in defining the sea state, with higher wave heights signifying rougher conditions.

For the evaluation of wave loads based on the penalty method, it is crucial to determine an appropriate stiffness coefficient between the target structure and fluids. Typically, the stiffness coefficient can be determined by physical experiments, or can be calibrated by comparing analytic solutions derived through empirical equations of wave loads calculation. In addition to these two approaches, two basic thinking about searching for the stiffness coefficient are proposed during the numerical experiments. The following two criteria are used to determine the stiffness factor value:

- less possible penetration of the fluid into the structure;
- consistency between the hydrostatic pressure on the bottom node of the structure and its draft depth.

And these two criteria are respected by all impact simulations.

4.2.4 Structure Posture Analysis

When free the translation and rotation constraints of the structure, it is possible to move to another application scenario, the dynamic motion analysis of a

floating platform on the water surface subjected to wave impacts. Taking the target wave $E2$ as an example, the angular posture changes of the structure over a cycle are recorded. Before the wave stabilizes, the structure is pushed away in the X direction, and it will start a periodic oscillation when waves are stabilized. The Figure 4.17 below illustrates postures of the structure in one cycle due to wave impact, with only the structure part preserved for a clear observation.

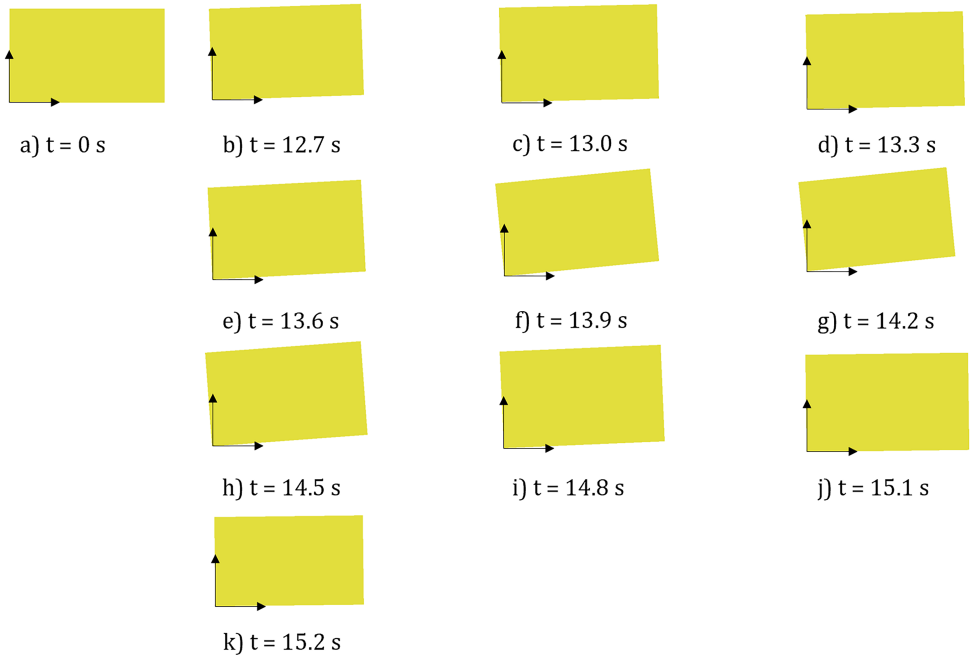


Figure 4.17: Structure Motion Subjected to Impact E2

It can be observed that the structure periodically oscillates along with the motion trajectory of water particles. A maximum angular change along the Z-direction throughout the impact is recorded as 5.715 °. Posture changes such as the angular variation can be treated as important study parameters when confronted with research problems such as seakeeping, landing and takeoff of seaplanes, and hydrofoil structures that utilize wave motion energy.

4.3 Conclusion

This chapter presents the construction of a numerical wave flume model and the associated setups. Simulation results of water wave generation and wave-structure interaction are analyzed. Based on the linear wave theory and wavemaker theory described in Chapter 2, and the description of the ALE method in Chapter 3, a piston-type numerical wave flume model is constructed. Then, models are solved using OpenRadioss. The numerical wave flume is first applied for experiments on water wave generation, and then the simulation of water waves impacting a structure is carried out after verifying the accuracy of generated water waves.

In the part of wave generation, the damping zone for water wave absorption is included on the left and right sides of the numerical wave flume. According to dimensions of the numerical wave flume, parameters of the aimed wave conditions and the transfer function equation, four sets of target water waves are set up. A simulation without water wave absorption is presented to illustrate the necessity of the damping zone. Water particle velocity data in different regions is compared to verify the effect of water wave absorption in damped zones. For generated water waves, error rates during numerical experiments are calculated by comparing with analytical wave profile solutions of target waves derived from the linear wave theory. The wavelength error is less than 3.3 $\%$ and the wave height error is between 4.3 $\% - 6.5$ $\%$, within an acceptable range. The computational resources for water wave generation simulations are also briefly analyzed.

For the simulation of wave-structure interaction, a simple structure is coupled into the numerical wave flume to simulate a floating structure on the water surface. The structure is parameterized with an usual glass/epoxy laminate material, but is still modeled as a rigid body. Considering that reflections from the generated water waves in contact with the structure are unavoidable, only the damping zone on the left side was retained. Then, impact of water waves on

the structure is simulated using the same four sets of target water waves. Simulated impact scenes are presented as well as computational resource statistics for corresponding experiments. In FSI simulations, the actual time duration of the ALE computation is significantly increased. Coupling forces at the wave-structure interface are collected by sensors set up at the interface. Normal contact pressure data based on the interface nodes in the X-direction and Y-direction is presented in the scenario of impacts by water waves $E1$ and $E2$. The impact processes of nodes located underwater and above the still water level are analyzed. Nodes at the interface that are most affected by the impact and associated pressure values are identified. Wave loading data obtained from the simulations can be used as a reference to study the mechanical responses as well as the fatigue behavior of the composite hull of the wave glider under dynamic impacts of water waves in its general operating sea state conditions over a long period of time. In numerical simulation experiments, two considerations for determining the stiffness coefficient in the penalty method are presented. At the end, dynamic motion of the structure under impacts of the target water wave $E2$ is analyzed.

In general, the numerical experiments are successfully performed using the ALE method for the simulation of water wave generation and wave-structure interaction. But the insufficiencies also need to be brought out. First, the linear wave theory used is a fundamental water wave theory, while other theories such as Stokes's wave theory are much closer to the real water wave conditions. Moreover, general CFD solvers use the NS equations as the governing equations for describing the fluid, and in some numerical experimental cases, water wave behavior, which may be a nonlinear phenomenon, is still observed. For the wave glider, the linear wave theory can be used to simulate the sea state under the proposed working conditions, and for the extreme sea state, it is necessary to apply wave theories for solitary waves or focused waves. Furthermore, more supports are needed for the validation of wave loading data, such as comparing physical experimental data with existing research results. For the

evaluation of the structure's behavior, it is preferable to adopt a more complex composite model with failure criteria.

Nevertheless, the constructed numerical wave flume model as well as the FSI model have shown the potential to be extended to more complex theoretical applications. Wave impact scenarios like the simulation of green water and slamming wave impacts are possible. Meanwhile, numerical simulations in this study have proven to be an economical, efficient, and scientifically valuable approach for approximating the physical investigation of the wave impact problem.

Appendix A

Analytical Wave Profiles of Target waves

For target waves $E1$ and $E2$ with the period $T = 2.5\ s$ and stroke $S_{E1} = 0.3\ m, S_{E2} = 0.5\ m$, the analytical solution of the free surface profile is shown in Figure A.1 (Figure 4.2 in Chapter 4), with a time point selected as $t = 10\ s$.

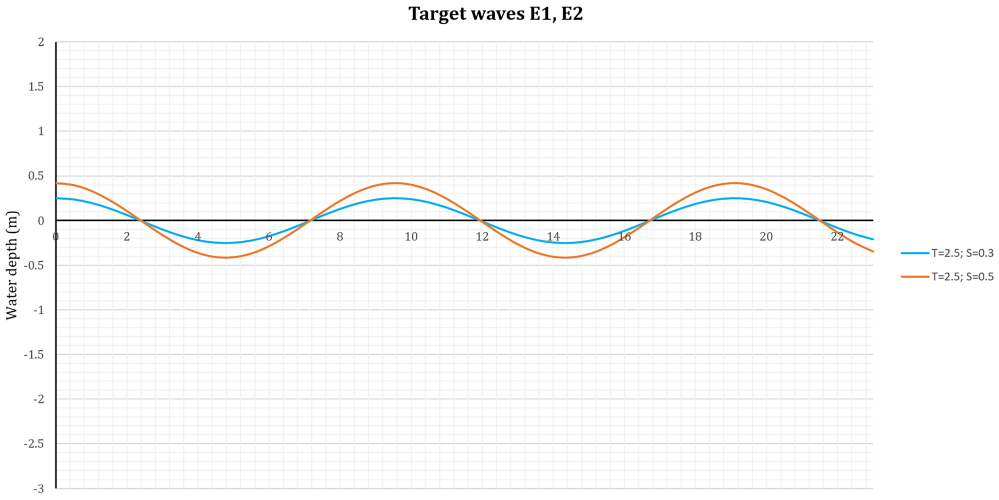


Figure A.1: Analytical Wave Profiles of Target Waves E1, E2

For target waves $E3$ and $E4$ with the period $T = 3\ s$ and stroke $S_{E3} = 0.3\ m, S_{E4} = 0.5\ m$, the analytical solution of the free surface profile is shown in

Figure A.2, with a time point selected as $t = 10\ s$.

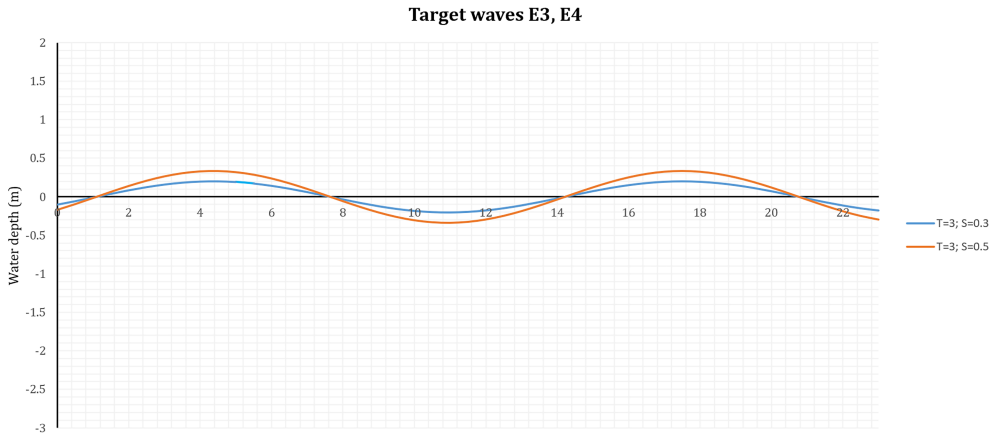


Figure A.2: Analytical Wave Profiles of Target Waves E3, E4

For target waves $E5$ and $E6$ with the period $T = 3.5\ s$ and stroke $S_{E5} = 0.3\ m, S_{E6} = 0.5\ m$, the analytical solution of the free surface profile is shown in Figure A.3, with a time point selected as $t = 10\ s$.



Figure A.3: Analytical Wave Profiles of Target Waves E5, E6

For target waves $E7$ and $E8$ with the period $T = 4\ s$ and stroke $S_{E7} = 0.3\ m, S_{E8} = 0.5\ m$, the analytical solution of the free surface profile is shown in Figure A.4, with a time point selected as $t = 10\ s$.

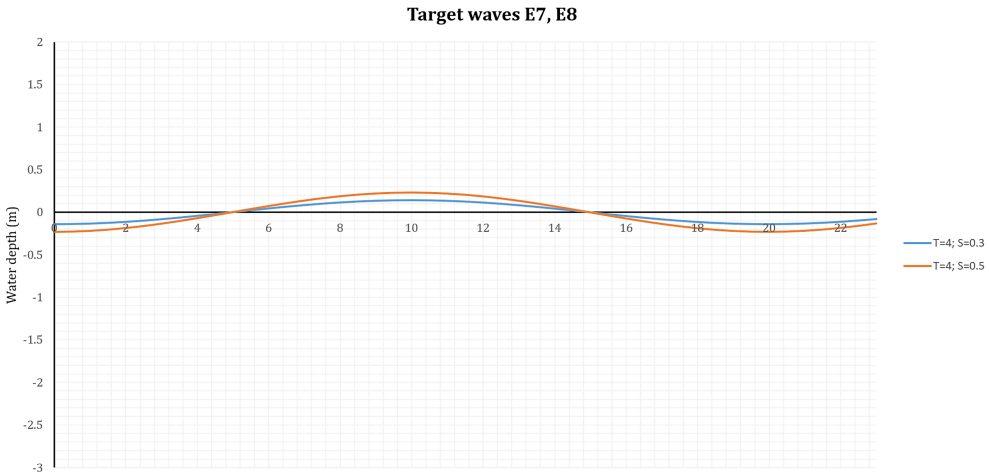
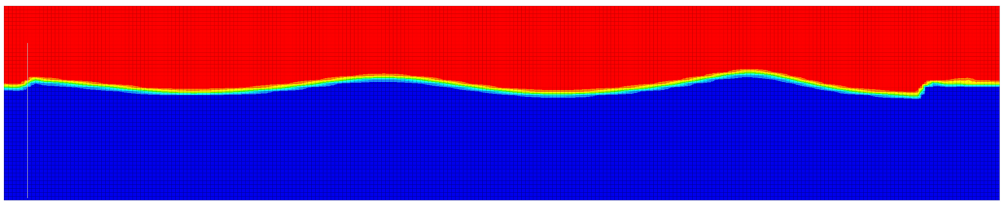


Figure A.4: Analytical Wave Profiles of Target Waves E7, E8

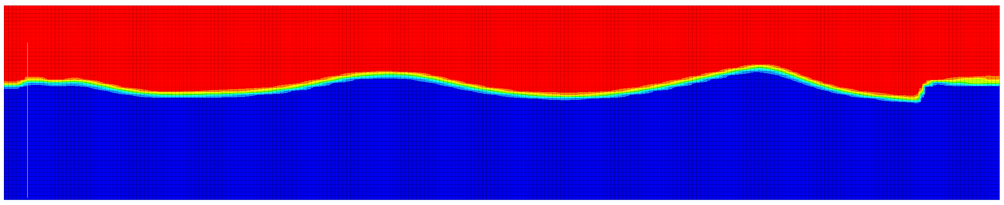
Appendix B

Simulated Target Waves

For target waves $E1$ and $E2$ with the period $T = 2.5\ s$ and stroke $S_{E1} = 0.3\ m, S_{E2} = 0.5\ m$, the simulated wave profile is shown in Figure B.1 (Figure 4.7 in Chapter 4), with a time point selected as $t = 12.5\ s$.



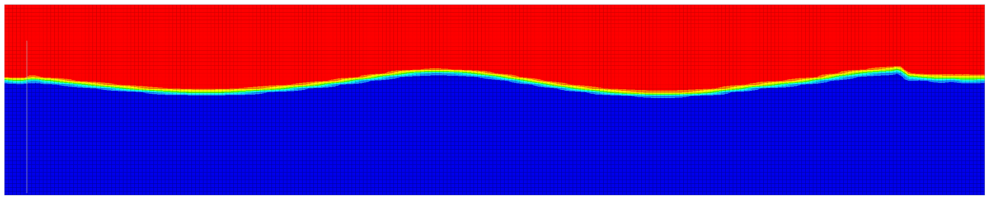
a) E1 at t = 12.5 s



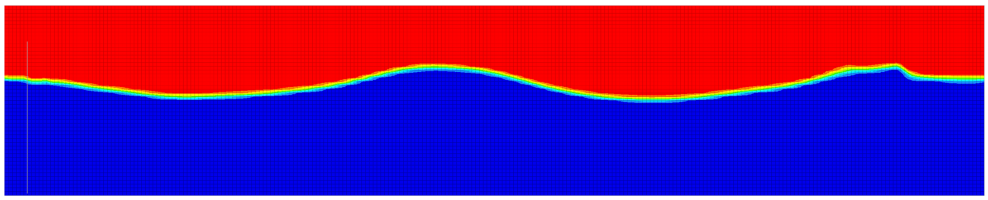
b) E2 at t = 12.5 s

Figure B.1: Simulated Target Waves E1, E2

For target waves $E3$ and $E4$ with the period $T = 3\ s$ and stroke $S_{E3} = 0.3\ m, S_{E4} = 0.5\ m$, the simulated wave profile is shown in Figure B.2, with a time point selected as $t = 17.5\ s$.



c) E3 at t = 17.5 s

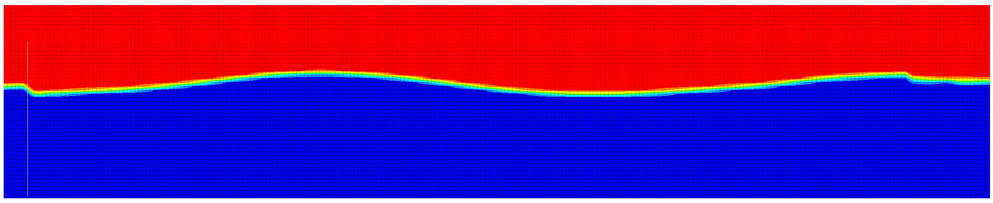


d) E4 at t = 17.5 s

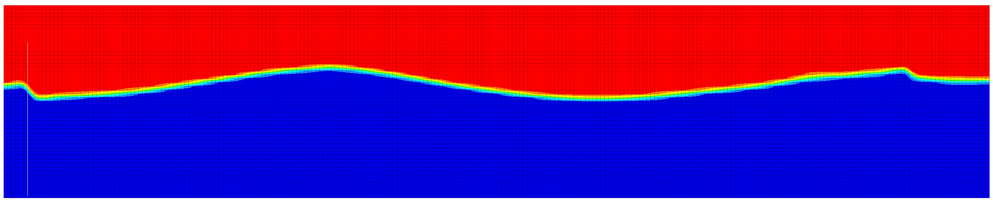
Figure B.2: Simulated Target Waves E3, E4

For target waves $E5$ and $E6$ with the period $T = 3.5\ s$ and stroke $S_{E5} = 0.3\ m, S_{E6} = 0.5\ m$, the simulated wave profile is shown in Figure B.3, with a time point selected as $t = 15.7\ s$.

For target waves $E7$ and $E8$ with the period $T = 4\ s$ and stroke $S_{E7} = 0.3\ m, S_{E8} = 0.5\ m$, the simulated wave profile is shown in Figure B.4, with a time point selected as $t = 6.3\ s$.

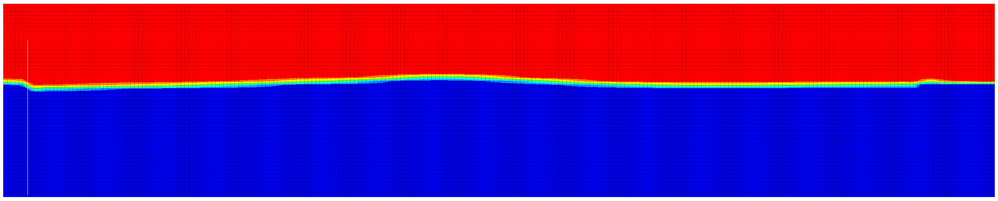


e) E5 at t = 15.7 s

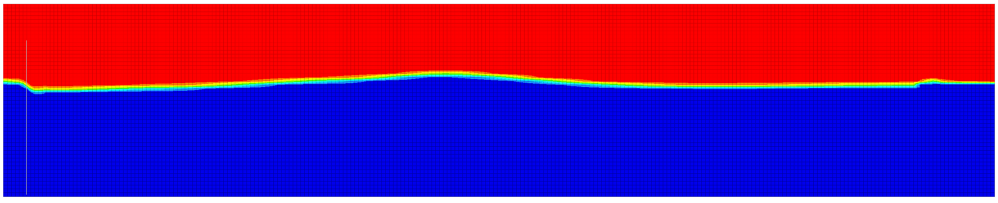


f) E6 at t = 15.7 s

Figure B.3: Simulated Target Waves E5, E6



g) E7 at t = 6.3 s



h) E8 at t = 6.3 s

Figure B.4: Simulated Target Waves E7, E8

Appendix C

Simulated Wave-Structure Interaction

For the wave-structure interaction simulation, the scene of the impact of the target water waves $E1$, $E2$ on the structure at $t = 12.7\ s$ is shown in Figure C.1 (Figure 4.9 in Chapter 4).



a) Impact E1 at t = 12.7 s



b) Impact E2 at t = 12.7 s

Figure C.1: Wave Impacts From Target waves E1, E2

For the wave-structure interaction simulation, the scene of the impact of the

target water waves $E3$, $E4$ on the structure at $t = 10.6\ s$ is shown in Figure C.2.



c) Impact E3 at t = 10.6 s



d) Impact E4 at t = 10.6 s

Figure C.2: Wave Impacts From Target waves E3, E4

For the wave-structure interaction simulation, the scene of the impact of the target water waves $E5$, $E6$ on the structure at $t = 10.9\ s$ is shown in Figure C.3.

For the wave-structure interaction simulation, the scene of the impact of the target water waves $E7$, $E8$ on the structure at $t = 7.9\ s$ is shown in Figure C.4.



e) Impact E5 at t = 10.9 s



f) Impact E6 at t = 10.9 s

Figure C.3: Wave Impacts From Target waves E5, E6



g) Impact E7 at t = 7.9 s



h) Impact E8 at t = 7.9 s

Figure C.4: Wave Impacts From Target waves E7, E8

Appendix D

Impact Pressure Data

For the wave-structure interaction simulation, the X-direction pressure data on the interface of the target water waves $E1$ and the structure is shown in Figure D.1 (Figure 4.11 in Chapter 4).

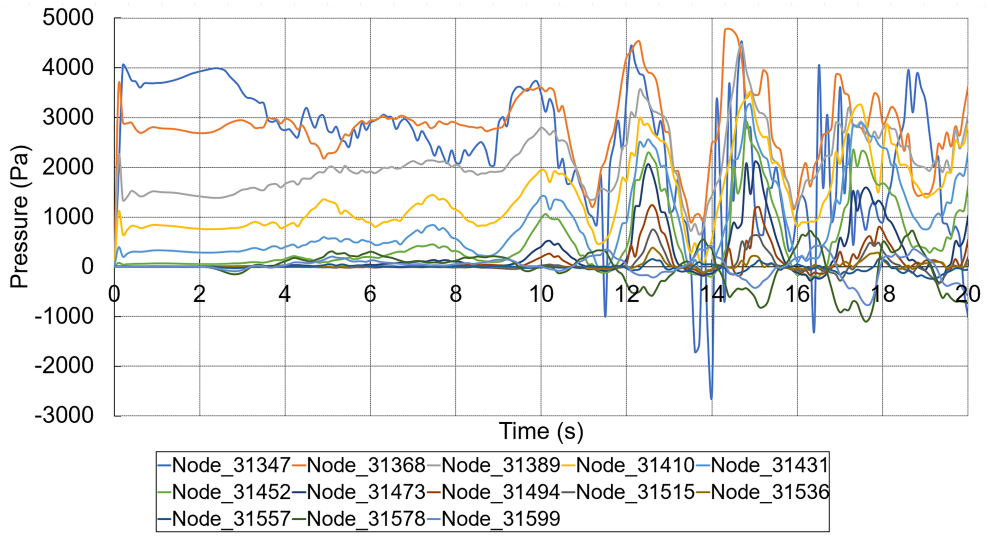


Figure D.1: X-Direction Pressure Data From Impact E1

For the wave-structure interaction simulation, the Y-direction pressure data on the interface of the target water waves $E1$ and the structure is shown in Figure D.2 (Figure 4.12 in Chapter 4).

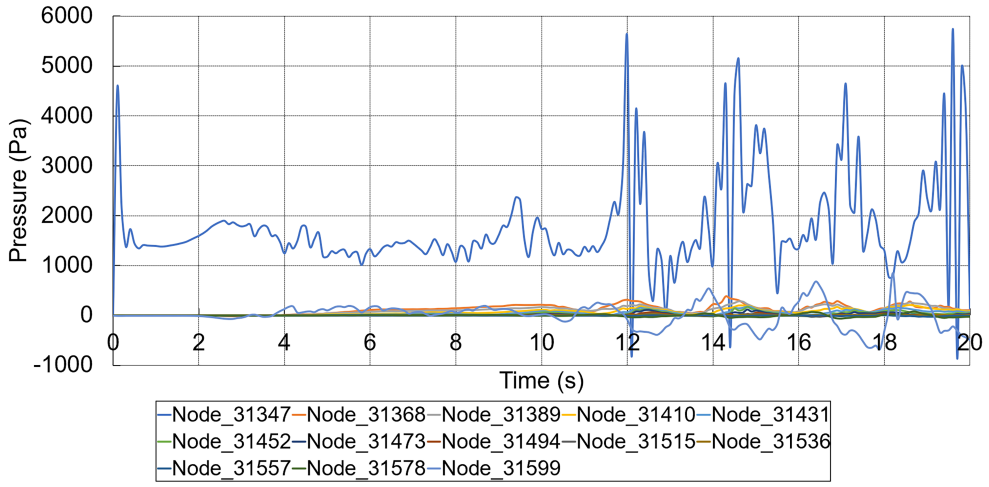


Figure D.2: Y-Direction Pressure Data From Impact E1

For the wave-structure interaction simulation, the X-direction pressure data on the interface of the target water waves $E2$ and the structure is shown in Figure D.3 (Figure 4.15 in Chapter 4).

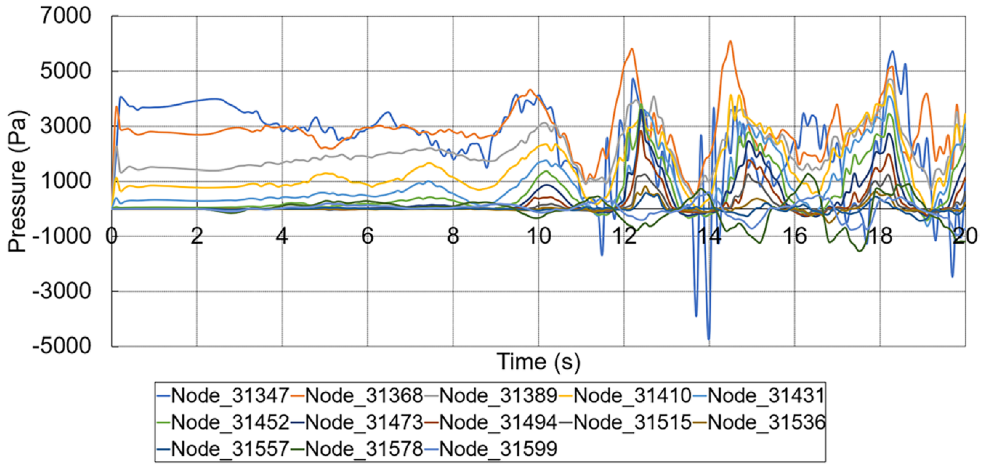


Figure D.3: X-Direction Pressure Data From Impact E2

For the wave-structure interaction simulation, the Y-direction pressure data on the interface of the target water waves $E2$ and the structure is shown in Figure D.4 (Figure 4.16 in Chapter 4).

For the wave-structure interaction simulation, the X-direction pressure data

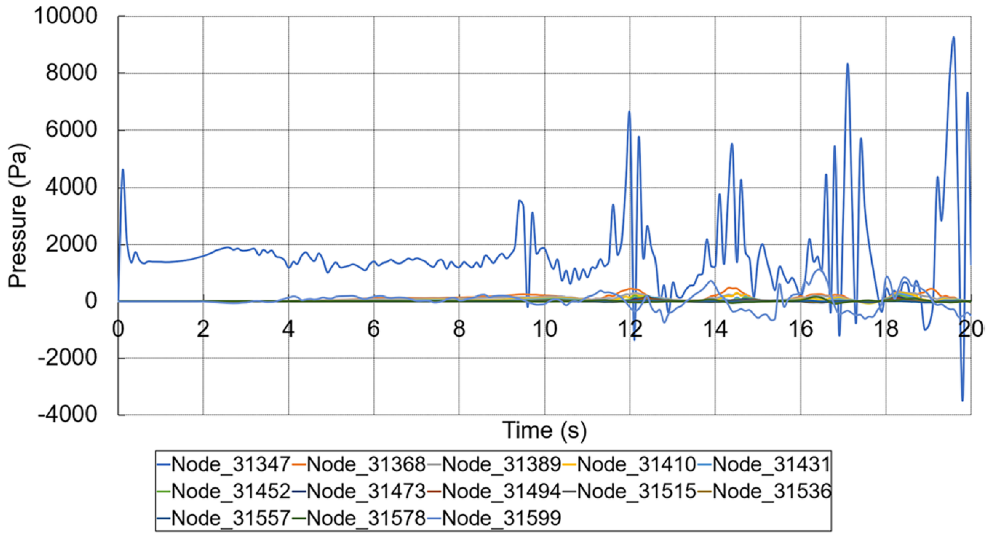


Figure D.4: Y-Direction Pressure Data From Impact E2

on the interface of the target water waves $E3$ and the structure is shown in Figure D.5.

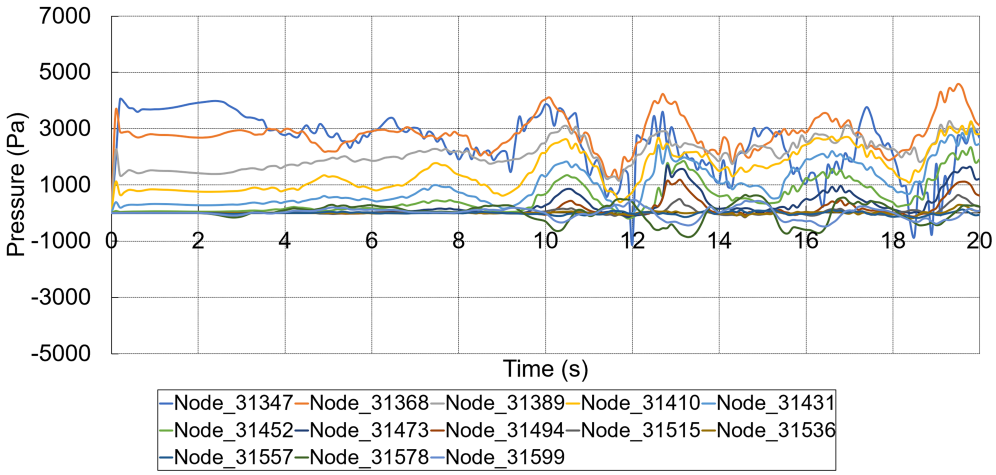


Figure D.5: X-Direction Pressure Data From Impact E3

For the wave-structure interaction simulation, the Y-direction pressure data on the interface of the target water waves $E3$ and the structure is shown in Figure D.6.

For the wave-structure interaction simulation, the X-direction pressure data

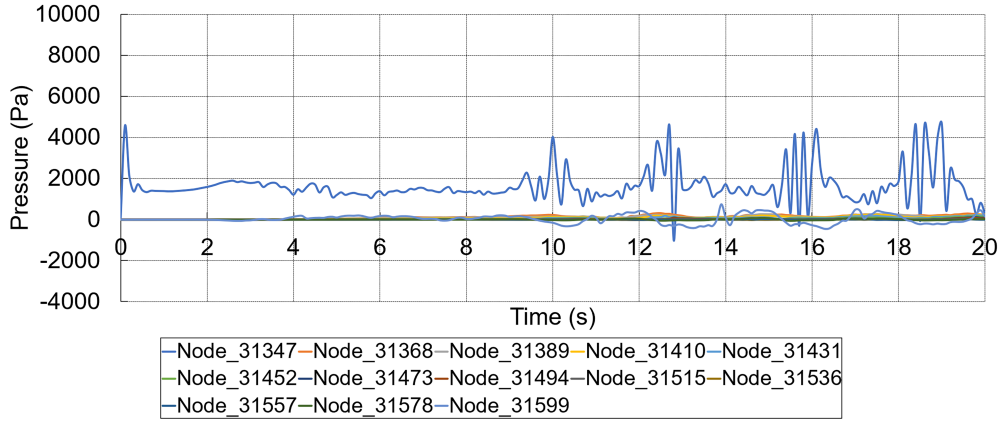


Figure D.6: Y-Direction Pressure Data From Impact E3

on the interface of the target water waves $E4$ and the structure is shown in Figure D.7.

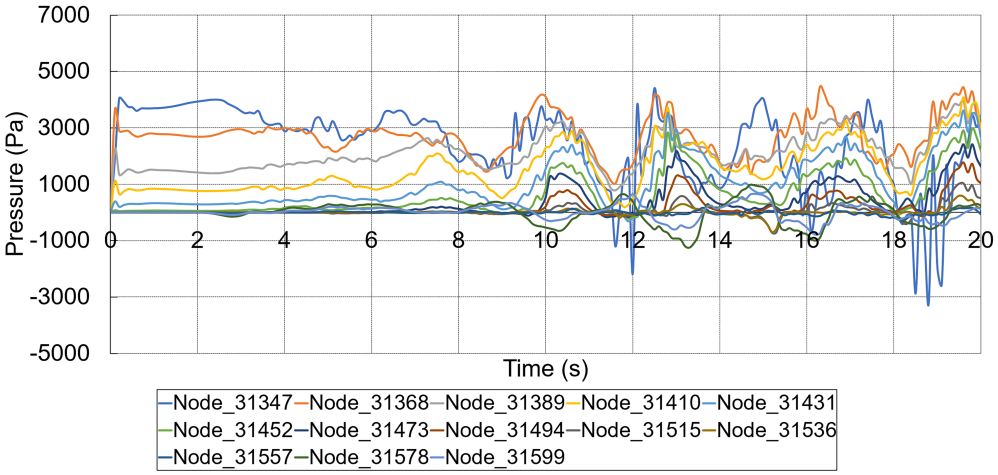


Figure D.7: X-Direction Pressure Data From Impact E4

For the wave-structure interaction simulation, the Y-direction pressure data on the interface of the target water waves $E4$ and the structure is shown in Figure D.8.

For the wave-structure interaction simulation, the X-direction pressure data on the interface of the target water waves $E5$ and the structure is shown in Figure D.9.

For the wave-structure interaction simulation, the Y-direction pressure data

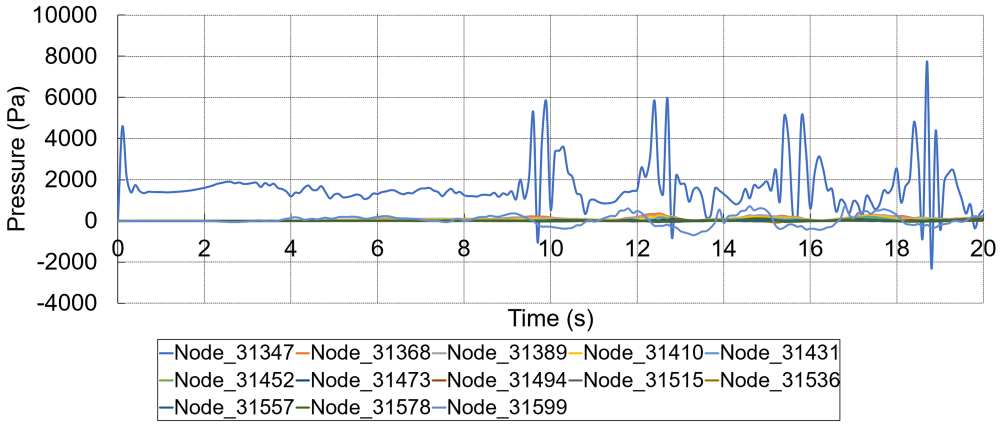


Figure D.8: Y-Direction Pressure Data From Impact E4

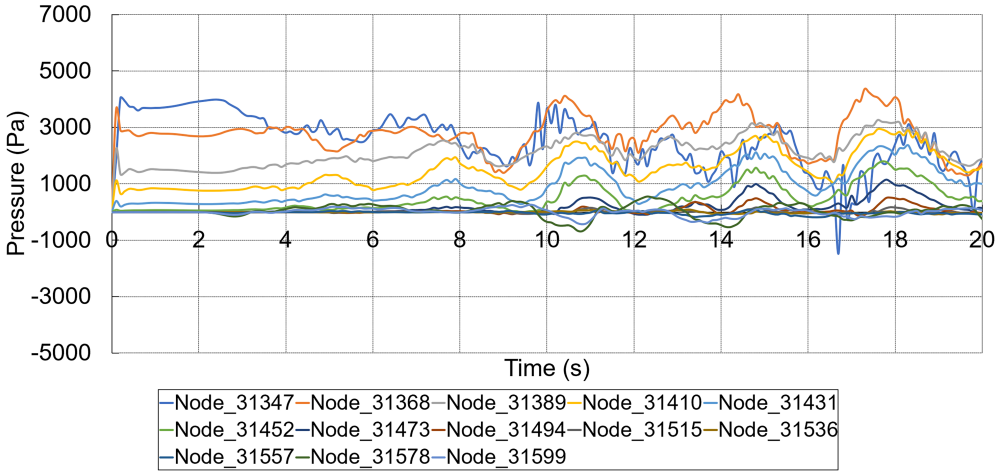


Figure D.9: X-Direction Pressure Data From Impact E5

on the interface of the target water waves $E5$ and the structure is shown in Figure D.10.

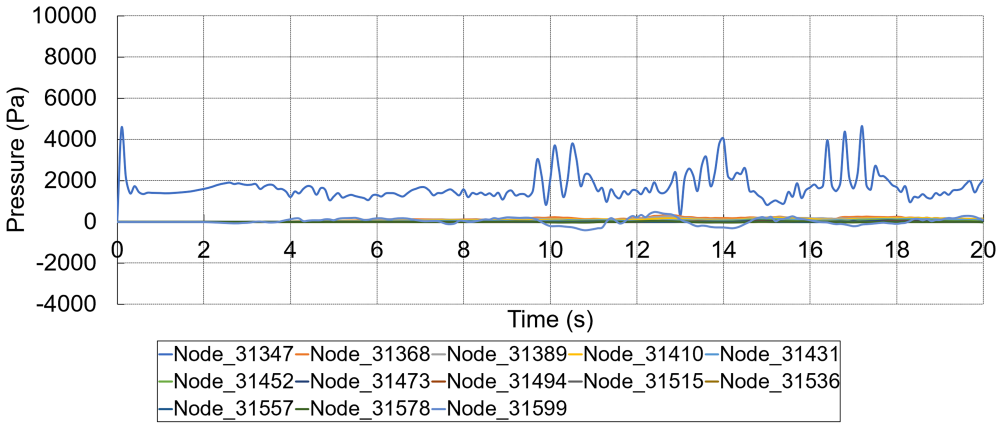


Figure D.10: Y-Direction Pressure Data From Impact E5

For the wave-structure interaction simulation, the X-direction pressure data on the interface of the target water waves $E6$ and the structure is shown in Figure D.11.

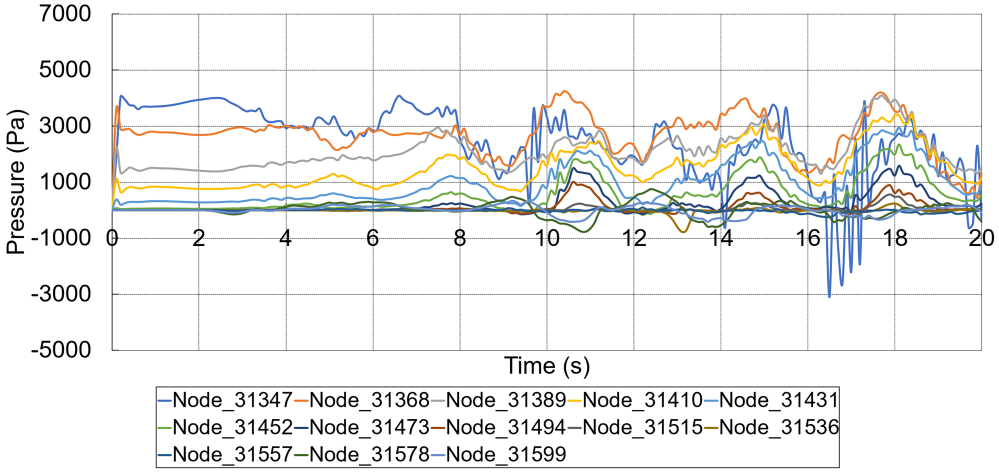


Figure D.11: X-Direction Pressure Data From Impact E6

For the wave-structure interaction simulation, the Y-direction pressure data on the interface of the target water waves $E6$ and the structure is shown in Figure D.12.

For the wave-structure interaction simulation, the X-direction pressure data

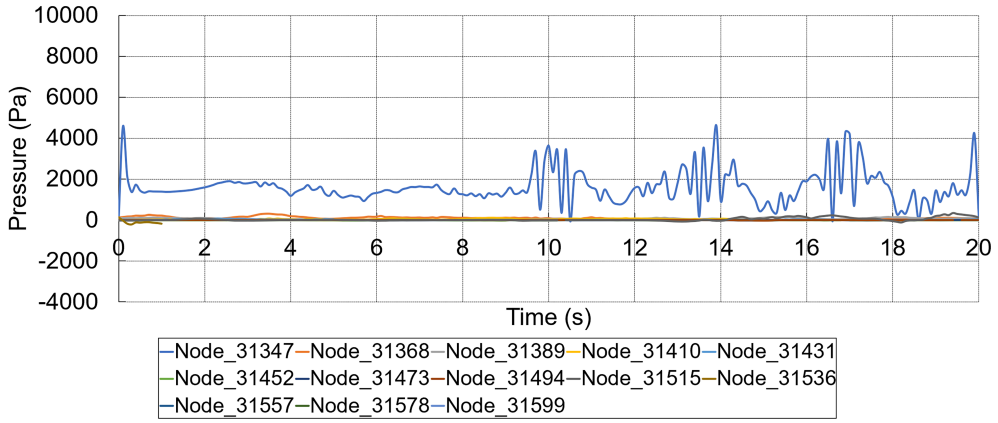


Figure D.12: Y-Direction Pressure Data From Impact E6

on the interface of the target water waves $E7$ and the structure is shown in Figure D.13.

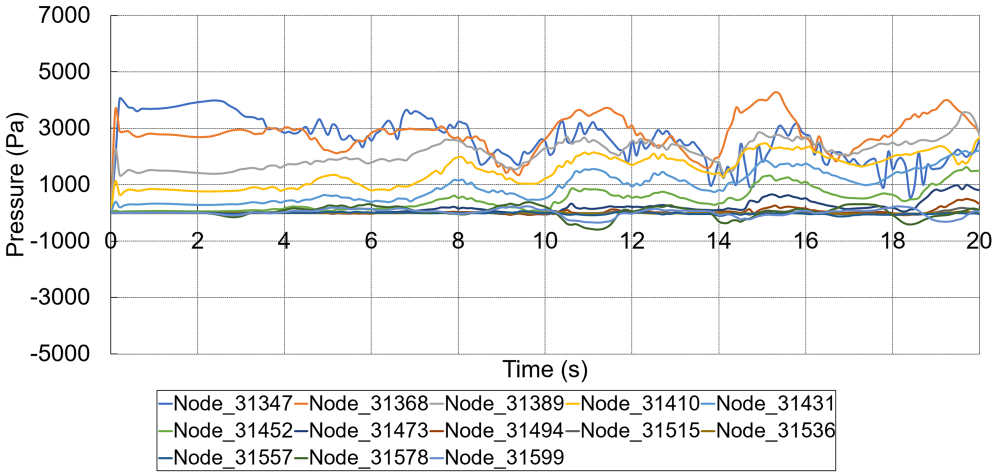


Figure D.13: X-Direction Pressure Data From Impact E7

For the wave-structure interaction simulation, the Y-direction pressure data on the interface of the target water waves $E7$ and the structure is shown in Figure D.14.

For the wave-structure interaction simulation, the X-direction pressure data on the interface of the target water waves $E8$ and the structure is shown in Figure D.15.

For the wave-structure interaction simulation, the Y-direction pressure data

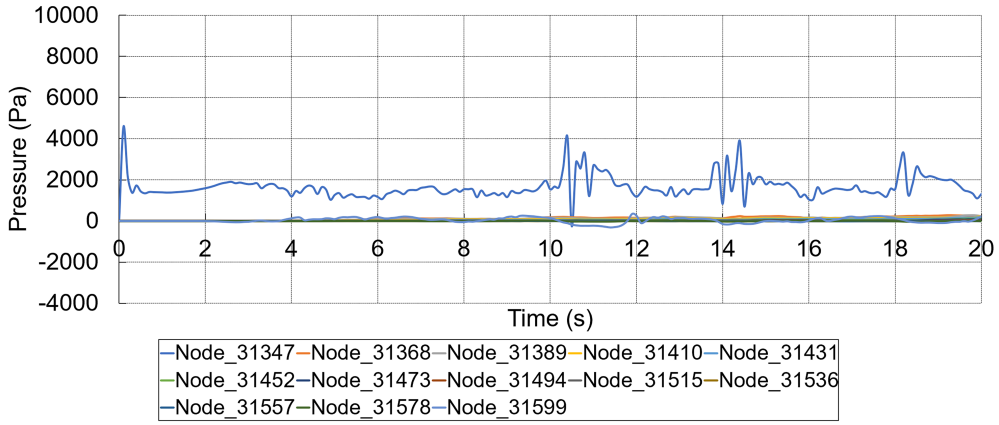


Figure D.14: Y-Direction Pressure Data From Impact E7

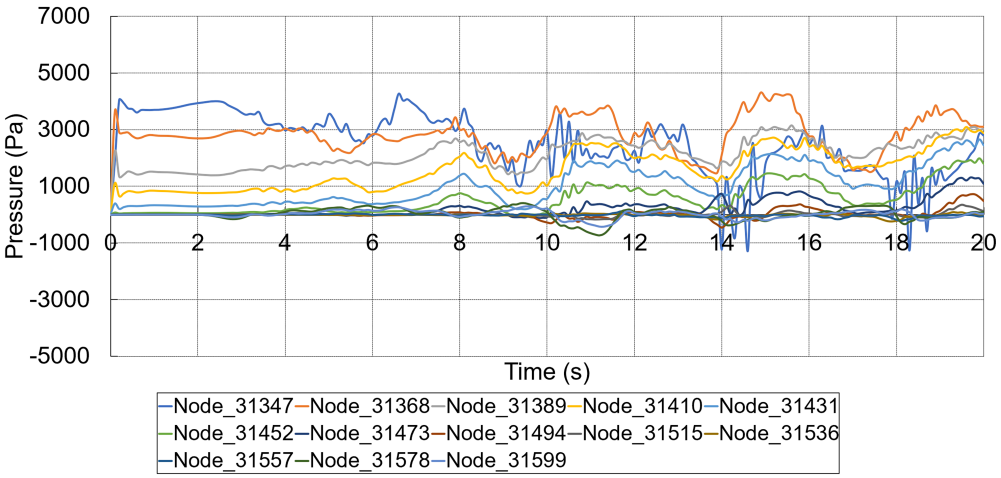


Figure D.15: X-Direction Pressure Data From Impact E8

on the interface of the target water waves $E8$ and the structure is shown in Figure D.16.

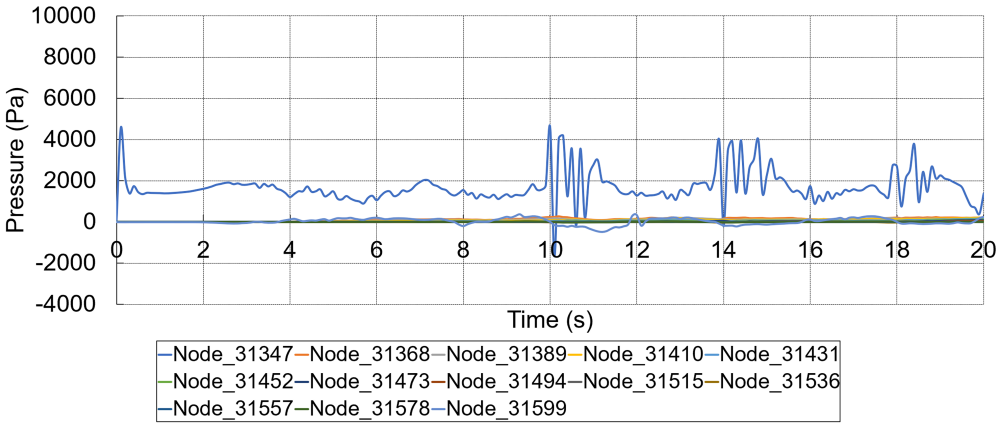


Figure D.16: Y-Direction Pressure Data From Impact E8

Bibliography

[1] Liquid Robotics. WG_SpecSheet_4.1, **2023**.

[2] Lenain, L.; Melville, W.K. Autonomous Surface Vehicle Measurements of the Ocean's Response to Tropical Cyclone Freda **2014**. Section: Journal of Atmospheric and Oceanic Technology, https://doi.org/10.1175/JTECH-D-14-00012.1.

[3] Mitarai, S.; McWilliams, J.C. Wave glider observations of surface winds and currents in the core of Typhoon Danas. *Geophysical Research Letters* **2016**, *43*. https://doi.org/10.1002/2016GL071115.

[4] Tian, D.; Zhang, H.; Zhang, W.; Zhou, F.; Sun, X.; Zhou, Y.; Ke, D. Wave Glider Observations of Surface Waves During Three Tropical Cyclones in the South China Sea. *Water* **2020**, *12*, 1331. Number: 5 Publisher: Multidisciplinary Digital Publishing Institute, https://doi.org/10.3390/w12051331.

[5] Son, Y.B.; Jung, S.K.; Cho, J.H.; Moh, T. Monitoring of the Surface Ocean Environment Under A Passing Typhoon Using A Wave Glider. *Journal of Coastal Research* **2020**, *95*, 168–172. https://doi.org/10.2112/SI95-033.1.

[6] Fitzpatrick, P.J.; Lau, Y.; Moorhead, R.; Skarke, A.; Merritt, D.; Kreider, K.; Brown, C.; Carlon, R.; Hine, G.; Lampoudi, T. A review of the 2014 Gulf of

Mexico Wave Glider® field program. *Marine Technology Society Journal* **2015**, *49*, 64–71. Publisher: Marine Technology Society.

[7] Tian, D.; Zhang, H.; Wang, S.; Zhang, W.; Sun, X.; Zhou, Y.; Zheng, G.; Jiang, H.; Yang, S.; Zhou, F. Sea Surface Wind Structure in the Outer Region of Tropical Cyclones Observed by Wave Gliders. *Journal of Geophysical Research: Atmospheres* **2023**, *128*, e2022JD037235. https://doi.org/10.1029/2022JD037235.

[8] Kosaka, N.; Umemiya, Y.; Endou, N.; Kura, T.; Matsubara, H.; Hisada, M.; Murata, A.; Mitarai, S. Simultaneous Observations of Atmosphere and Ocean Directly under Typhoons Using Autonomous Surface Vehicles. *Sola* **2023**, *19*, 116–125. https://doi.org/10.2151/sola.2023-016.

[9] Thomas, T.; Tarapore, D. Methods for the deployment of a swarm of wave gliders to monitor tropical cyclones. In Proceedings of the OCEANS 2023 - Limerick, **2023**, pp. 1–8. https://doi.org/10.1109/OCEANSLimerick52467.2023.10244741.

[10] Van Walree, F.; Willemsen, E. Wind loads on offshore structures. In Proceedings of the BOSS'88, **1988**, pp. 1413–1428.

[11] Bai, Y.; Jin, W.L. Wind Loads for Offshore Structures. In *Marine Structural Design (Second Edition)*; Bai, Y.; Jin, W.L., Eds.; Butterworth-Heinemann: Oxford, **2016**; pp. 95–118. https://doi.org/10.1016/B978-0-08-099997-5.00006-X.

[12] Misra, S.C. *Design principles of ships and marine structures*; CRC Press, **2015**.

[13] Isaacson, M. Wave and current forces on fixed offshore structures. *Canadian Journal of Civil Engineering* **1988**, *15*, 937–947. https://doi.org/10.1139/l88-125.

[14] Reuben, R.L. *Materials in marine technology*; Springer Science & Business Media, **2012**.

[15] Dong, Y.; Garbatov, Y.; Guedes Soares, C. Review on uncertainties in fatigue loads and fatigue life of ships and offshore structures. *Ocean Engineering* **2022**, *264*, 112514. https://doi.org/10.1016/j.oceaneng.2022.112514.

[16] Corigliano, P.; Frisone, F.; Chianese, C.; Altosole, M.; Piscopo, V.; Scamardella, A. Fatigue Overview of Ship Structures under Induced Wave Loads. *Journal of Marine Science and Engineering* **2024**, *12*, 1608. Number: 9 Publisher: Multidisciplinary Digital Publishing Institute, https://doi.org/10.3390/jmse12091608.

[17] Temarel, P.; Bai, W.; Bruns, A.; Derbanne, Q.; Dessi, D.; Dhavalikar, S.; Fonseca, N.; Fukasawa, T.; Gu, X.; Nestegård, A.; et al. Prediction of wave-induced loads on ships: Progress and challenges. *Ocean Engineering* **2016**, *119*, 274–308. https://doi.org/10.1016/j.oceaneng.2016.03.030.

[18] Kim, Y.J.; Yoshitake, I.; Liu, R. Composite hull structures subjected to wave-induced slamming impact. *Journal of Reinforced Plastics and Composites* **2014**, *33*, 3–13. Publisher: SAGE Publications Ltd STM, https://doi.org/10.1177/0731684413499831.

[19] Davies, P.; Bigourdan, B.; Choqueuse, D.; Lacotte, N.; Forest, B. Development of a Test to Simulate Wave Impact on Composite Sandwich Marine Structures. In *Dynamic Failure of Composite and Sandwich Structures*; Abrate, S.; Castanié, B.; Rajapakse, Y.D.S., Eds.; Springer Netherlands: Dordrecht, **2013**; Vol. 192, pp. 177–208. Series Title: Solid Mechanics and Its Applications, https://doi.org/10.1007/978-94-007-5329-7_5.

[20] Davies, W. *HMS Warrior: Ironclad Frigate 1860*; Seaforth Publishing, **2011**.

[21] Peng, Y.; Nianga, J.M.; Wang, Z. Characterization of Marine Composites: A Comprehensive Review of Marine Materials in Shipbuilding, Their Mechanical Behaviors and Degradation Mechanisms. *Global Journal of Engineering Sciences* **2025**, *12*. https://doi.org/10.33552/GJES.2025.12.000778.

[22] Bai, Y.; Jin, W.L. Marine Composite Materials and Structure. In *Marine Structural Design (Second Edition)*; Bai, Y.; Jin, W.L., Eds.; Butterworth-Heinemann: Oxford, **2016**; pp. 19–37. https://doi.org/10.1016/B978-0-08-099997-5.00002-2.

[23] Casari, P. *Applications marines des matériaux composites*; Ed. Techniques Ingénieur, **2008**.

[24] Mouritz, A.P.; Gellert, E.; Burchill, P.; Challis, K. Review of advanced composite structures for naval ships and submarines. *Composite Structures* **2001**, *53*, 21–42. https://doi.org/10.1016/S0263-8223(00)00175-6.

[25] Selvaraju, S.; Ilaiyavel, S. Applications of composites in marine industry. *Journal of engineering research and studies* **2011**, *2*, 89–91.

[26] Surís-Regueiro, J.C.; Garza-Gil, M.D.; Varela-Lafuente, M.M. Marine economy: A proposal for its definition in the European Union. *Marine Policy* **2013**, *42*, 111–124. https://doi.org/10.1016/j.marpol.2013.02.010.

[27] Stewart, R. Better boat building — trend to closed-mould processingcontinues. *Reinforced Plastics* **2011**, *55*, 30–36. https://doi.org/10.1016/S0034-3617(11)70183-7.

[28] Neşer, G. Polymer Based Composites in Marine Use: History and Future Trends. *Procedia Engineering* **2017**, *194*, 19–24. https://doi.org/10.1016/j.proeng.2017.08.111.

[29] Baley, C.; Davies, P.; Troalen, W.; Chamley, A.; Dinham-Price, I.; Marchandise, A.; Keryvin, V. Sustainable polymer composite marine structures: Developments and challenges. *Progress in Materials Science* **2024**, *145*, 101307. https://doi.org/10.1016/j.pmatsci.2024.101307.

[30] Marsh, G. Sailing at motor car speeds, thanks to composites. *Reinforced Plastics* **2016**, *60*, 298–301. https://doi.org/10.1016/j.repl.2016.05.001.

[31] Rubino, F.; Nisticò, A.; Tucci, F.; Carlone, P. Marine Application of Fiber Reinforced Composites: A Review. *Journal of Marine Science and Engineering* **2020**, *8*, 26. Number: 1 Publisher: Multidisciplinary Digital Publishing Institute, https://doi.org/10.3390/jmse8010026.

[32] Saravanan, M.; Kumar, D.B. A review on navy ship parts by advanced composite material. *Materials Today: Proceedings* **2021**, *45*, 6072–6077. https://doi.org/10.1016/j.matpr.2020.10.074.

[33] Siengchin, S. A review on lightweight materials for defence applications: Present and future developments. *Defence Technology* **2023**, *24*, 1–17. https://doi.org/10.1016/j.dt.2023.02.025.

[34] Asgharian, P.; Azizul, Z.H. Proposed Efficient Design for Unmanned Surface Vehicles, **2020**. arXiv:2009.01284 [cs], https://doi.org/10.48550/arXiv.2009.01284.

[35] Luo, H.; Jia, S.; Chen, S.; Ma, L. Embodied intelligence in unmanned surface vehicles: current applications and future perspectives. In Proceedings of the International Conference on Algorithms, High Performance Computing, and Artificial Intelligence (AHPCAI 2024). SPIE, **2024**, Vol. 13403, pp. 590–598.

[36] Ghazali, M.H.M.; Satar, M.H.A.; Rahiman, W. Unmanned surface ve-

hicles: From a hull design perspective. *Ocean Engineering* **2024**, *312*, 118977. https://doi.org/10.1016/j.oceaneng.2024.118977.

[37] Cevahir, A. Glass fibers. In *Fiber Technology for Fiber-Reinforced Composites*; Seydibeyoğlu, M.O.; Mohanty, A.K.; Misra, M., Eds.; Woodhead Publishing Series in Composites Science and Engineering, Woodhead Publishing, **2017**; pp. 99–121. https://doi.org/10.1016/B978-0-08-101871-2.00005-9.

[38] Berthelot, J.M. *Matériaux composite*; Lavoisier, **2012**.

[39] Mahltig, B.; Kyosev, Y. *Inorganic and composite fibers: production, properties, and applications*; **2018**. Publisher: Woodhead Publishing.

[40] Wallenberger, F.T.; Watson, J.C.; Li, H. Glass fibers. In *Composites*; ASM International, **2001**; pp. 27–34.

[41] Ertekin, M. Aramid fibers. In *Fiber Technology for Fiber-Reinforced Composites*; Seydibeyoğlu, M.O.; Mohanty, A.K.; Misra, M., Eds.; Woodhead Publishing Series in Composites Science and Engineering, Woodhead Publishing, **2017**; pp. 153–167. https://doi.org/10.1016/B978-0-08-101871-2.00007-2.

[42] Mather, R.R.; Wardman, R.H.; Rana, S. *The chemistry of textile fibres*; Royal Society of chemistry, **2023**.

[43] Campbell, F.C. Fibers and Reinforcements: The String That Provides the Strength. In *Manufacturing Processes for Advanced Composites*; Campbell, F.C., Ed.; Elsevier Science: Amsterdam, **2004**; pp. 39–62. https://doi.org/10.1016/B978-185617415-2/50003-4.

[44] Riggs, D.M.; Shuford, R.J.; Lewis, R.W. Graphite Fibers and Composites. In *Handbook of Composites*; Lubin, G., Ed.; Springer US: Boston, MA, **1982**; pp. 196–271. https://doi.org/10.1007/978-1-4615-7139-1_11.

[45] Bacon, R. Growth, structure, and properties of graphite whiskers. *Journal of applied physics* **1960**, *31*, 283–290. Publisher: American Institute of Physics.

[46] Donnet, J.B.; Bahl, O.P.; Bansal, R.C.; Wang, T.K. Carbon Fibers. In *Encyclopedia of Physical Science and Technology (Third Edition)*; Meyers, R.A., Ed.; Academic Press: New York, **2003**; pp. 431–455. https://doi.org/10.1016/B0-12-227410-5/00082-X.

[47] Manocha, L.M. Carbon Fibers. In *Encyclopedia of Materials: Science and Technology*; Buschow, K.H.J.; Cahn, R.W.; Flemings, M.C.; Ilschner, B.; Kramer, E.J.; Mahajan, S.; Veyssière, P., Eds.; Elsevier: Oxford, **2001**; pp. 906–916. https://doi.org/10.1016/B0-08-043152-6/00174-1.

[48] Marsh, G. Vinyl ester –the midway boat building resin. *Reinforced Plastics* **2007**, *51*, 20–23. https://doi.org/10.1016/S0034-3617(07)70248-5.

[49] Sarkar, P.K.; .; Kandasubramanian, B. Metals to polymer composites for submerged hull: a paradigm shift. *Polymer-Plastics Technology and Materials* **2021**, *60*, 1785–1819. Publisher: Taylor & Francis _eprint: https://doi.org/10.1080/25740881.2021.1930048, https://doi.org/10.1080/25740881.2021.1930048.

[50] Subbulakshmi, A.; Verma, M.; Keerthana, M.; Sasmal, S.; Harikrishna, P.; Kapuria, S. Recent advances in experimental and numerical methods for dynamic analysis of floating offshore wind turbines — An integrated review. *Renewable and Sustainable Energy Reviews* **2022**, *164*, 112525. https://doi.org/10.1016/j.rser.2022.112525.

[51] Altomare, C.; Domínguez, J.M.; Crespo, A.J.C.; González-Cao, J.; Suzuki, T.; Gómez-Gesteira, M.; Troch, P. Long-crested wave generation and absorption for SPH-based DualSPHysics model. *Coastal Engineering* **2017**, *127*, 37–54. https://doi.org/10.1016/j.coastaleng.2017.06.004.

[52] Dean, R.G.; Dalrymple, R.A. *Water wave mechanics for engineers and scientists*; Vol. 2, World scientific publishing company, **1991**.

[53] Pelfrene, J. Study of the SPH method for simulation of regular and breaking waves. Master's degree, Ghent University, Belgium, **2011**.

[54] Anbarsooz, M.; Passandideh-Fard, M.; Moghiman, M. Fully nonlinear viscous wave generation in numerical wave tanks. *Ocean Engineering* **2013**, *59*, 73–85. https://doi.org/10.1016/j.oceaneng.2012.11.011.

[55] Park, J.; Cho, D.; Jang, T. A numerical experiment on a new piston-type wavemaker: Shallow water approximation. *International Journal of Naval Architecture and Ocean Engineering* **2023**, *15*, 100535. https://doi.org/10.1016/j.ijnaoe.2023.100535.

[56] Francis, V.; Ramakrishnan, B.; Rudman, M.; Valizadeh, A. Generating stable solitary waves with a piston-type wavemaker. *Coastal Engineering* **2020**, *157*, 103633. https://doi.org/10.1016/j.coastaleng.2020.103633.

[57] Miquel, A.M.; Kamath, A.; Alagan Chella, M.; Archetti, R.; Bihs, H. Analysis of Different Methods for Wave Generation and Absorption in a CFD-Based Numerical Wave Tank. *Journal of Marine Science and Engineering* **2018**, *6*, 73. Number: 2 Publisher: Multidisciplinary Digital Publishing Institute, https://doi.org/10.3390/jmse6020073.

[58] Ohyama, T.; Nadaoka, K. Development of a numerical wave tank for analysis of nonlinear and irregular wave field. *Fluid Dynamics Research* **1991**, *8*, 231–251. https://doi.org/10.1016/0169-5983(91)90045-K.

[59] Hu, Z.Z.; Greaves, D.; Raby, A. Numerical wave tank study of extreme waves and wave-structure interaction using OpenFoam®. *Ocean Engineering* **2016**, *126*, 329–342. https://doi.org/10.1016/j.oceaneng.2016.09.017.

[60] Westphalen, J.; Greaves, D.M.; Williams, C.J.K.; Hunt-Raby, A.C.; Zang, J. Focused waves and wave-structure interaction in a numerical wave tank. *Ocean Engineering* **2012**, *45*, 9–21. https://doi.org/10.1016/j.oceaneng.2011.12.016.

[61] Hughes, T.J.R.; Liu, W.K.; Zimmermann, T.K. Lagrangian-Eulerian finite element formulation for incompressible viscous flows. *Computer Methods in Applied Mechanics and Engineering* **1981**, *29*, 329–349. https://doi.org/10.1016/0045-7825(81)90049-9.

[62] Donea, J.; Giuliani, S.; Halleux, J.P. An arbitrary lagrangian-eulerian finite element method for transient dynamic fluid-structure interactions. *Computer Methods in Applied Mechanics and Engineering* **1982**, *33*, 689–723. https://doi.org/10.1016/0045-7825(82)90128-1.

[63] Souli, M.; Zolesio, J.P. Arbitrary Lagrangian–Eulerian and free surface methods in fluid mechanics. *Computer Methods in Applied Mechanics and Engineering* **2001**, *191*, 451–466. https://doi.org/10.1016/S0045-7825(01)00313-9.

[64] Souli, M.; Gabrys, J. Fluid Structure Interaction for Bird Impact Problem: Experimental and Numerical Investigation. *Computer Modeling in Engineering & Sciences* **1970**, *85*, 177–192. Publisher: Tech Science Press, https://doi.org/10.3970/cmes.2012.085.177.

[65] Souli, M.; Shahrour, I. A coupling method for soil structure interaction problems. *International Journal for Numerical and Analytical Methods in Geomechanics* **2013**, *37*, 1140–1153. _eprint: https://onlinelibrary.wiley.com/doi/pdf/10.1002/nag.2080, https://doi.org/10.1002/nag.2080.

[66] Ozdemir, Z.; Moatammedi, M.; Fahjan, Y.; Souli, M. ALE and Fluid Structure Interaction for Sloshing Analysis. *The international journal of*

multiphysics. **2009**, *3*, 307–336. Publisher: Multi-Science Publishing, https://doi.org/10.1260/175095409788922257.

[67] Aquelet, N.; Souli, M.; Olovsson, L. Euler–Lagrange coupling with damping effects: Application to slamming problems. *Computer Methods in Applied Mechanics and Engineering* **2006**, *195*, 110–132. https://doi.org/10.1016/j.cma.2005.01.010.

[68] Gong, S.W. Transient response of stiffened composite submersible hull to underwater shock and bubble. *Composite Structures* **2019**, *213*, 243–251. https://doi.org/10.1016/j.compstruct.2019.01.097.

[69] Andersen, T.L.; Frigaard, P. Lecture notes for the course in water wave mechanics. Technical Report DCE Lecture notes No. 16, Department of Civil Engineering, Aalborg University, **2007**. Publisher: Department of Civil Engineering, Aalborg University.

[70] Le Méhauté, B. An Introduction to Water Waves. In *An Introduction to Hydrodynamics and Water Waves*; Le Méhauté, B., Ed.; Springer: Berlin, Heidelberg, **1976**; pp. 197–211. https://doi.org/10.1007/978-3-642-85567-2_15.

[71] Airy, G.B. Tides and Waves. In *Encyclopaedia Metropolitana*; William Clowes and Sons, **1845**; pp. 241–396.

[72] Havelock, T. LIX. Forced surface-waves on water. *The London, Edinburgh, and Dublin Philosophical Magazine and Journal of Science* **1929**, *8*, 569–576. Publisher: Taylor & Francis _eprint: https://doi.org/10.1080/14786441008564913, https://doi.org/10.1080/14786441008564913.

[73] Biésel, F.; Suquet, F. Les Appareils Générateurs de Houle en Laboratoire. *La Houille Blanche* **1951**, *37*, 147–165. https://doi.org/10.1051/lhb/1951033.

[74] Biésel, F.; Suquet, F. Les Appareils Générateurs de Houle en Laboratoire. *La Houille Blanche* **1952**, *38*, 779–801. https://doi.org/10.1051/lhb/1952051.

[75] Sarmento, A. Wave flume experiments on two-dimensional oscillating water column wave energy devices. *Experiments in fluids* **1992**, *12*, 286–292. Publisher: Springer.

[76] Izquierdo, U.; Esteban, G.A.; Blanco, J.M.; Albaina, I.; Peña, A. Experimental validation of a CFD model using a narrow wave flume. *Applied Ocean Research* **2019**, *86*, 1–12. https://doi.org/10.1016/j.apor.2019.02.012.

[77] Wu, N.J.; Hsiao, S.C.; Chen, H.H.; Yang, R.Y. The study on solitary waves generated by a piston-type wave maker. *Ocean Engineering* **2016**, *117*, 114–129. https://doi.org/10.1016/j.oceaneng.2016.03.020.

[78] Schimmels, S.; Sriram, V.; Didenkulova, I.; Fernández, H. On the generation of tsunami in a large scale wave flume. *Coastal Engineering Proceedings* **2014**, *1*, 14.

[79] Lee, S.; Ko, K.; Hong, J.W. Comparative study on the breaking waves by a piston-type wavemaker in experiments and SPH simulations. *Coastal Engineering Journal* **2020**, *62*, 267–284. Publisher: Taylor & Francis. https://doi.org/10.1080/21664250.2020.1747141.

[80] Nouioui, B.; Doğan, M. Irregular wavemaker (piston type) in a unmerical and physical wave tank. *Usak University Journal of Engineering Sciences* **2022**, *5*, 95–116. Publisher: Usak University.

[81] Spinneken, J.; Swan, C. Second-order wave maker theory using force-feedback control. Part II: An experimental verification of regular wave generation. *Ocean Engineering* **2009**, *36*, 549–555. https://doi.org/10.1016/j.oceaneng.2009.01.007.

[82] Khalilabadi, M.R.; Bidokhti, A.A. Design and construction of an optimum wave flume. *Journal of Applied Fluid Mechanics* **2013**, *5*, 99–103.

[83] Lal, A.; Elangovan, M. CFD simulation and validation of flap type wavemaker. *World Academy of Science, Engineering and Technology* **2008**, *46*, 76–82.

[84] Shehab, A.; El-Baz, A.M.; Elmarhomy, A.M. CFD modeling of regular and irregular waves generated by flap type wave maker. *J. of Adv. Res. in Num. Heat Trans* **2021**, *85*, 128–144.

[85] Saincher, S.; Banerjeea, J. Design of a Numerical Wave Tank and Wave Flume for Low Steepness Waves in Deep and Intermediate Water. *Procedia Engineering* **2015**, *116*, 221–228. https://doi.org/10.1016/j.proeng.2015.08.394.

[86] Dao, M.H.; Chew, L.W.; Zhang, Y. Modelling physical wave tank with flap paddle and porous beach in OpenFOAM. *Ocean Engineering* **2018**, *154*, 204–215. https://doi.org/10.1016/j.oceaneng.2018.02.024.

[87] Nurdin, Z.; Muarif, M.; Munzir, S.; Tulus, T.; Mardiningsih, M.; Ramli, M. Three Dimensional Model of Snake-Type Wavemakers using Linear Wave Theory. In Proceedings of the 2018 International Conference on Electrical Engineering and Informatics (ICELTICs), **2018**, pp. 155–158. https://doi.org/10.1109/ICELTICS.2018.8548810.

[88] Park, J.C.; Uno, Y.; Sato, T.; Miyata, H.; Chun, H.H. Numerical reproduction of fully nonlinear multi-directional waves by a viscous 3D numerical wave tank. *Ocean Engineering* **2004**, *31*, 1549–1565. https://doi.org/10.1016/j.oceaneng.2003.12.009.

[89] Lee, S.; Hong, J.W. A Semi-Infinite Numerical Wave Tank Using Discrete Particle Simulations. *Journal of Marine Science and Engineering* **2020**,

8, 159. Number: 3 Publisher: Multidisciplinary Digital Publishing Institute, https://doi.org/10.3390/jmse8030159.

[90] Balitsky, P. A numerical investigation of the array effects of wave energy converters with a realistic power take-off system utilizing a coupled model suite. PhD Thesis, Ghent University, **2019**.

[91] Head, M.; Seo, J.; Shokouhian, M.; Schaffer, W. Foundation Anchorages for Offshore Wind Turbines in Deep Water Using Composite Materials. Technical Report, Morgan State University, **2016**

[92] Gutiérrez, E.M. Experimental study of water waves: nonlinear effects and absorption. PhD Thesis, Université Pierre et Marie Curie-Paris VI, **2017**.

[93] Finkl, C.W.; Makowski, C. *Encyclopedia of Coastal Science*; Springer Cham, **2019**.

[94] Rohani, I.; Thaha, M.A.; Hatta, M.P.; Paotonan, C. Stability of breakwater armour using rock pockets on transition wave. In Proceedings of the IOP Conference Series: Earth and Environmental Science. IOP Publishing, **2020**, Vol. 419, p. 012131. Issue: 1.

[95] Miranda, F.; Margarida Bento, A.; Chambel, J.; Francisca Sarmento, M.; Rosa-Santos, P.; Taveira-Pinto, F.; Fazeres-Ferradosa, T. A novel and simple passive absorption system for wave-current flumes. *Alexandria Engineering Journal* **2023**, *71*, 463–477. https://doi.org/10.1016/j.aej.2023.03.067.

[96] Lean, G.H. A Simplified Theory Of Permeable Wave Absorbers. *Journal of Hydraulic Research* **1967**, *5*, 15–30. https://doi.org/10.1080/00221686709500187.

[97] Lim, H.C. Optimum design of a sloping-wall-type wave absorber placed in a sinusoidal propagating wave. *Ocean engineering* **2014**, *88*, 588–597. Publisher: Elsevier.

[98] Neelamani, S.; Prasad Raju, P.V. Wave interaction with parabolic corrugated and perforated wave absorbers. *ISH Journal of Hydraulic Engineering* **2004**, *10*, 19–32. https://doi.org/10.1080/09715010.2004.10514741.

[99] Hodaei, S.M.R.; Chamani, M.R.; Moghim, M.N.; Mansoorzadeh, S.; Kabiri-Samani, A. Experimental study on reflection coefficient of curved perforated plate. *Journal of Marine Science and Application* **2016**, *15*, 382–387. https://doi.org/10.1007/s11804-016-1383-5.

[100] Saprykina, Y.V.; Kuznetsov, S.Y.; Kovalenko, A.N. Experimental studies of the local reflection of long waves from an underwater slope. *Oceanology* **2015**, *55*, 171–181. https://doi.org/10.1134/S0001437015020137.

[101] Urrego-Pabón, J.; Mercado, J.; Obando-Vega, F.; Rubio-Clemente, A.; Chica, E. Numerical and experimental study of several passive wave absorber behavior in a wave channel. *Results in Engineering* **2024**, *23*, 102455. https://doi.org/10.1016/j.rineng.2024.102455.

[102] Das, S.; Bora, S.N. Reflection of oblique ocean water waves by a vertical rectangular porous structure placed on an elevated horizontal bottom. *Ocean Engineering* **2014**, *82*, 135–143. https://doi.org/10.1016/j.oceaneng.2014.02.035.

[103] Schäffer, H.A.; Klopman, G. Review of Multidirectional Active Wave Absorption Methods. *Journal of Waterway, Port, Coastal, and Ocean Engineering* **2000**, *126*, 88–97. Publisher: American Society of Civil Engineers, https://doi.org/10.1061/(ASCE)0733-950X(2000)126:2(88).

[104] Milgram, J.H. Active water-wave absorbers. *Journal of Fluid Mechanics* **1970**, *42*, 845–859. https://doi.org/10.1017/S0022112070001635.

[105] Chen, Q.; Kelly, D.M.; Zang, J. On the relaxation approach for wave ab-

sorption in numerical wave tanks. *Ocean Engineering* **2019**, *187*, 106210. https://doi.org/10.1016/j.oceaneng.2019.106210.

[106] De Vita, F.; Di Mascio, A.; Onorato, M. A Navier–Stokes numerical wave tank with a pressure-based relaxation zone method. *Ocean Engineering* **2022**, *266*, 113207. https://doi.org/10.1016/j.oceaneng.2022.113207.

[107] Jacobsen, N.G.; Fuhrman, D.R.; Fredsøe, J. A wave generation toolbox for the open-source CFD library: OpenFoam®. *International Journal for Numerical Methods in Fluids* **2012**, *70*, 1073–1088. _eprint: https://onlinelibrary.wiley.com/doi/pdf/10.1002/fld.2726, https://doi.org/10.1002/fld.2726.

[108] Perić, R.; Vukčević, V.; Abdel-Maksoud, M.; Jasak, H. Optimizing wave generation and wave damping in 3D-flow simulations with implicit relaxation zones. *Coastal Engineering* **2022**, *171*, 104035. https://doi.org/10.1016/j.coastaleng.2021.104035.

[109] Strutt, J.W.; Rayleigh, J.W.S. *The theory of sound*; Vol. 1, Macmillan, **1877**.

[110] Rayleigh, J.W.S.B. *The theory of sound*; Vol. 2, Macmillan, **1896**.

[111] Noh, W.F. CEL: A time-dependent, two-space-dimensional, coupled Eulerian-Lagrange code. Technical report, Lawrence Livermore National Lab.(LLNL), Livermore, CA (United States), **1963**.

[112] Donea, J.; Fasoli-Stella, P.; Giuliani, S. Lagrangian and Eulerian finite element techniques for transient fluid-structure interaction problems. In *Structural mechanics in reactor technology*; **1977**.

[113] Belytschko, T.; Flanagan, D.P.; Kennedy, J.M. Finite element methods with user-controlled meshes for fluid-structure interaction. *Computer Methods*

in Applied Mechanics and Engineering **1982**, *33*, 669–688. https://doi.org/10.1016/0045-7825(82)90127-X.

[114] Loiseau, F. Simulation numérique d'écoulements à surface libre: caractérisation de la couche limite de fond engendrée par un écoulement de houle et de courant. PhD Thesis, Lille 1, **1996**.

[115] Wang, H.h.; Jin, X.l. Numerical simulation of solitary wave interaction with wave wall of breakwater using arbitrary Lagrangian–Eulerian method. *Proceedings of the Institution of Mechanical Engineers, Part M: Journal of Engineering for the Maritime Environment* **2017**, *231*, 452–463. Publisher: SAGE Publications, https://doi.org/10.1177/1475090216653065.

[116] Xiang, T.; Istrati, D. Assessment of Extreme Wave Impact on Coastal Decks with Different Geometries via the Arbitrary Lagrangian-Eulerian Method. *Journal of Marine Science and Engineering* **2021**, *9*, 1342. Number: 12 Publisher: Multidisciplinary Digital Publishing Institute, https://doi.org/10.3390/jmse9121342.

[117] Pákozdi, C.; Kamath, A.; Wang, W.; Bihs, H. Application of Arbitrary Lagrangian–Eulerian strips with fully nonlinear wave kinematics for force estimation. *Marine Structures* **2022**, *83*, 103190. https://doi.org/10.1016/j.marstruc.2022.103190.

[118] Tsao, W.H.; Kees, C.E. An Arbitrary Lagrangian-Eulerian Regularized Boundary Integral Method for Nonlinear Free-Surface Flows over Complex Topography and Wave-Structure Interaction. *Engineering Analysis with Boundary Elements* **2023**, *157*, 326–341. https://doi.org/10.1016/j.enganabound.2023.09.019.

[119] Fan, X.; Zhao, J.; Qi, C.; Wang, X.; Lyu, X. On the water entry impact characteristics of high-speed vehicle with an Arbitrary Lagrangian-Eulerian method. *Applied Ocean Research* **2024**, *150*, 104118. https://doi.org/10.1016/j.apor.2024.104118.

[120] Brooks, A.N.; Hughes, T.J.R. Streamline upwind/Petrov-Galerkin formulations for convection dominated flows with particular emphasis on the incompressible Navier-Stokes equations. *Computer Methods in Applied Mechanics and Engineering* **1982**, *32*, 199–259. https://doi.org/10.1016/0045-7825(82)90071-8.

[121] Hughes, T.J.R.; Tezduyar, T.E. Finite element methods for first-order hyperbolic systems with particular emphasis on the compressible euler equations. *Computer Methods in Applied Mechanics and Engineering* **1984**, *45*, 217–284. https://doi.org/10.1016/0045-7825(84)90157-9.

[122] Hughes, T.J.R.; Mallet, M. A new finite element formulation for computational fluid dynamics: III. The generalized streamline operator for multidimensional advective-diffusive systems. *Computer Methods in Applied Mechanics and Engineering* **1986**, *58*, 305–328. https://doi.org/10.1016/0045-7825(86)90152-0.

[123] Chorin, A.J.; Hughes, T.J.; McCracken, M.F.; Marsden, J.E. Product formulas and numerical algorithms. *Communications on Pure and Applied Mathematics* **1978**, *31*, 205–256. Publisher: Wiley Subscription Services, Inc., A Wiley Company New York.

[124] Benson, D.J. Computational methods in Lagrangian and Eulerian hydrocodes. *Computer Methods in Applied Mechanics and Engineering* **1992**, *99*, 235–394. https://doi.org/10.1016/0045-7825(92)90042-I.

[125] Souli, M.; Sigrist, J.F. *Interaction fluide-structure: modélisation et simulation numérique*; Hermés science, **2009**.

[126] Souli, M.; Benson, D.J. *Arbitrary Lagrangian Eulerian and fluid-structure interaction: numerical simulation*; John Wiley & Sons, **2013**.

[127] Godunov, S.K. A difference scheme for numerical solution of discontinu-

ous solution of hydrodynamic equations. *Math. Sbornik* **1959**, *47*, 271–306.

[128] Van Leer, B. Towards the ultimate conservative difference scheme. IV. A new approach to numerical convection. *Journal of Computational Physics* **1977**, *23*, 276–299. https://doi.org/10.1016/0021-9991(77)90095-X.

[129] Amsden, A.A.; Hirt, C.W. YAQUI: an arbitrary Lagrangian–Eulerian computer program for fluid flow at all speeds. Technical report, Los Alamos National Lab.(LANL), Los Alamos, NM (United States), **1973**.

[130] Amsden, A.A.; Ruppel, H.M.; Hirt, C.W. SALE: A simplified ALE computer program for fluid flow at all speeds. Technical report, Los Alamos National Lab.(LANL), Los Alamos, NM (United States), **1980**.

[131] Benson, D.J. A mixture theory for contact in multi-material Eulerian formulations. *Computer Methods in Applied Mechanics and Engineering* **1997**, *140*, 59–86. https://doi.org/10.1016/S0045-7825(96)01050-X.

[132] Youngs, D.L. Time-Dependent Multi-material Flow with Large Fluid Distortion. In *Numerical Methods for Fluid Dynamics*; Morton, K.W.; Baines, M.J., Eds.; **1982**; pp. 273–285. Journal Abbreviation: Num. Method Fluid Dyn.

[133] Youngs, D.L. An interface tracking method for a 3D Eulerian hydrodynamics code. *Atomic Weapons Research Establishment (AWRE) Technical Report* **1984**, *44*, 35.

[134] Bourago, N.G.; Kukudzhanov, V.N. A review of contact algorithms. *Mechanics of solids* **2005**, *40*, 35–71. Publisher: New York: Allerton Press, c1972-c1991.

[135] Wriggers, P. Finite element algorithms for contact problems. *Archives of computational methods in engineering* **1995**, *2*, 1–49. Publisher: Springer.

[136] Zhong, Z.H. *Finite element procedures for contact-impact problems*; Oxford university press, **1993**.

Unité Mécanique Lille UML J. Boussinesq

Titre: Simulation numérique du comportement mécanique d'un nouveau matériau composite en milieu marin

Mots clés: Interaction Fluide-Structure ; Arbitrary Lagrangian Eulerian ; Impact de la vague ; Vague linéaire ; Simulation numérique ; Véhicule de surface

Résumé: Avec le développement des équipements intelligents, les véhicules de surface sans pilote sont aujourd'hui largement utilisés dans les domaines de la défense, de la surveillance environnementale et de l'énergie offshore, tout en présentant des perspectives d'application convaincantes. Grâce à leur capacité à utiliser des énergies renouvelables en mer, les véhicules de surface tels que le Wave glider et l'AutoNaut peuvent effectuer des missions de longue durée en milieu marin. La coque d'un véhicule de surface de petite à moyenne taille est généralement constituée d'un matériau composite à structure sandwich, avec la peau étant généralement constituée de polymères renforcés de fibres de verre ou de fibres de carbone. L'étude de l'interaction entre la coque d'un véhicule de surface et la vague, ainsi que l'évaluation du niveau des charges d'impact des vagues dans ses conditions de fonctionnement typiques en mer, constituent l'objectif principal de cette recherche. Cela peut aussi soutenir la recherche sur la réponse mécanique et le comportement en fatigue des structures composites sous l'effet d'une charge dynamique de vagues. L'étude du problème de l'interaction vague-structure est effectuée par le biais des expérimentations numériques. Les simulations numériques sont réalisées à l'aide de la méthode Arbitrary Lagrangian Eulerian. Cette approche combine les avantages des formulations lagrangiennes et eulériennes, permettant la simulation de multi-matériaux et la présence de grandes déformations des matériaux dans la simulation. Sur la base de cette approche, un modèle numérique de canal à houle avec des zones d'amortissement pour l'absorption des vagues est construit, qui est d'abord appliqué pour simuler les vagues correspondant aux conditions de mer de fonctionnement typiques du Wave glider, puis, des scènes d'impact des vagues sont simulées avec une structure simulant le flotteur du Wave glider couplée dans le canal à houle numérique. La génération de vagues est basée sur la théorie de vague linéaire et la théorie de génération de vagues du générateur de type piston. Prenant en compte les dimensions du canal à houle numérique et les paramètres des vagues ciblées, quatre séries de vagues expérimentales sont mises en place. Les vagues générées sont mesurées et comparées par rapport aux solutions analytiques des vagues ciblées dérivées de la théorie de vague linéaire. Les taux d'erreur des vagues simulées sont calculés afin de vérifier l'efficacité du canal à houle numérique et la précision de la génération de vagues. La simulation de l'interaction vague-structure utilise les mêmes quatre séries de vagues. L'algorithme de couplage basé sur la méthode de pénalisation est utilisé pour modéliser le contact entre les fluides et la structure, aussi pour prédire les charges de vagues à l'interface vague-structure. Les données relatives à la charge de vagues sont collectées et analysées. Le changement de posture de la structure sous l'influence des impacts de vague est également étudié. L'usage des ressources informatiques consacrées aux simulations de la génération de vagues et celles de l'interaction fluide-structure est présenté et analysé. En s'appuyant sur la rentabilité et l'efficacité de la méthode numérique, cette recherche a étudié le problème de la génération de vagues et de l'interaction fluide-structure par le biais de simulations numériques. Le modèle numérique de canal à houle mis en œuvre est validé et peut être étendu à des scénarios d'application plus complexes.

Title: Numerical simulation of the mechanical behavior of a new composite material in the marine environment

Keywords: Fluid-Structure Interaction; Arbitrary Lagrangian Eulerian; Water wave impact; Linear wave; Numerical simulation; Surface vehicle

Abstract: With the development of intelligent equipment, unmanned surface vehicles nowadays are widely used in the fields of defense, environmental surveillance and offshore energy, and possess promising application prospects. Benefiting from the ability to make use of renewable energy at sea, surface vehicles such as the Wave glider and AutoNaut are capable of performing long-duration missions in marine environments. The hull structure of a small to medium-sized surface vessel is generally made of sandwich-structured composite materials with the skin generally being the glass fiber or carbon fiber-reinforced polymers. Investigating the interaction between the hull structure of a surface vehicle and water waves, as well as evaluating the level of wave impact loads under its operating sea state conditions, are the major focus of this study. This can support research on the mechanical response and fatigue behavior of composite structures under dynamic loading induced by water waves. The wave-structure interaction problem is carried out through numerical experiments in this study. Numerical simulations are performed using the Arbitrary Lagrangian Eulerian method. This approach combines the advantages of the Lagrangian and Eulerian formulations, allowing for multi-material computation and the presence of large material deformations in the simulation. Based on this approach, a numerical wave flume model with damping zones for water wave absorption is constructed, which is first applied to simulate the water waves corresponding to the working sea conditions of the wave glider, and then, the wave impact scenarios are carried out with a structure simulating the wave glider's float coupled into the numerical wave flume. The numerical generation of water waves is on the basis of linear wave theory and piston-type wavemaker theory. Four sets of target waves have been set up based on the dimension parameters of the numerical wave flume and the wave glider's general operating sea states. Profiles of generated water waves are measured and compared to the analytical solution of target waves derived from the linear wave theory. Error rates of simulated water waves are calculated in order to verify the effectiveness of the numerical wave flume and the accuracy of the wave generation. Then, the wave-structure interaction simulations use the same four sets of target waves. A coupling algorithm based on the penalty method is used to model the contact between fluids and the structure, also to predict the wave loads at the wave-structure interface. Wave load data is collected and analyzed. The posture changes of the structure under influence of wave impacts are also investigated. Computational resources devoted to water wave generation and wave-structure interaction simulations are studied to verify different weightings of Arbitrary Lagrangian Eulerian calculation in their computations. As a result, this study has investigated the water wave generation and wave-structure interaction problems through numerical simulations. The numerical wave flume model constructed in this study is valid and has the potential to be extended for more complex application scenarios.

Université de Lille
Unité de Mécanique de Lille - Joseph Boussinesq
Cité Scientifique, 59650 Villeneuve-d'Ascq, France